AN INVESTIGATION OF THE FLUORESCENCE EMITTED BY ARTERIAL INTIMAS DURING IRRADIATION BY A XeCl EXCIMER LASER

by

Niresh Bhagwandin, MSc

Thesis Presented for the Degree of
DOCTOR OF PHILOSOPHY
in the Department of Biomedical Engineering
UNIVERSITY OF CAPE TOWN
February 1995

PREFACE

These studies represent original work by the author and have not been submitted in any form to another University. Where use was made of the work of others it has been duly acknowledged in the text.

ACKNOWLEDGEMENTS

I am grateful to all of the many people who helped with this thesis in one way or the other. I would like to extend a special thanks to:

Dr H Breuer, Prof. AE Bunn and Dr JE Fincham;
my supervisors, for their many inputs, guidance, advice and encouragement

Dr S Wynchank;
for showing a keen interest in this study and his constructive suggestions during the review of this thesis

Prof B Reichart and Prof JA Odell;
for suggesting and supporting this study

U Deutschlander, Prof PE Walters and T Gordon;
for their assistance with the experimental setup

P Human;
for providing aorta samples

Prof JP Nel and Lt. Bothma and his staff;
for providing iliac artery samples

The staff of the Department of Vascular Surgery, Tygerberg Hospital;
for providing femorotibial artery samples

C Woodroof;
for tissue processing and preparation of slides for histologic examination

R Edwards and my work colleagues;
for many helpful discussions and encouragement

My wife, Anusha and children, Akshar and Lipika;
for their encouragement, understanding and patience.

I would also like to thank the Medical Research Council (MRC) and Art Medical Equipment (Pty) Ltd for financial support as well as the Department of Health for time granted to me to research this project.

ABSTRACT

Laser angioplasty of occluded arteries has been limited by the unacceptably high rate of vessel wall perforation. To overcome this limitation, fluorescence spectroscopy of arterial wall tissue has been proposed as a technique to discriminate between normal and atherosclerotic arteries and thereby prevent arterial wall perforation during laser angioplasty.

In this study, a XeCl excimer laser ($\lambda = 308$ nm) was used to excite fluorescence in normal and atherosclerotic segments of human postmortem aorta and iliac arteries as well as segments of femorotibial arteries from recently amputated limbs. The laser beam was transmitted through a 600 μm quartz fibre and the fluorescence emission from the tissue samples was collected by a similar but separate fibre. The tissue samples were placed 2 mm from the ends of the fibres with air as the surrounding medium. The laser fluence at the surface of the sample was approximately 32 μJ/pulse. The fluorescence signal was transmitted to a spectrometer and from there to a gated integrator and boxcar averager system for analysis.

Fluorescence spectra from 88 arterial segments were recorded. Histological examination showed that 14 segments were normal, 37 segments were atherosclerotic and 37 segments were unclassifiable or displayed arteriosclerosis. The fluorescence spectra displayed a peak at $\lambda \cong 380$ nm and a plateau between $\lambda \cong 440$ nm and 500 nm. A pronounced dip at $\lambda \cong 420$ nm and minor dips at $\lambda \cong 540$ nm and $\lambda \cong 580$ nm were also evident. Quantitative analysis of the fluorescence spectra was performed by defining algorithms to differentiate between: (a) normal and atherosclerotic tissue, and (b) non-fibrotic and fibrotic tissue. In evaluating algorithms there was concentration on those which reflected the intrinsic properties of the tissue, whether normal or atherosclerotic. Fluorescence characteristics of extraneous properties, such as the spectral features due to oxy-haemoglobin, were avoided in the analysis. The efficacy of the algorithms was assessed by considering the sensitivity, specificity and predictive value of the algorithms. With specificity and predictive value set at 100%, the maximum sensitivities obtained are: (a) 84% for the algorithm $X1_A = I(550\ \mathrm{nm})/I(430\ \mathrm{nm}) + (I(400\ \mathrm{nm})/I(540\ \mathrm{nm}))^{0.5}$ to distinguish normal tissue from atherosclerotic tissue, and (b) 81% for the algorithm $X2'_A = (I(530\ \mathrm{nm})/I(510\ \mathrm{nm}))^{0.25} - (I(570\ \mathrm{nm})/I(550\ \mathrm{nm}))$ to distinguish non-fibrotic tissue from fibrotic tissue. However, these algorithms were not consistent in distinguishing between normal and atherosclerotic tissue nor between non-fibrotic and fibrotic tissue when the distance, *z* (between the delivery/collection fibre and tissue for values of z, $0 \text{ mm} \leq z \leq 8 \text{ mm}$) as well as when the angle, α (between the plane of the delivery/collection fibres and the plane of the sample for values of α, $90^\circ \leq \alpha \leq 160^\circ$), changes. Several algorithms with sensitivities $\geq 70\%$ that are insensitive to geometrical effects are proposed to distinguish between normal and atherosclerotic tissue and non-fibrotic and fibrotic tissue. The algorithms most suitable are insensitive to the ranges of z and α given above and hence are the most appropriate for use *in vivo* where z and α cannot be controlled as in the laboratory.

This study shows that by using fluorescence spectroscopy together with the developed algorithms it is possible to discriminate between normal/atherosclerotic tissue and non-fibrotic/fibrotic tissue, *in vitro*. This technique may be utilised to achieve safer laser angioplasty of occluded arteries, *in vivo*.

CONTENTS

Page

APPENDICES

LIST OF SYMBOLS AND ABBREVIATIONS

α:	angle between plane of sample and delivery/collection fibre
β_λ:	yield or efficiency of fluorescence production
Φ:	quantum yield of fluorescence
λ:	wavelength
μ_λ:	attenuation coefficient of tissue for radiation of wavelength λ
μ_a:	absorption coefficient
μm:	micrometre
μs:	microsecond
μ_s:	scattering coefficient
τ:	average lifetime of excited state of molecule
Ω:	geometrical collection efficiency of fibre
$\cong$:	approximately equal to
$\approx$:	approximately
a:	acceptance angle
A:	overlap area of directly irradiated area and imaged area of sample
A_e:	area of sample exposed by excitation beam
AO:	aorta
A.T.:	artery type
a.u.:	arbitrary units
cm:	centimetre
d:	distance between centres of delivery fibre and collection fibre
DT:	decision threshold
EVG:	elastic Van Gieson
F:	female
FT:	femorotibial
HE:	haematoxylin and eosin
h:	hours

Hz: Hertz

I: intensity or radiant density

$I(\lambda)$: intensity at wavelength λ

IBM: International Business Machines

IHD: ischaemic heart disease

I_{int}: integrated intensity

IL: iliac

J: Joule

KrF: krypton fluoride

LIF: laser induced fluorescence

LSI: laser spectroscopic imaging

M: male

m: metre

min.: minute

ms: millisecond

N_2: nitrogen molecule

NIM: nuclear instrumentation module

nm: nanometre

ns: nanosecond

OMA: optical multichannel analyser

OSA: optical spectral analyser

$p(\Theta)$: phase function

PMT: photomultiplier tube

PRF: pulse repetition frequency

P.M.I.: postmortem interval

r: radius of circle subtended by acceptance angle

S/N: signal-to-noise ratio

SNIR: signal-to-noise improvement ratio

S_x: electronic states of molecule, where $x = 0,1,2$

TEA: transverse excitation atmospheric

T_G: aperture duration, gatewidth or sample interval

T_p: period between successive triggers

UK: unknown

UV: ultraviolet

vs.: versus

W: Watt

XeCl: xenon chloride

XeF: xenon fluoride

yr: years

z: distance between sample and delivery/collection fibre

CHAPTER 1

INTRODUCTION

1.1 BACKGROUND OF THE STUDY

Atherosclerosis (see APPENDIX A) is a major pathological process causing death in developed countries (Ross, 1993; Prince *et al*, 1987). As atherosclerotic plaques develop within arteries, they compromise blood flow and usually cause death from complications such as distal organ ischaema, embolisation or infarction. Gangrene and loss of function in the extremities is also a result of atherosclerosis.

Although atherosclerosis may affect any artery, myocardial infarcts (heart attacks) and cerebral infarcts (strokes) are acute end points which may be lethal or permanently debilitating.

Walker *et al* (1993) report that the mortality rate from ischaemic heart disease (IHD) in South Africa has decreased over the past two decades. However, the IHD rates are very high. Their studies among the interethnic South African populations during 1978 to 1989 indicate that IHD mortality rates are relatively high among whites and Asians, lower in coloureds and very low among blacks (see Figure 1.1). However there is increasing evidence that as blacks become urbanised and/or adopt Western diets their incidence of IHD increases. Such findings have been reported in New Orleans, USA (Strong *et al*, 1984), Nigeria (Ogunnowo *et al*, 1986), the Seychelles (Bovet *et al*, 1991), Charleston, USA (Keil *et al*, 1993) and Orange Free State, South Africa (Mollentze *et al*, 1995).

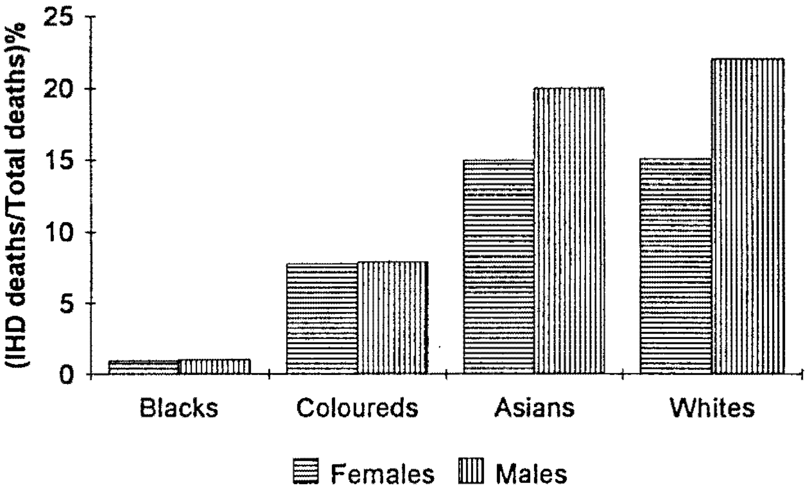

Figure 1.1 Deaths as a result of ischaemic heart disease (IHD) in relation to total deaths per population sector in South African peoples in 1989 (from Walker *et al*, 1993).

The well established methods for restoring blood flow are recanalising the obstacle or replacing the blocked section of the vessel. This often necessitates major surgery, especially for the coronary by-pass. Since this procedure imposes a heavy strain on an already weakened patient, percutaneous methods of restoring blood flow are highly desirable. A considerable effort is presently being made to find a less invasive procedure of restoring blood flow that would also reduce the recovery time as well as the costs.

1.2 PERCUTANEOUS ANGIOPLASTY TECHNIQUES

In order to re-establish blood flow through fully or partially blocked arteries, the obstacle to free flow inside the vessel has to be reduced either by pressing it into the vessel wall or by removing it altogether. A combination of both methods can also be considered, i.e., creating a channel by removing tissue with subsequent compression of the remaining constriction into the interior vessel wall.

Of the percutaneous techniques that have been performed, balloon dilatation and laser angioplasty have enjoyed some degree of success (Breuer, 1990a). These techniques as well as the problems associated with them are discussed below.

1.2.1 Balloon Dilatation

In balloon dilatation, a balloon catheter is positioned in the affected area. As the balloon is inflated it crushes the atheromas (degenerated thickened arterial intima occurring during atherosclerosis) against the artery wall and so clears the vessel's interior. However, a complete obstruction cannot be treated in this way. The average success rate for balloon dilatation alone is greater than 85% in lesions less than 20 mm in length. However the rate drops to less than 60% in lesions longer than 20 mm (Moretti, 1991). Furthermore, with this method failure frequently occurs and the artery fills up, thereby requiring a repeat attempt.

1.2.2 Laser Angioplasty

The problems experienced in balloon dilatation led researchers to consider other methods such as laser angioplasty. Here, laser radiation is transported via optical fibres to the site of obstruction. Once sufficient radiant energy reaches the site and is absorbed, an open lumen distal to the end of the optical fibre is created either by thermoablation or photoablation of the stenosing material. The interaction that dominates depends on the wavelength and power density of the incident radiation.

(a) Thermoablation

In thermoablation, radiation energy emitted by the laser and transferred to the stenosing tissue is absorbed by the tissue and converted into heat which in turn raises the tissue's temperature. If the intensity of the radiation, I, is sufficient, i.e., a few W/cm^2, the tissue may undergo the following phases: thermal expansion, denaturation, melting, and evaporation via exploding bubbles leaving a molten surface and charred edges.

The temperature rise in the tissue is not restricted to the forward direction with respect to the laser beam but spreads laterally as well, a serious complication if recanalisation of small diameter vessels is attempted. Thermoablation can be achieved by using a bare fibre, a capped or 'hot tip' or by using fibres that are only partially transparent to radiation (see Figure 1.2).

Employing the bare distal tip of the optical fibre has the disadvantage that the radiation is often emitted non-axially. Furthermore, the sharp edges of the fibre may cause mechanical injury. But the major drawback of this method is the penetration depth of the received radiation. Infrared radiation may penetrate up to a centimetre distal to the fibre tip. In the case of tortuous coronaries, this may damage the vessel walls.

Tiny metal caps enclosing the distal fibre tip overcome those disadvantages. When the laser radiation is absorbed in the metal, the cap will become hot and consequently act as a uniform source of thermal energy. Thermal energy will penetrate via thermal conduction in all directions and tissue in contact with the metal will vaporise. By gently pushing forward the capped fibre, a channel develops. Although the temperature decreases exponentially with distance from the cap, it may still cause tissue damage a few millimetres laterally from the channel, again rendering the method dangerous for small vessels.

Partly transparent caps, e.g., caps with a small opening in the forward direction or made of temperature resistant translucent crystals avoid a problem encountered by heated metal which tends to stick to the channel walls as soon as the source of thermal energy is

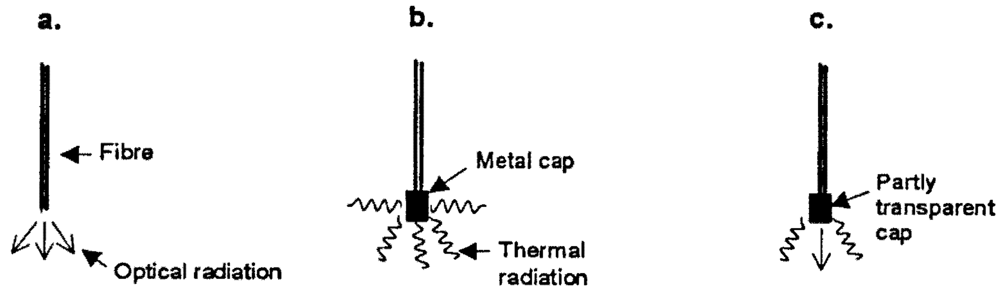

Figure 1.2 Illustration of fibre tips. **a.** bare fibre **b.** capped tip **c.** partially transmitting cap

removed.

Another serious disadvantage of recanalisation by thermal ablation is that it cannot remove partially calcified tissue.

(b) Photoablation

It has been demonstrated that very short (submicrosecond) ultraviolet (UV) laser radiation pulses can ablate tissue of any composition, including calcified tissue and even bone, with negligible local heat production. This process has been termed photoablation.

The following description gives a brief outline of the photoablation process (Dardenne and Hohla, 1989): tissue is composed mainly of long-chain organic molecules and interstitial water molecules. The UV radiation is absorbed only by the organic molecules which are broken up into small volatile fragments provided the photon energy exceeds a threshold value. If the laser beam transfers sufficient energy, the volatile fragments cause microexplosions due to the larger volume they occupy and the interstitial water is ejected. High-speed photography has shown that the process resembles the familiar form of an explosion.

The photoablation effect has a power density threshold of approximately 10^9-10^{10} W/cm^2 (Dardenne and Hohla, 1989) for the beam wavelength used and for human tissue (see Figure 1.3).

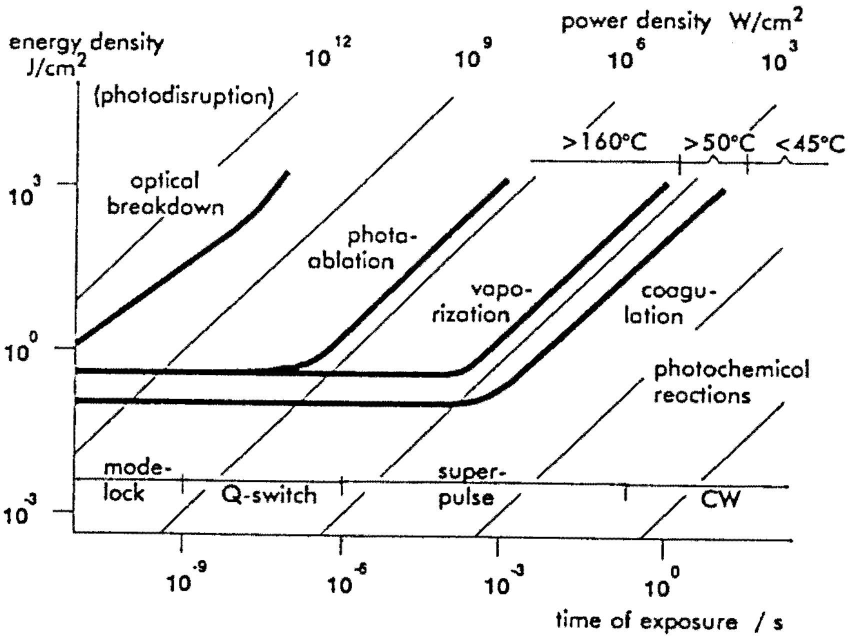

Figure 1.3 "Threshold and energy density in different laser tissue reactions to describe the difference in tissue removal" (from Schaldach, 1990)

Below this threshold, the laser radiation is converted into heat and deeper zones of necrosis can be observed. Above the threshold, the thickness of the ablated layer increases in proportion to the laser energy density. No further increase of ablated layer thickness is observed beyond an additional threshold energy density, as the entire material will then be removed within the depth of penetration. The necrotic zone will decrease with increasing laser energy density. The smaller the penetration of the laser beam into the tissue, the smaller will be the threshold energy density and the thickness of layer ablated less for each laser pulse. For the XeCl laser, the ablative threshold is 2 J/cm^2 (Schaldach, 1990).

Excimer lasers (see APPENDIX B) are well suited for photoablation since they produce high-energy (>10^{-1} J), short-pulse (10 to 16 ns) radiation in the UV region (193 to 351 nm) (Parrish, 1985).

1.3 PROPOSED SOLUTION TO PROBLEM OF ARTERIAL PERFORATION

An integrated laser catheter delivery system that is capable of reliable *in vivo* atheroma recognition is desirable for safe and effective laser angioplasty, especially in small, tortuous conduits of the coronaries, (e.g., left coronary, left circumflex, left anterior descending, right, etc.) and long blockages of peripheral vessels. Whilst photoablation has been demonstrated to ablate variable composition atheroma (including calcified material) without eliciting thermal damage to surrounding normal tissue, precise tissue ablation with pulsed lasers still does not prevent transmural perforation at vessel bends and cannot accurately direct the course of plaque recanalisation within an eccentric stenosis or a total occlusion.

The fluorescence (see APPENDIX C) that occurs when visible and UV laser radiation interacts with tissue opens up an interesting possibility. Investigations have shown the spectral composition of this fluorescence to be the equivalent of a "optical fingerprint" of the irradiated tissue (Laufer *et al*, 1988). For example, calcium-containing tissue fluoresces significantly differently from cartilage.

In a “smart” laser angioplasty system, the fluorescence occurring in response to laser irradiation of the arterial wall can be evaluated in real time for each individual laser pulse. The results can then be utilised to control the next laser pulse delivered to the arterial tissue. For instance, the laser angioplasty system can be made to stop automatically if the laser beam strikes healthy tissue.

1.4 AIMS OF STUDY

The aims of this study were threefold, viz.,

a. develop and evaluate spectral classification algorithms for discriminating normal and atherosclerotic arteries by their respective fluorescence spectra. In order to realise a "smart" laser angioplasty system to overcome the problem of arterial perforation, an on-line spectral analysis algorithm or algorithms will be required to discriminate between the fluorescence spectra from normal and atherosclerotic tissue;

b. determine whether the fluorescence signals could be utilised to diagnose the state of the tissue. It is desirable to track the development of atherosclerosis *in vivo* as it will provide important information about both the need to treat and the most effective treatment for a given stage of atherosclerosis. In the past few years, intravascular ultrasound (IVUS) has been used as a technique for detection and quantification of atherosclerosis (Dake, 1991; St. Goar *et al*, 1992; Sechtem *et al*, 1993); and

c. determine the influence of the geometry of the laser delivery and fluorescence collection system on the fluorescence signal. In the final analysis, the choice of a spectral classification algorithm or algorithms will depend on how it behaves during *in vivo* investigation of arterial tissue. Hence geometries that are likely to occur during *in vivo* investigation of arterial tissue must be simulated.

No studies, in the opinion of the author, utilising the materials and method described in this thesis and with the above-mentioned goals, were previously attempted.

1.5 OUTLINE AND SUMMARY OF THESIS

The starting point of the work presented in this thesis is an introduction to percutaneous angioplasty techniques that are presently being utilised to re-canalise blocked arteries, viz., balloon angioplasty and laser angioplasty. Balloon angioplasty is successful in treating partial blockages, however, the restenosis rate is high, viz., 30% at 6 months (Breuer, 1990b). Laser angioplasty is preferable because of its ability to ablate plaque and thereby reduce the restenosis rate. Nevertheless, laser angioplasty is limited by the high rate of arterial wall perforation. The overall aim of this study was to measure the fluorescence emitted from arterial tissue during irradiation by a XeCl laser and assess whether this fluorescence may be utilised to discriminate between normal and atherosclerotic artery wall and thereby prevent arterial wall perforation.

In chapter 2, the interaction of laser radiation with biological tissue and a model of the fluorescence emitted by the tissue are discussed. The XeCl laser (λ = 308 nm) radiation has a penetration depth of ≈ 50 μm in arterial tissue which implies that the fluorescence originates primarily from the intima of the arterial wall. Wide ranges of laser frequencies (from ultraviolet to visible), fluorescence collection geometries and tissue samples have been used in the fluorescence studies. Several fluorescence detection schemes such as surface fluorescence, time-resolved fluorescence and medical imaging have been proposed to discriminate between normal and atherosclerotic arteries and are discussed. The limitations of other's research were assessed to determine what investigations were necessary to fill the gaps.

In chapter 3 the experimental apparatus and methodology used in this investigation are discussed. A dual fibre system was used to deliver the laser radiation and to collect the fluorescence. The collected fluorescence signal is transmitted to a spectrometer which consists of a scanning monochromator (scan rate: 100 nm/min) and a fast rise-time photomultiplier tube which detects the dispersed light intensity. The signal is then sent to a gated integrator and boxcar averager. A fluorescence intensity that is proportional to the amplitude of the signal is output at each wavelength.

In this study, human aorta, iliac and femorotibial arteries (all in an unfixed state, stored in air and kept at ambient temperature) were investigated. In total, 88 arterial segments were analysed. After study, the exact location from which the fluorescence was collected was marked with India ink and the sample stored in formalin for preservation and histolgic processing. An analysis of the fibre geometry and a description of the tissue classification scheme used in this study are also given in chapter 3.

In chapter 4, the patient details and histology of the samples that were investigated are presented. Photomicrographs representing some of the different stages of atherosclerosis and denoted in the text as Stary types I, I-II, II, IV, V, VIa, VIc, VII , VIII (Stary, 1992b) were made. Of the 88 samples that were investigated, 51 could be classified as normal or atherosclerotic. Thirty-five percent of the samples displayed arteriosclerosis and were not considered in this investigation.

The performance characteristics of the measurement set-up was thoroughly investigated to determine the optimal settings of the measuring system. Settings of the photomultiplier voltage, gate delay, gate width, monochromator exit slit width and cut-off filter were determined after systematic investigation.

Baseline measurements were also performed. The background radiation is negligible compared to the fluorescence emitted from arterial tissue. Experiments show that the fluorescence intensity from arterial tissue decreases exponentially with exposure to the laser radiation. The rates of decay of the fluorescence intensity (4800 laser pulses) are consistent to within ± 5% for measurements performed at wavelengths $\lambda = 380$ nm and $\lambda = 460$ nm. Further measurements indicate that photobleaching of the samples occur during exposure to XeCl laser radiation.

Representative spectra of 8 Stary types of atherosclerotic lesions (Stary, 1992b) as well as normal and arteriosclerosis tissue are presented. The spectra are uniform in the wavelength range $\lambda = 300$ nm to $\lambda \cong 335$ nm and this is a result of the selective absorption of radiation by the filter placed in front of the monochromator. The spectra are characterised by a broadband fluorescence emission with a prominent dip at $\lambda \cong 420$ nm and less pronounced dips at $\lambda \cong 540$ nm and $\lambda \cong 580$ nm. These dips are due to the reabsorption of fluorescence by oxy-haemoglobin. Several fluorophores have been identified as the source of the fluorescence maxima.

Quantitative analysis of the fluorescence spectra was performed by defining algorithms to differentiate between normal and atherosclerotic tissue as well as between non-fibrotic and fibrotic tissue. The efficacy of the algorithms was assessed by determining their sensitivity, specificity and predictive value.

Fourteen general algorithms were defined and applied to the fluorescence spectra to determine which algorithm(s) would provide the highest sensitivity. With specificity and predictive value set at 100%, the maximum sensitivities obtained are: a. 84% for the algorithm $X1_A = I(550\text{ nm})/I(430\text{ nm}) + (I(400\text{ nm})/I(540\text{ nm}))^{0.5}$ to distinguish normal tissue from atherosclerotic tissue, and b. 81% for the algorithm $X2'_A = (I(530\text{ nm})/I(510\text{ nm}))^{0.25} - (I(570\text{ nm})/I(550\text{ nm}))$ to distinguish between non-fibrotic and fibrotic tissue. Nevertheless, these algorithms were not consistent in distinguishing between normal and atherosclerotic tissue nor between non-fibrotic and fibrotic tissue when the distance, z, between the delivery/collection fibre and tissue for $0\text{ mm} \leq z \leq 8\text{ mm}$ as well as when the angle, α, between the plane of the delivery/collection fibres and the plane of the sample for $90° \leq \alpha \leq 160°$, changes. The algorithms with sensitivities $\geq 70\%$ that not affected by changes in z and α are proposed.

In chapter 5, the results of this study are compared with those of other studies and a critical assessment is made of the similarities and differences in the results. The limitations of this study are also discussed.

CHAPTER 2

LITERATURE REVIEW

2.1 INTERACTION OF LASER RADIATION WITH BIOLOGICAL TISSUE

The two main processes that occur when laser radiation impinges on human tissue are scattering and absorption of the radiation by constituents of the tissue. In general, scattered photons are forward directed in human tissue (Wu, 1993a, b). The scattered photons continue to experience additional scattering events until they are absorbed. Absorption usually results in the excitation of the molecule, which can either dissipate its energy as heat or by re-radiating a fluorescent photon. Molecules that fluoresce act as isotropic point sources of radiation within the tissue.

An artery wall consists of three composite layers (see Figure 2.1): a thin intima (see APPENDIX D) extending from the endothelium to the internal elastic lamina, then thick dense layers of collagen, elastin and smooth muscle cells (the media), and on the outside a thin coating of loosely arranged collagen fibres, small blood vessels (vasa vasora) and adipose tissue (the adventitia).

Optical properties of tissues are generally specified by three quantities: (a) the absorption coefficient, μ_a, which is the measure of the probability of a photon being absorbed per unit length; (b) the scattering coefficient, μ_s, which is the measure of the probability of a photon being scattered per unit length; and (c) the phase function, p(Θ) which describes the scattering angular distribution where Θ is the angle of photon deflection after a single scattering event.

μ_a for the XeCl laser (λ = 308 nm) is 200 cm^{-1} (Dörschel and Müller, 1992) and the penetration depth ($1/\mu_a$) is therefore 50 µm. The effective absorption coefficient and penetration depth (i.e., when corrected for scattering in normal soft tissue as a function of λ) are 1670 cm^{-1} and 6 µm, respectively (Dörschel and Müller, 1992). Measurements performed by Baraga *et al* (1990) with an absorption spectrophotometer indicate that the

Figure 2.1 Structure of artery wall

1/e penetration depth of 306-310 nm light in the intima of normal aorta is between 80 and 100 μm. These measurements agree with photoacoustic measurements of attenuation in normal intima performed by Oraevsky *et al* (1992). Gmitro *et al* (1988) showed that the fluorescence arises from a tissue zone 150 μm beneath the transmitting fibre. The wavelength of the excitation radiation was 325 nm.

2.2 FLUORESCENCE MODEL

An understanding of the fluorescence spectra is achieved by examining the theoretical fluorescence model developed by Gmitro *et al* (1988). This model is described below (see Figure 2.2). Assume that an optical fibre is placed in contact with a section of tissue of thickness x, and that the fibre emits an optical signal of wavelength λ_0 and radiant flux I_0 into the tissue. If a fibre with a small numerical aperture is used, so that the light propagates in first approximation as a parallel beam, and the tissue is homogeneous with an attenuation coefficient at the wavelength λ_0 of μ_0, the total intensity I at any plane at depth x' is (Beer's Law):

$$I(x') = I_0 e^{-\mu_0 x'} \qquad (1)$$

If the yield, or efficiency of fluorescence production, is independent of the intensity level and is given by a factor β_λ of the intensity I' emitted by the tissue at wavelength λ and at the plane at depth x', then this yield is

$$I'(x',\lambda) = \beta_\lambda I_0 e^{-\mu_0 x'} \qquad (2)$$

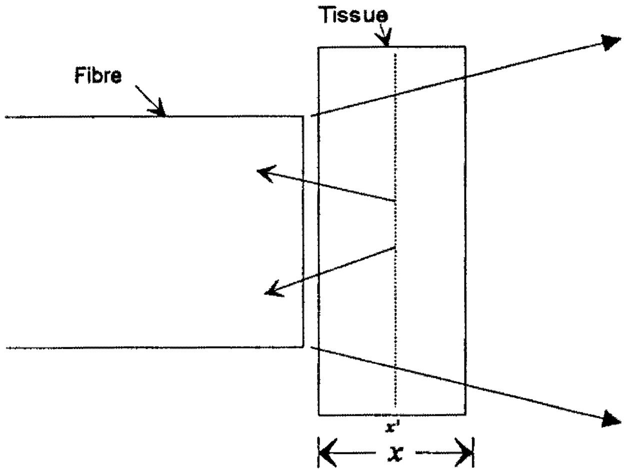

Figure 2.2 Geometry of fluorescence model

The fibre collects a portion of the radiation from each plane at depth x' to produce the optical signal transmitted back to the outside world. It is reasonable to make the simplifying assumption that, because of the small numerical aperture, the geometrical collection efficiency Ω of the fibre is the same for all points in the tissue. The fluorescent radiation at wavelength λ is attenuated as it propagates back a distance x' through the tissue, consequently the fluorescent intensity is given by

$$I''(x',\lambda) = \Omega\beta_\lambda I_0 e^{-\mu_0 x'} e^{-\mu_\lambda x'} \qquad (3)$$

where μ_λ represents the attenuation coefficient of the tissue for radiation of wavelength λ. The prime notation on I has been dropped to indicate that I now represents the signal returned from a thickness of tissue x and is obtained by integrating Equation (3) from 0 to x, in which case

$$I(x,\lambda) = \int_0^x \Omega\beta_\lambda I_0 e^{-\mu_0 x'} e^{-\mu_\lambda x'} dx'$$

$$= \frac{\Omega\beta_\lambda I_0}{\mu_0 + \mu_\lambda}(1 - e^{-(\mu_0+\mu_\lambda)x}) \qquad (4)$$

2.3 FLUORESCENCE STUDIES

The use of tissue fluorescence as a diagnostic aid in laser angioplasty was proposed by Kittrell *et al* (1985). Since then, several studies to improve tissue discrimination have been reported. These include the use of different types of lasers, fluorescence collection geometries and tissue samples.

The fluorescence detection schemes to discriminate between normal and diseased tissue may be divided into the following methods, viz., surface fluorescence, time-resolved fluorescence and medical imaging.

2.3.1 Surface fluorescence

In this technique, the data analysis is based on the recording of the relative intensity of two or more regions of the fluorescence spectrum and the comparison of their absolute values or their ratios for normal or atherosclerotic samples.

Kittrell *et al* (1985) used laser radiation of wavelength, λ = 480 nm, as the source of excitation on human cadaver carotid artery samples. Normal samples displayed distinct spectral peaks of approximately equal intensity at λ = 550 nm and λ = 600 nm.

Atherosclerotic samples exhibited the same two peaks but with the λ = 600 nm peak always "smaller" than the one at λ = 550 nm. Their results suggested that the presence of atherosclerotic plaque can be determined by comparing the relative intensities of fluorescence at λ = 550 nm and λ = 600 nm due to excitation at λ = 480 nm. They used the intensity ratio of the peaks at λ = 550 nm and λ = 600 nm to show a strong correlation between spectroscopic and histologic results.

Richards-Kortum *et al* (1987) obtained laser-induced fluorescence from freshly excised cadaver aorta using an argon-ion laser (λ = 476 nm). They found that normal artery fluorescence has more structure and is three times as intense as the atherosclerotic artery fluorescence. With normal artery the intimal fluorescence is slightly different to the composite fluorescence of the entire wall because of the contribution of the underlying media. With fibrous plaque, the composite and intimal spectra are equivalent, indicating that the atherosclerotic intima has been infiltrated by elements of the underlying layers.

Laufer *et al* (1988) used a KrF excimer laser (λ = 248 nm) to irradiate normal and severely atherosclerotic segments of human post-mortem femoral arteries. The total fluorescence of irradiated and ablated tissue was analysed in real-time mode by means of spectroscopy. Each laser pulse produced one spectrum that was characteristic of the composition of the tissue layer, which was then ablated. Fluorescence indicated a broad-continuum emission between λ = 300 nm and λ = 700 nm with a double peak fluorescence at wavelengths of 370 nm and 460 nm of equal intensity (ratio, 1.004 ± 0.087) for normal media layers. Atheroma without calcification (lipid, fibrous, and mixed tissues) was found to have spectral maxima at the same wavelengths but with significantly reduced intensity at λ = 460 nm (ratio, 1.765 ± 0.263; $p<0.001$). In contrast to this broad-continuum fluorescence, calcified plaques displayed multiple-line emission with the most prominent peaks at wavelengths 397 nm, 442 nm, 450 nm, 461 nm, 528 nm and 558 nm.

Bergeron *et al* (1988) obtained an entire fluorescence spectrum (excitation-emission) from λ = 200 nm to λ = 1000 nm on normal and atherosclerotic arteries. Previous studies on the fluorescence spectroscopy of arterial walls had generally been made at discrete excitation wavelengths. Their study shows that the entire fluorescence spectrum gives a more accurate analysis. They attribute the differences (between their results and those previously published) that exist in the exact localisation of the maximum fluorescence peaks to the difficulties in establishing the maximum fluorescent determination and to the variation between samples. They argue that using the entire excitation spectrum ensures that the maximum fluorescence is detected even if the sample characteristics are slightly different.

Svanberg (1989) used nitrogen laser excitation (λ = 337 nm) and found very prominent differences in the fluorescence spectra between atherosclerotic plaque and normal artery wall, both for the aortic arch and coronary vessels. The intensities of the two peaks at λ = 400 nm and λ = 450 nm and at the minimum at λ = 420 nm were evaluated. In addition, the intensity at λ = 480 nm was utilised since the spectra of atherosclerotic plaque and normal artery also differed in this region.

Baraga *et al* (1990) studied ultraviolet excited laser induced fluorescence (LIF) in normal and atherosclerotic human arterial wall *in vitro*. Using excitation wavelengths from 306 nm to 310 nm, two distinct emission bands were observed in the LIF of both normal and pathologic aorta: a "short" wavelength band peaking at λ = 340 nm which was attributed to tryptophan; and "long" wavelength band, peaking at λ = 380 nm, which was assigned to a combination of collagen and elastin. The intensity of the short wavelength band was sensitive to the choice of excitation wavelength, while the long wavelength was not, so that the relative contribution of the bands could be controlled by the precise choice of excitation wavelength. A dip in the spectra at λ = 418 nm was attributed to fluorescence reabsorption by oxy-haemoglobin.

By using λ = 308 nm excitation to observe fluorescence emission simultaneously from both the short and long wavelength bands, normal and atherosclerotic aorta were spectrally distinct (Baraga *et al*, 1990). Two LIF emission intensity ratios were defined to characterise both the relative tryptophan fluorescence content as well as the ratio of elastin to collagen fluorescence in each spectrum, i.e., I(335 nm)/I(380 nm) and I(480 nm)/I(380 nm) respectively. The differences in these two emission ratios among the various histologic tissue types correlated qualitatively with the histologic and biochemical compositions of these tissues. By combining these parameters in a binary classification scheme, normal and atherosclerotic aorta were correctly distinguished in 56 of 60 cases, *in vitro*. Furthermore, "atherosclerotic plaques", "atheromatous plaques", and "exposed calcifications" could be classified individually with sensitivities/predictive values of 90%/90%, 100%/75%, and 82%/82%, respectively.

Morguet *et al* (1994) evaluated arterial autofluorescence spectroscopy *in vitro* using a single XeCl laser (λ = 308 nm) for simultaneous tissue ablation and fluorescence excitation. In this study arterial media, lipid plaques and calcified plaques of aortic specimens were investigated in air, saline and blood. The spectrum of calcified lesions was sensitive to the surrounding optical medium whereas the spectra of arterial media and lipid plaques remained constant. In saline, there was no clear-cut spectroscopic difference between lipid plaques and calcified lesions. Normal arterial media could still be discriminated from atherosclerotic lesions (lipid plaques plus calcified lesions).

Pettit *et al* (1990) used a XeF laser (λ = 351 nm) to evaluate the endothelial surface and subsurface fluorescence during ablation. They found that calcified tissue consistently displays a broader fluorescence profile than healthy arterial wall. Fluorescence spectra from lipid-rich plaque precursor regions also display variations relative to those of normal tissue. These spectral differences were observed with both dual and single optical fibre fluorescence collection systems. Spectra taken from atherosclerotic sites after ablative penetration of the calcified plaque are similar to spectra obtained at healthy sites after ablation of part of the wall tissue. Fluorescence spectra obtained during ablation in calcified sites reveal distinct sharp lines not seen upon ablation of healthy vessel wall.

Ye and Abela (1992) report that the total fluorescence intensity of normal arterial samples is twice as great as that of fibrous atheroma. Their experiments show that both laser excitation power and tissue characteristics are responsible for the changes in the total intensity of fluorescence from arterial tissue. They used two laser wavelengths, viz., 488 nm and 514 nm of equal power and noted that the absorption coefficients of normal artery and atherosclerotic plaque are different in the wavelength range 420 nm to 530 nm. They speculate that the absorption differences which cause the change in penetration depth can lead to modification of the total intensity of fluorescence emission.

2.3.2 Time-resolved fluorescence

This technique is based on the measurement of the fluorescence decay times of the basic tissue components. The characteristic decay times serve as identifiers of the various tissue components.

Andersson-Engels *et al* (1990a, b) used time-resolved fluorescence for enhanced demarcation of human atherosclerotic plaques *in vitro* rather than the customary time-integrated monitoring technique. They demonstrated that a considerable improvement in plaque demarcation can be obtained using the temporal behaviour of the tissue fluorescence. It was also demonstrated that the interference from blood can be excluded by using such techniques. Since fluorescence spectra from tissue exhibit little structure, they claim that the additional information obtained from the time domain is of great value.

2.3.3 Medical imaging

Sartori *et al* (1987) irradiated the internal surface of isolated arteries with or without atherosclerosis with an argon ion laser and the peak intensity of the excited autofluorescence spectrum was related to the composition of the arterial wall. The higher autofluorescence intensity in the wavelength range between approximately 480 nm and 630 nm for grossly calcified tissue compared to normal or noncalcified atherosclerotic tissue is used to produce maps of the arterial wall. These images delineate the calcified areas of the sample with good spatial resolution, viz., 2.5 mm x 2.5 mm.

Andersson *et al* (1987) discuss the principles of a powerful multicolour imaging system for tissue fluorescence diagnostics. Four individual spectrally filtered images are formed on a matrix detector by means of a split-mirror arrangement. The four images are processed in a computer, pixel by pixel, by means of mathematical operations, leading to an optimised contrast image, which enhances a selected feature.

Hoyt *et al* (1988) used a laser spectroscopic imaging (LSI) technique for remote acquisition of spectroscopic images of biological tissues and tissue conditions. The technique employs laser-induced spectroscopic signals, collected and transmitted via an array of optical fibres, to produce discrete pixels of information from which a map or image of a desired tissue characteristic is constructed. They describe a prototype LSI catheter that produces spectral images of the interior of human arteries for diagnosis of atherosclerosis. The diagnostic ability is based on the fact that normal artery wall and atherosclerotic plaque exhibit distinct fluorescence spectra in the wavelength range 500 nm to 650 nm when excited by λ = 476 nm laser light. The fluorescence from blood is minimal. The catheter is composed of 19 optical fibres enclosed in a transparent, protective shield. In these studies, an optical multichannel spectral analyser was used for detection of the signal and computer-processed 19-pixel spectroscopic images were produced of vessels from a fresh cadaver. The images describe the spatial distribution of tissue type, disease or condition of the tissue at the distal end of the device.

2.4 CRITICAL ANALYSIS OF LITERATURE

Analysis of the literature shows that the fluorescence spectra of arterial tissue varies with the wavelength of the excitation radiation. When a XeF laser (λ = 351 nm) is used to excite fluorescence in arterial tissue, the fluorescence spectra displayed a peak at $\lambda \cong 450$ nm (Pettit *et al*, 1990). Excitation by a laser of wavelength (λ = 480 nm) produces peaks at λ = 550 nm and λ = 600 nm (Kittrel *et al*, 1985). N_2 laser excitation (λ = 337 nm) produced peaks at λ = 400 nm and λ = 450 nm (Svanberg, 1989).

The XeCl excimer laser can be used as a source of radiation for exciting fluorescence in arterial tissue as well as photoablating arterial tissue (Singleton *et al*, 1987). The XeCl laser can also make well defined cuts in biological material with very little injury to the adjacent remaining tissue (Singleton *et al*, 1987). Furthermore, since the penetration depth (≈ 50 μm) of the XeCl laser in arterial tissue is very shallow, it provides for greater control of the ablation process and a narrower region of subjacent tissue will have been exposed to potentially damaging intensities of radiation.

Geometrical effects such as the distance between the delivery and/or collection fibre and the sample, the angle of the sample surface relative to the excitation beam and single fibre vs dual/multiple fibre configurations have not been thoroughly investigated for the XeCl laser. Previous investigations (Schomaker *et al,* 1992; Keijzer *et al* 1989; Pettit *et al,* 1990, Sartori *et al,* 1987 and Richards-Kortum *et al,* 1988) have produced conflicting results.

Schomaker *et al* 1992 report that different fibreoptic probe geometries may vary in their sensitivity to morphology-induced changes in fluorescence signals because of differences in the spatial region sampled. Multiple collection fibres arranged concentrically about the excitation fibre and placed in direct contact with the tissue would effectively probe fluorescence which originated deeper within the tissue and hence be more sensitive to absorption effects. They contend that such differences may be significant in comparing results using single fibre probes with probes using separate fibres for excitation and fluorescence collection.

Keijzer *et al* (1989) have demonstrated that excitation and collection through the same optical fibre in contact with the tissue produce fluorescence spectra different from those excited via one fibre and collected through an adjacent fibre. They contend that on the tissue surface area directly illuminated by the excitation light the fluorescence spectra are less distorted by reabsorption of the fluorescence. They conclude that to differentiate tissues based on variation in intrinsic fluorescence, a single fibre system is most appropriate. Tissue differentiation based on fluorescence reabsorption, however, is enhanced by measuring far from the excitation beam, where the average path length of the light has been longer and where the spectral signature of the tissue absorption is more prominent. The findings of Keijzer *et al* (1989) are in conflict with the findings of Pettit *et al* (1990) where it was reported that the fluorescence spectra obtained with a dual fibre system is similar to that obtained by a single fibre system.

Sartori *et al* (1987) used an argon ion laser (λ = 457.9 nm) to excite fluorescence in tissue and report that investigations show that the fluorescence spectra remain unchanged when both the delivery fibre and collection fibre are brought into immediate contact with the tissue surface. It is claimed that this insensitivity of the fluorescence to fibre positioning should facilitate the adaptation of the method to *in vivo* use.

It has been reported by Richards-Kortum *et al* (1988) that the fluorescence lineshapes obtained depend significantly on the geometry of the collection system used, due to tissue filtering. They used visible radiation (λ = 476 nm) as the source of excitation and conclude that geometrical effects may be less relevant for an ultraviolet excitation source due to the shallow penetration depth of the ultraviolet radiation.

Most recent studies (Pettit *et al*, 1990; Morguet *et al*, 1994) utilise optical multichannel analysers (OMAs) or optical spectral analysers (OSAs) for fluorescence measurements. The OMA or OSA systems combine the advantages of high sensitivity, simultaneous detection of extended spectral ranges, and the capability of time resolution. OMA/OSA systems also have the advantage of producing a complete spectrum with a single laser pulse.

The fluorescence lineshape depends largely on the spectral response of the fluorescence detection system. However, differences between spectra are more important than the spectral fluorescence lineshapes themselves (Morguet *et al*, 1994).

Different authors have used different schemes for classifying atherosclerotic tissue because of local tradition or habit. Different terms are often used for lesions with identical morphologies (Stary, 1992b). The lack of a uniform and biologically valid terminology and classification can lead to serious misunderstandings when the data of different studies are compared. For example, Laufer *et al* (1988) considered the following pathological tissue lesions to represent the variety of chemical and physical structures in human atherosclerosis: lipid plaque, fibrous plaque, mixed plaque and calcified plaque. Baraga *et al* (1990), histologically classified atherosclerotic tissue according to the categories defined as follows: intimal fibroplasia, atherosclerotic plaque, atheromatous plaque, nonulcerated calcified plaque and exposed calcification.

It is clear that much work has been done in this field in the last decade due both to the availability of suitable lasers and detectors and also to the intrinsic importance of the principal problem of distinguishing between normal and atherosclerotic arterial tissue *in vivo* with a percutaneous method. However, there are discrepancies and limitations of others' work, described above, which have led to the study comprising this thesis.

CHAPTER 3

MATERIALS AND METHOD

3.1 EXPERIMENTAL SET-UP

The experimental apparatus used in this investigation is shown in Figure 3.1.

3.2 LASER SYSTEM

Laser radiation is supplied by a XeCl excimer laser (LAMBDA-PHYSIK EMG 101 MSC). The laser provides pulses of radiation (λ = 308 nm) at a variable pulse repetition rate of 1 to 50 Hz. A pulse counter (MONSANTO Model 101A) is used for accurate setting of the pulse repetition frequency of the laser.

The risetime of the laser radiation was measured with a fast photodiode (MOTOROLA MRD-510) and a high speed sampling storage oscilloscope (HEWLETT PACKARD HP54502A). The risetime of a typical pulse was measured as 17 ns.

The pulse energy of the principal beam (cross-section: 25 mm x 10 mm) was measured with a laser probe (JOULEMETER) and found to be 170 mJ per pulse (maximum).

The principal beam was focused by an optical lens (f = 200 mm). The beam is then emitted into the proximal end of a quartz optical fibre of core diameter 600 μm and numerical aperture (n.a.) = 0.22 (SCHOTT HQSW1.2) which is placed approximately 30 mm away from the focal point of the lens. The distal end of the fibre was polished and positioned above the sample in air.

In our experiments we found that considerable damage to the proximal surface of the fibre resulted if the fibre was placed directly at the focal point of the lens. Approximately 50 μm per pulse was ablated from the surface of the fibre. The energy density at the focal point of the lens is approximately 170 J/cm^2 (area of beam spot 0.5 mm x 0.2 mm). The catastrophic damage threshold of a quartz fibre to XeCl laser radiation was determined as 42 J/cm^2 by Taylor *et al* (1988).

With this arrangement, the laser energy at the distal end of the fibre was measured with a LASER PRECISION RjP-735 PYROELECTRIC ENERGY PROBE and a LASER PRECISION Rj 7620 meter. The average energy at the distal end of the fibre is 31.7 μJ.

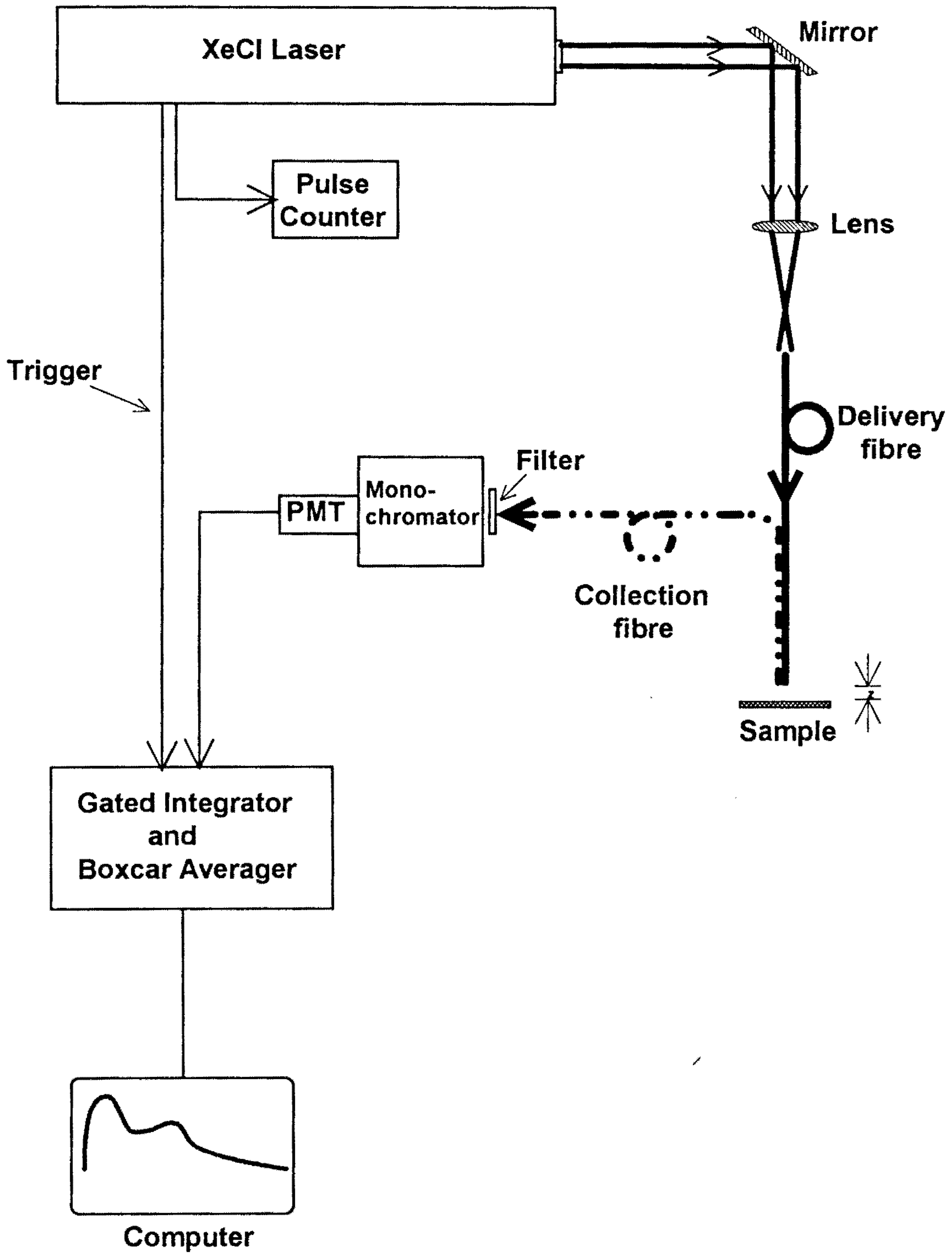

Figure 3.1 Experimental set-up

This pulse energy was used in the experiments as it was the maximum energy that was possible with the experimental set-up. The measurements show that there is a 0.02% overall efficiency, measured from the exit of the laser source. The fluctuation of the XeCl laser output was ±5%. The laser energy at the distal end of the fibre vs. the number of readings is shown in Figure 3.2.

3.3 FLUORESCENCE SPECTROSCOPY

The tissue samples were pinned to a flat pierce of cork board and mounted on a translational stage that could be moved in the x, y and z directions.

The fluorescence emission from the tissue is collected by the same type of fibre used to deliver the laser radiation, i.e., SCHOTT HQSW1.2. For the detection of the fluorescence spectra, the fibre for delivery of the laser radiation and the fibre for the fluorescence collection leading to the monochromator were mounted in parallel and as close to each other as possible. The distance between the end of the fibres and the sample, z, was kept fixed at approximately 2 mm unless otherwise stated. In our experiments it was found that there were changes in the fluorescence in fluorescence spectra as z changed, especially between 0 and 2 mm (see Figure 4.45). This has serious implications for *in vivo* work. During ablation of plaque, for instance, the value of z is unlikely to be known. On the basis of the normalised spectra (see Figure 4.46) z = 2 mm was determined as the minimum distance for the fluorescence measurements.

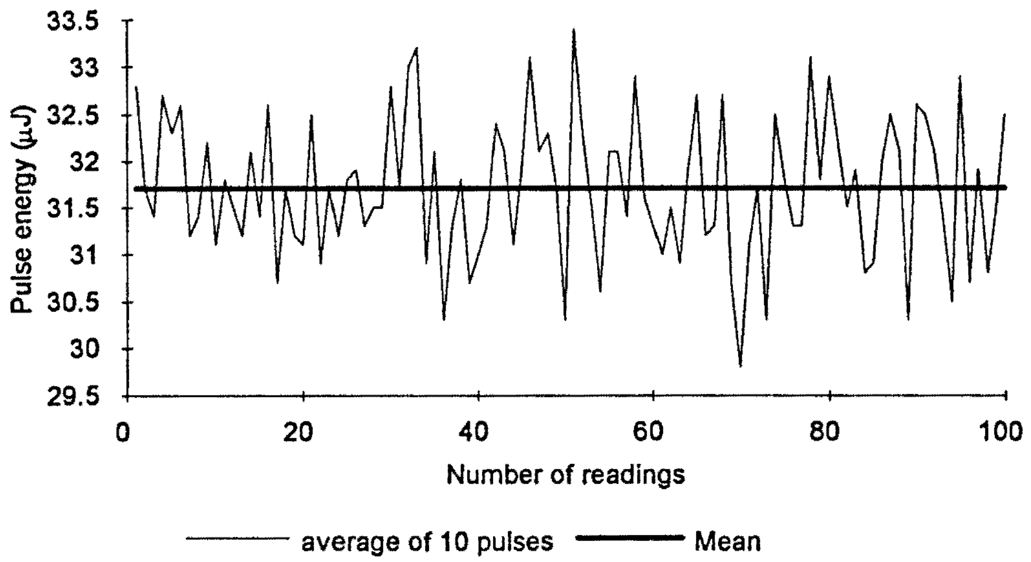

Figure 3.2 Output fluctuation of the XeCl laser at distal end of fibre. The average energy at the distal end of the fibre is indicated by the solid line.

The experiments were conducted with air as the medium between the fibres and the tissue sample. Slight variations in z (±0.2 mm) were unavoidable due to the uneven surface of the tissue sample. With this set-up, the energy density at the surface of the sample was $\approxeq$ 4 mJ/cm^2. Since the ablation threshold of vascular tissue is 2 J/cm^2 and is much larger than the energy density at the surface of the tissue, we are operating in the non-ablative regime.

The proximal tip of the fluorescence collection fibre is imaged onto the entrance slit of a scanning monochromator (SCHOEFFEL CN252; holographic gratings: 1180 Gr./mm, blaze: 240 nm, dispersion: 3.3 mm/nm). The monochromator was scanned between the wavelength range 300 nm to 600 nm unless otherwise stated. The scan rate of the monochromator was set at 100 nm/min. A band-pass cut-off filter (SCHOTT WG335) is placed before the entrance slit, in order to reduce interference from the scattered excitation radiation. The filter used allows 50% transmission at λ = 335 nm, indicating that the fluorescence response at wavelengths shorter than 335 nm was significantly attenuated. Although this attenuation was not compensated for, all the spectra are affected equally and valid comparison between profiles can be made.

A fast-risetime (2.2 ns) photomultiplier tube (HAMAMATSU R955) detects the dispersed light intensity. The photomultiplier has a spectral response in the wavelength region 160 nm to 930 nm and a peak response at λ = 400 nm (see APPENDIX E). The sensitivity of the photodetector is 68 mA/W.

The signal from the photomultiplier is sent via a coaxial cable to a Gated Integrator and Boxcar Averager (STANFORD RESEARCH SYSTEM SR250). In order to provide impedance matching and ensure distortion free transmission for the signal waveform, the coaxial cable was terminated with a 50 Ω resistor at the photomultiplier tube end and at the receiving end.

APPENDIX F describes the operation of a boxcar averaging system. The model SR250 Gated Integrator and Boxcar Averager is a versatile, high speed, low cost Nuclear Instrumentation Module (NIM) designed to recover fast analogue signals from noisy backgrounds. The SR250 system consists of a Gate Generator, a Fast Integrator, and Exponential Averaging Circuitry. The Gate Generator, triggered internally or externally, provides an adjustable delay from a few nanoseconds to 100 ms, before it generates a continuously adjustable gate of 2 ns to 15 μs

The Fast Gated Integrator integrates the input signal during the gating period. The output from the integrator is then normalised by the gate width to provide a voltage which is proportional to the average of the input signal during the sampling gate. This signal is further amplified and then sampled by a low droop sample and hold amplifier. This "LAST

SAMPLE" output allows the experimenter to do a pulse-by-pulse analysis of the signal being studied.

A moving Exponential Average of over 1 to 10 000 samples is available as the "AVERAGED OUTPUT". This averaging technique is useful for extracting small signals from noisy backgrounds. As one averages many noisy samples of a signal, the average will converge to the mean value of the signal, and the noise will average to zero. In the case of a random white noise background, the signal-to-noise (S/N) ratio increases as the square root of the number of samples in the average. This allows a S/N improvement of a factor of 100 using this technique alone.

The signal from the SR250 Gated Integrator and Boxcar Averager was digitised, recorded and displayed by an IBM 286 PC compatible computer. Fluorescence intensity at each wavelength was given in volts based on the amplitude of the signal detected by the photomultiplier and the boxcar averager and gated integrator system. Although the fluorescence intensities are an output measured as volts, throughout the text the fluorescence intensities are given in arbitrary units (a.u.). Further manipulation of the data is done under software control via the STANFORD RESEARCH SR270 program.

The boxcar was initiated by a trigger pulse from the laser and was gated to integrate the signal only during the fluorescence pulse (see Figure 3.3). Groups of pulses may be averaged in the boxcar averager to improve the signal. In all the experiments described below, the exponential moving average was set at 10 samples.

The wavelength calibration of the monochromator was verified with a mercury penlight lamp (SPECTROLINE QUARTZ PENCIL MODEL 11SC-1). In the wavelength region 300 nm to 600 nm, the measured wavelengths were within ±1 nm of the known mercury lines. The results are presented in Table 3.1.

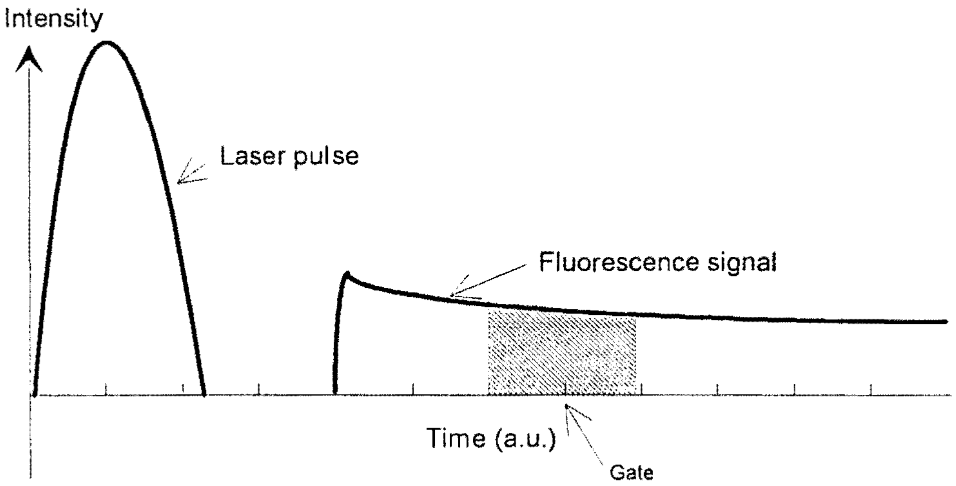

Figure 3.3 Sequence of events from onset of laser pulse to sampling the fluorescence signal

Table 3.1 Wavelength calibration of monochromator using a mercury source

Measured λ (± 0.5 nm)	Known λ (nm)
334.0	334.15
365.5	365.02
405.0	404.66
435.0	435.84
546.0	546.07
577.0	576.96

3.4 TISSUE SAMPLES

Human aorta, iliac, femorotibial (femoral and tibial) arteries were used as samples in this investigation. The aorta and iliac samples were extracted at postmortem examination from recently deceased patients. The postmortem interval varied from a few hours to a few days. The femorotibial arteries were obtained from surgically amputated limbs within 6 hours of the procedure.

The samples were obtained from three sources. The aorta samples (x14) were procured from the Department of Cardio-thoracic Surgery, Groote Schuur Hospital/University of Cape Town Medical School. The iliac artery samples (x13) were obtained from the South African Police Mortuary attached to the Tygerberg Hospital/University of Stellenbosch Medical School. The femorotibial artery samples (x21) were collected from the Department of Vascular Surgery, Tygerberg Hospital/University of Stellenbosch Medical School.

A summary of the sample population is presented in Table 3.2.

Table 3.2 Summary of sample population

Artery type	Artery population	Average age of patients (yr)	Age range (yr)
Femorotibial	21	61	27 - 78
Iliac	13	35	11 - 70
Aorta	14	29	9 - 52

Experiments were performed in a blinded manner in that the classification of the tissue (normal or stage of atherosclerosis) was not known at the time of the investigation.

In total, 88 arterial segments were analysed. The size of the segments varied but each was considerably larger than the excitation beam diameter at the point of irradiation.

The samples were transported and kept in an unfixed state in air at ambient temperature before irradiation by the XeCl laser. The experiments were performed within 2 hours of collection. The samples were investigated in air with the endothelium exposed to the laser beam. After study, the exact location from which the fluorescence was collected was marked with India ink. Each sample was then fixed in 10% formalin for preservation, histologic processing and thereafter light microscopy.

In the tissue processing phase the selected tissue was placed in tissue cassettes (LAB TEK) and processed in an automated tissue processor (SHANDON CITADEL 1000) through ascending grades of alcohol, xylene and finally into histological embedding wax (PARAPLAST PLUS). For histological examination, four sections, 4 µm thick, per sample were cut on a rotary microtome and mounted on glass microscope slides and dried prior to staining. Four sections were processed in the event of the need to use different stains to highlight features of the sample histology.

One section was stained with haematoxylin and eosin (HE) as it is permits the visual differentiation of a variety of tissue types. All HE staining was performed on a SHANDON LINISTAIN GLX automatic staining machine thus achieving constancy of tinctorial response. A modification of Mayer's haemalum (Kiernan, 1990) and 1% aqueous eosin was used.

The slides were viewed with a light microscope (ZEISS PHOTOMICROSCOPE II) and 35 mm photomicrographs (using KONICA 50 ASA film) were made of selected slides.

The samples were classified as normal or atherosclerotic. The atherosclerotic tissue was further classified according to the scheme suggested by Stary (1992b). Table 3.3 describes this classification of human atherosclerotic lesions.

Throughout the text, the atherosclerotic types suggested by Stary (1992b) are referred to as Stary types.

Table 3.3 Classification of human atherosclerotic lesions (from Stary, 1992b)

Classification of atherosclerotic lesion types based on microscopic and chemical composition			**Conventional terms based on appearance with the unaided eye**	**Comments**
Recommended terms		**Description**		
Type I	(intimal lesion)	Lipoprotein accumulation in intima; lipid in macrophages; these changes discernable only microscopically or chemically; no tissue damage	None	Types I and II are sometimes combined as "early lesions"
Type II	(fatty streak)	Lipoprotein accumulation in intima; lipid in macrophages and smooth muscle cells; quantities large enough to be visible to the unaided eye but still no tissue damage	Fatty streak	
IIa	(progression-prone: colocalized with specific adaptive thickening)			
IIb	(progression-resistant)			
Type III	(preatheroma)	All type IIa changes plus multiple deposits of pooled extra-cellular lipid; microscopic evidence of tissue damage and disorder	None	An "intermediate" or "transitional" lesion had been suspected
Type IV	(atheroma)	All type IIa changes plus confluent mass of extracellular lipid (lipid core) with massive structural damage to intima	Fibrous plaque; fibrolipid plaque; plaque	Types IV to VIII are sometimes combined as "advanced lesions"
Type V	(fibroatheroma)	All type IV changes plus development of marked collagen and smooth muscle cell increase (cap) above lipid core		
Type VI	(complicated fibroatheroma)	All type V changes plus a thrombotic deposit, and/or haemorrhage, and/or erosion or fissure	Complicated plaque	
VIa	(thrombo-haemorrhagic)			
VIb	(thrombotic)			
VIc	(haemorrhagic)			
Type VII	(calcific lesion)	Any advanced lesion type composed predominantly of calcium; substantial structural deformity	Calcified plaque	
Type VIII	(fibrotic lesion)	Any advanced lesion type composed predominantly of collagen; lipid may be absent	Fibrous plaque	

3.5 FIBRE GEOMETRY

The area of the sample exposed by the excitation beam, A_e, is given by:

$$A_e = \pi(z \tan a)^2$$

where a is defined as the acceptance angle of the fibre (see Figure 3.4).

The overlap area, A, of the directly irradiated area and the imaged area is calculated as follows (see Figure 3.5):

$$\begin{aligned} A &= 4 \times \left(\left(\int_0^{x_1} \sqrt{r^2 - x^2}\,dx\right) - x_1\sqrt{r^2 - x_1^2}\right) \\ &= 4 \times \left(0.5 \times \left[x\sqrt{r^2 - x^2} + r^2 \sin^{-1}\frac{x}{r}\right]_0^{x_1} - x_1\sqrt{r^2 - x_1^2}\right) \\ &= 2 \times \left(r^2 \sin^{-1}\frac{x_1}{r} - x_1\sqrt{r^2 - x_1^2}\right) \end{aligned}$$

where

r is the radius of the circle subtended by the acceptance angle and $d = 1$ mm is the distance between the centres of the delivery fibre and the collection fibre. Both are related by

$$x_1 = \sqrt{r^2 - \frac{1}{4}d^2} \quad \text{and} \quad r = z \tan a$$

Figure 3.6 illustrates the variation of A with z.

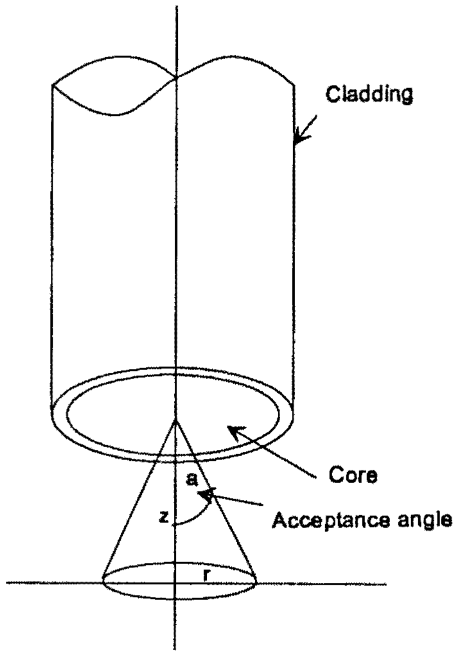

Figure 3.4 Illustration of acceptance angle of fibre

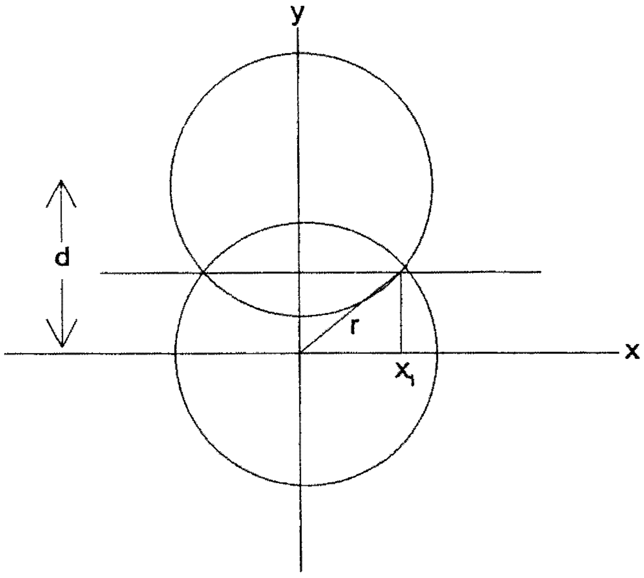

Figure 3.5 Geometry of imaged area

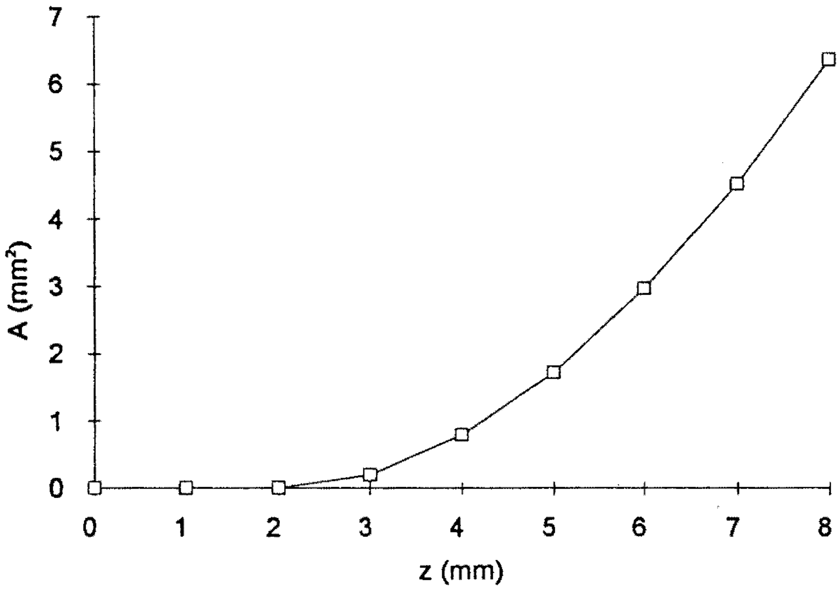

Figure 3.6 Variation of A with z

From Figure 3.6 it can be seen that the fluorescence collection fibre sees the irradiated tissue for $z > 2$ mm.

CHAPTER 4

RESULTS AND ANALYSIS

4.1 HISTOLOGY OF TISSUE SAMPLES

Table 4.1 contains a description and histological classification of the tissue samples. Of the 88 samples that were investigated, 51 of the samples could be classified as either normal or atherosclerotic.

Photomicrographs representing normal, Stary types I, I-II, III, IV, V, VIa, VIc, VII, VIII and arteriosclerosis are shown in Figures 4.1 to 4.10. Some remarks need to be made about the photomicrographs. Postmortem human material always demonstrates significant autolytic and putrefactive changes because of delays before fixation. A result is that the microscopic cellular details which largely define Stary types I - III are blurred. Stary types IV-VIII are not affected as much because they are less susceptible to autolysis. This means that Stary types I-II are more difficult to photograph clearly in autolysed material (these samples) than Stary types III-VIII.

Non-genetic atherosclerosis progresses over decades from Stary types I-II in childhood to Stary types V - VIII in adults. Two samples in this series were from children aged 9 and 11 years. Ages ranged from 19 to 78 for the other samples. There were no samples from young children. This is the reason why early atherosclerosis is not well represented in the series.

The population of the normal and atherosclerotic tissue classifications is shown in Table 4.2. It can be seen from this table that the majority of atherosclerotic samples are not restricted to a single Stary type but to a combination of Stary types. Some of the samples were not classifiable. Furthermore, the histology of the tissue samples shows that the tissue properties can vary considerably within a few μm along the tissue. This gives an indication of the heterogeneous nature of arterial tissue. It should also be noted that a large proportion of samples (35%) was classified as arteriosclerotic. Arteriosclerosis is a disease of the media and was not subject to the present study.

Almost all of the samples classified as normal were aorta samples. Iliac samples had classifications in almost all the Stary types. Femorotibial samples were mainly Stary types V - VIII. The histologic classification of the femorotibial arteries (obtained from surgically amputated limbs) confirms the advanced atherosclerotic state of the tissue.

Table 4.1 Histologic analysis of samples (list of abbreviations given at foot of table)

Sample #	Patient #	A.T.	Sex	Age (yr)	P.M.I.	HISTOLOGIC CLASSIFICATION
1	1	AO	M	28	UK	Arteriosclerosis
2	1	AO	M	28	UK	Almost normal
3	2	AO	M	9	UK	Normal
4	2	AO	M	9	UK	Normal
5	3	AO	M	30	UK	Almost normal
6	3	AO	M	30	UK	Stary IIa - III
7	4	AO	M	31	UK	Stary II
8	4	AO	M	31	UK	Stary III
9	5	AO	M	44	5 h	Stary VIc
10	6	FT	F	78	< 6 h	Stary VIc - VIII
11	6	FT	F	78	< 6 h	Probably Stary VIII. Very fragmented
12	7	AO	F	30	41 h	Hypertensive + medial arteriosclerosis
13	8	FT	M	72	< 6 h	Medial arteriosclerosis + Stary VI i.e. VI + VIII
14	9	FT	M	45	< 6 h	Unclassifiable
15	10	FT	M	67	< 6 h	Stary VII - VIII
16	11	FT	M	47	< 6 h	Hypertensive arteriosclerosis, intimal fibrosis + hyalinisation
17	12	FT	F	55	< 6 h	Stary VIa + arteriosclerosis (calcified media)
18	12	FT	F	55	< 6 h	Stary VIII
19	13	FT	M	65	< 6 h	Stary VI - VIII
20	13	FT	M	65	< 6 h	Unclassifiable
21	14	FT	M	59	< 6 h	Hypertensive arteriosclerosis, intimal fibrosis + hyalinisation
22	15	FT	M	66	< 6 h	Stary VIc and VIII
23	15	FT	M	66	< 6 h	Stary VIII

Table 4.1 (continued)

Sample #	Patient #	A.T.	Sex	Age (yr)	P.M.I.	HISTOLOGIC CLASSIFICATION
24	16	FT	M	65	< 6 h	Stary VII
25	17	FT	M	50	< 6 h	Hypertensive arteriosclerosis
26	17	FT	M	50	< 6 h	Unclassifiable
27	17	FT	M	50	< 6 h	Hypertensive arteriosclerosis
28	18	FT	F	73	< 6 h	Stary VIII
29	18	FT	F	73	< 6 h	Severe medial arteriosclerosis + Stary VII
30	18	FT	F	73	< 6 h	Severe medial arteriosclerosis
31	18	FT	F	73	< 6 h	Stary VIII + V
32	19	FT	M	65	< 6 h	Stary VII
33	19	FT	M	65	< 6 h	Severe medial arteriosclerosis + Stary VI - VII
34	20	FT	M	27	< 6 h	Mild hypertensive arteriosclerosis
35	20	FT	M	27	< 6 h	Mild hypertensive arteriosclerosis
36	21	AO	F	45	2 days	Hypertensive arteriosclerosis
37	21	AO	F	45	2 days	Normal
38	21	AO	F	45	2 days	Normal
39	22	AO	M	20	27 h	Stary III - IV
40	23	AO	M	25	22 h	Normal
41	24	IL	F	70	5 days	Stary I - II
42	24	IL	F	70	5 days	Medial arteriosclerosis
43	25	IL	F	19	32 h	Hypertensive arteriosclerosis.
44	26	IL	M	56	3 days	Severe hypertensive arteriosclerosis + Stary VIII
45	27	IL	M	21	3 days	Mild hypertensive arteriosclerosis
46	27	IL	M	21	3 days	Hypertensive arteriosclerosis
47	28	IL	M	19	4 days	Mild hypertensive arteriosclerosis

Table 4.1 (continued)

Sample #	Patient #	A.T.	Sex	Age (yr)	P.M.I.	HISTOLOGIC CLASSIFICATION
48	29	FT	M	71	< 6 h	Mild hypertensive arteriosclerosis
49	29	FT	M	71	< 6 h	Mild/moderate hypertensive arteriosclerosis.
50	29	FT	M	71	< 6 h	Unclassifiable
51	29	FT	M	71	< 6 h	Stary VII
52	30	FT	M	64	< 6 h	Stary VII + VIII
53	31	IL	M	30	12 h	Mild hypertensive arteriosclerosis.
54	32	IL	M	32	32 h	Mild/moderate hypertensive arteriosclerosis.
55	32	IL	M	32	32 h	Severe/mild hypertensive arteriosclerosis + Stary III - IV
56	33	IL	F	11	10 h	Mild/moderate hypertensive arteriosclerosis
57	33	IL	F	11	10 h	Mild/moderate hypertensive arteriosclerosis
58	33	IL	F	11	10 h	Mild/moderate hypertensive arteriosclerosis
59	33	IL	F	11	10 h	Almost normal
60	34	IL	M	35	2 days	Almost normal
61	34	IL	M	35	2 days	Mild hypertensive arteriosclerosis
62	34	IL	M	35	2 days	Moderate hypertensive arteriosclerosis + Stary II - III
63	34	IL	M	35	2 days	Severe/moderate hypertensive arteriosclerosis + Stary II - III
64	35	AO	M	35	34 h	Mild hypertensive arteriosclerosis
65	35	AO	M	35	34 h	Mild hypertensive arteriosclerosis
66	35	AO	M	35	34 h	Mild hypertensive arteriosclerosis
67	35	AO	M	35	34 h	Mild hypertensive arteriosclerosis
68	36	AO	M	35	12 h	Stary I-II + mild hypertensive arteriosclerosis
69	36	AO	M	35	12 h	Stary I-II
70	37	IL	F	54	2 days	Stary VII-VIII
71	37	IL	F	54	2 days	Stary VIII

Table 4.1 (continued)

Sample #	Patient #	A.T.	Sex	Age (yr)	P.M.I.	HISTOLOGIC CLASSIFICATION
72	37	IL	F	54	2 days	Stary VII. Very fragmented
73	38	IL	M	30	14 h	Hypertensive arteriosclerosis
74	39	IL	M	49	2 days	Stary V (fibroatheroma)
75	40	IL	F	28	2 days	Probably Stary VIII
76	41	FT	F	68	< 6 h	Stary VII
77	41	FT	F	68	< 6 h	Stary VII + VIII
78	42	FT	M	78	< 6 h	Unclassifiable
79	42	FT	M	78	< 6 h	Stary V + medial arteriosclerosis
80	43	FT	M	49	< 6 h	Stary VII + VIII
81	44	FT	M	59	< 6 h	Stary VII + VIII
82	45	FT	M	27	< 6 h	Unclassifiable
83	45	FT	M	27	< 6 h	Unclassifiable
84	46	AO	M	39	24 h	Normal
85	46	AO	M	39	24 h	Normal
86	47	AO	M	52	17 h	Normal
87	47	AO	M	52	17 h	Normal
88	48	AO	M	28	UK	Normal

Abbreviations used in table above are:

AO:	Aorta
A.T.:	Artery type
F:	Female
FT:	Femorotibial
h:	hours
IL:	Iliac
M:	Male
P.M.I.:	Post mortem interval
UK:	Unknown
yr:	years

Table 4.2 Population of normal and atherosclerotic tissue types

Tissue type (Stary)	Tissue population
Normal	14
I	-
II	1
IIa	-
IIb	-
III	1
IV	-
V	3
VI	1
VIa	1
VIb	
VIc	1
VII	6
VIII	5
I-II	3
II-III	2
IIa-III	1
III-IV	2
VI-VII	1
VI-VIII	1
VIc-VIII	2
VII-VIII	6
Arteriosclerosis	30
Unclassifiable	7

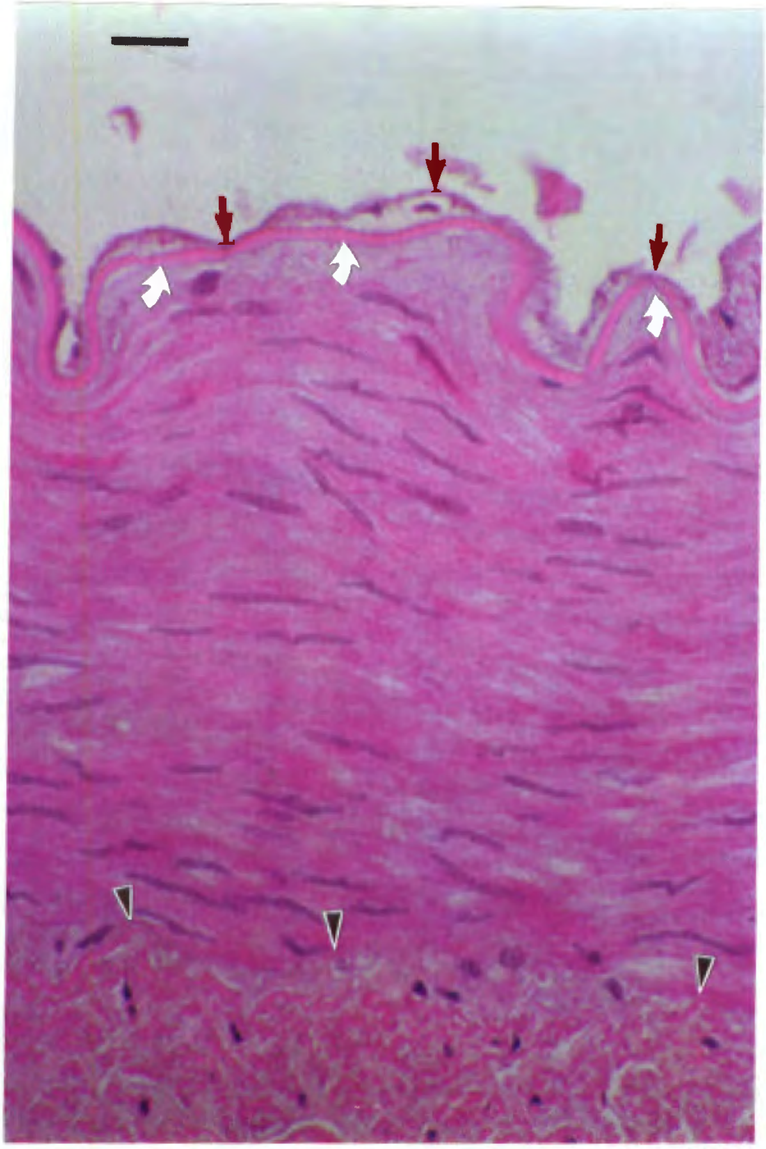

Scan 490. Hist 264/92. Film C189/16.

Figure 4.1 Normal muscular artery. Peripheral branch of iliac artery from an 11 year old girl (sample #59). Post mortem interval 10 h. The endothelium (red arrows) and the internal elastic lamina (white arrows) are either in contact or separated by a narrow space. The cells in the media are smooth muscle cells and the arrowheads indicate the external elastic lamina and the begining of the adventitia. Stain HE. Magnification x 320. Bar = 23.8 μm.

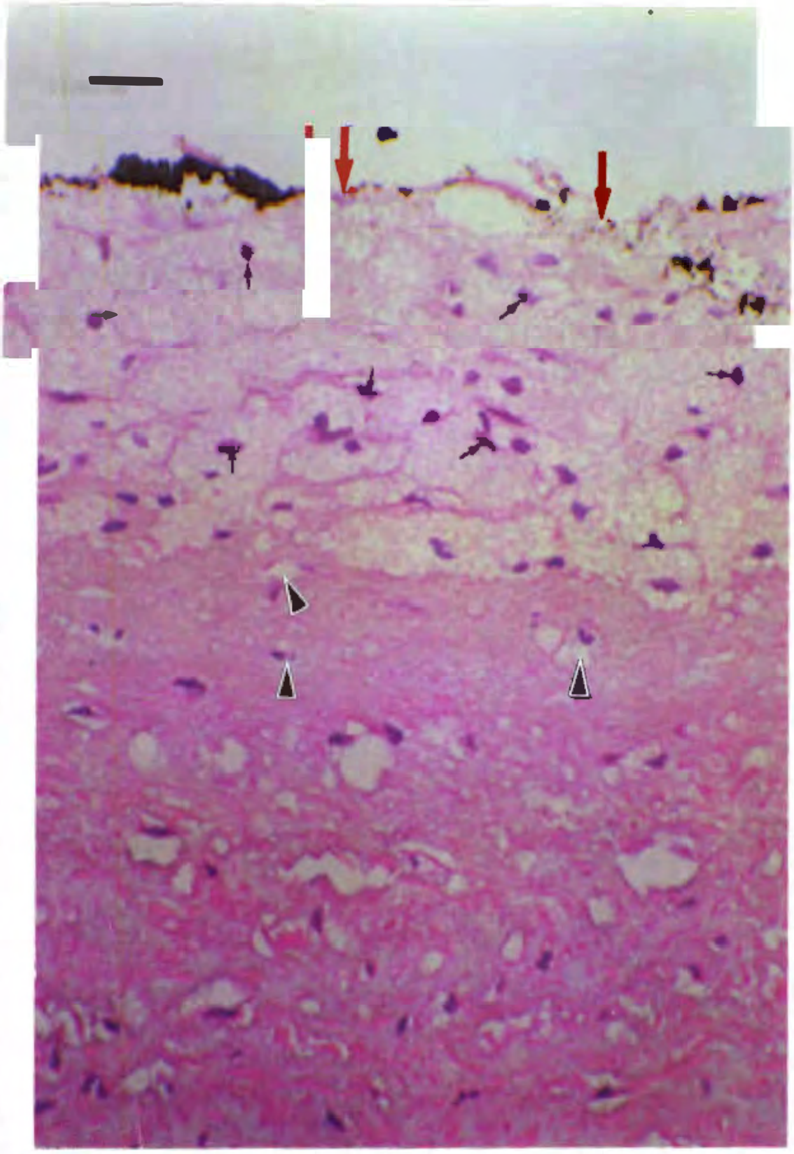

Scan 523. Hist 274/9.2 Film C189/4.

Figure 4.2 Stary type I-II (fatty streak). Aortic atherosclerosis. Microscopy suggests endothelial sloughing (red arrows) and confirms subendothelial foam cells typical of monocytes which have transformed to macrophages and phagocytised lipid (black arrows). Lipid stains such as oil red O would demonstrate this lesion as a fatty streak with minimal intimal distortion, like elevation. Some smooth muscle cells containing lipid may also be present (arrowheads). Tissue damage is minimal. Aorta from a 35 year old man (sample #68). Postmortem interval 12 h. Stain HE. Magnification x 320. Bar = 23.8 μm.

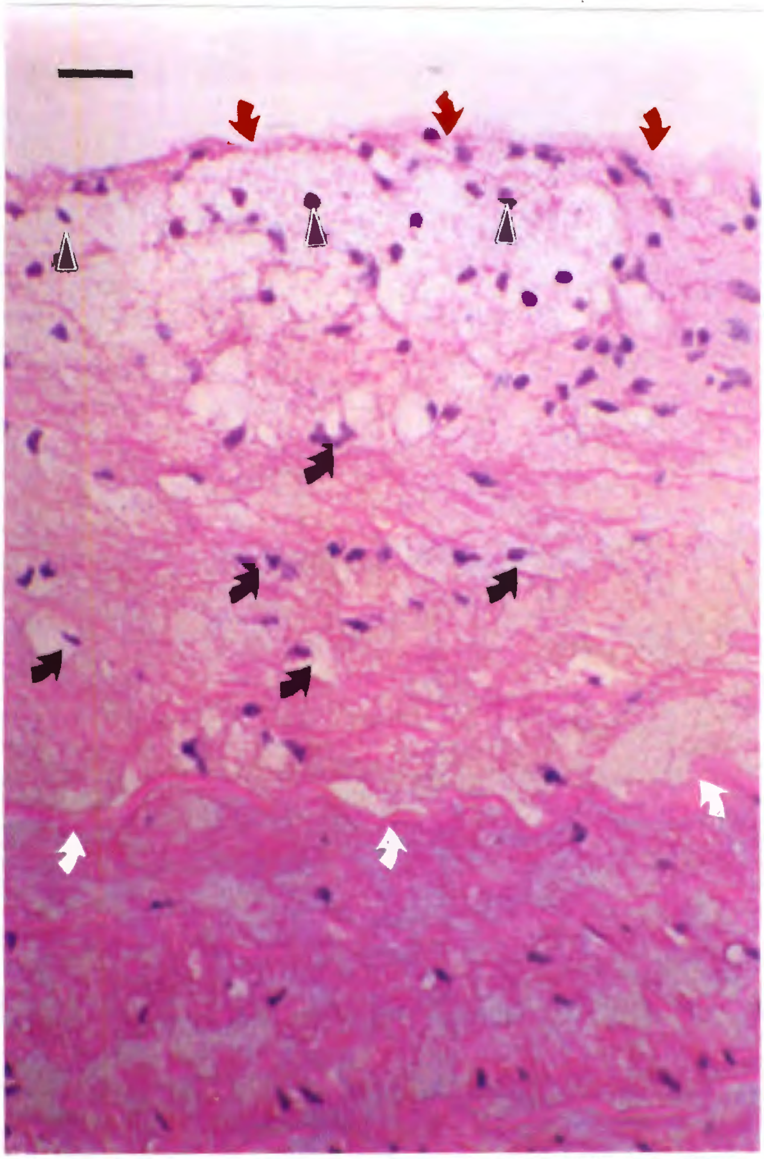

Scan 366. Hist 174/92. Film C188/12.

Figure 4.3 Stary type III (preatheroma). Aortic atherosclerosis. The intima is demarcated by the endothelium, which demonstrates sloughing (red arrows), and the internal elastic lamina (white arrows). The subendothelial foam cells (arrowheads) are typical of monocyte macrophages, and those which lie deeper may be smooth muscle cells (black arrows) modulated to secrete the type of extracellular matrix filling the rest of the intima. Aorta from a 20 year old man (sample #39). Post mortem interval 27 h. Stain HE. Magnification x 320. Bar = 23.8 μm.

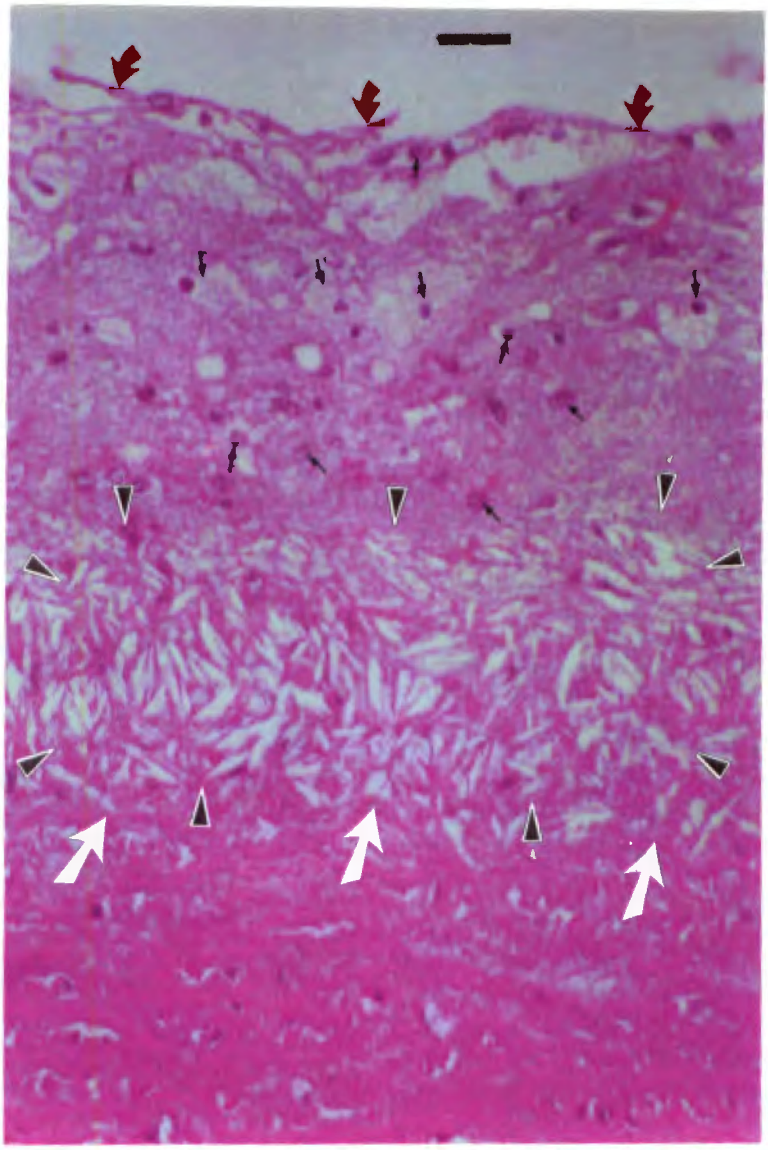

Scan 177. Hist 141/92. Film C189/6.

Figure 4.4 Stary type IV (atheroma). Aortic atherosclerosis. The intima between the endothelium (red arrows) and the internal elastic lamina (white arrows) shows massive structural damage, including the lipid core (arrowheads) and infiltrating inflammatory cells (small black arrows). However, there is no fibrous cap. Aorta from a 20 year old man (sample #39). Post mortem interval 27 h. Stain HE. Magnification x 320. Bar = 23.8 μm.

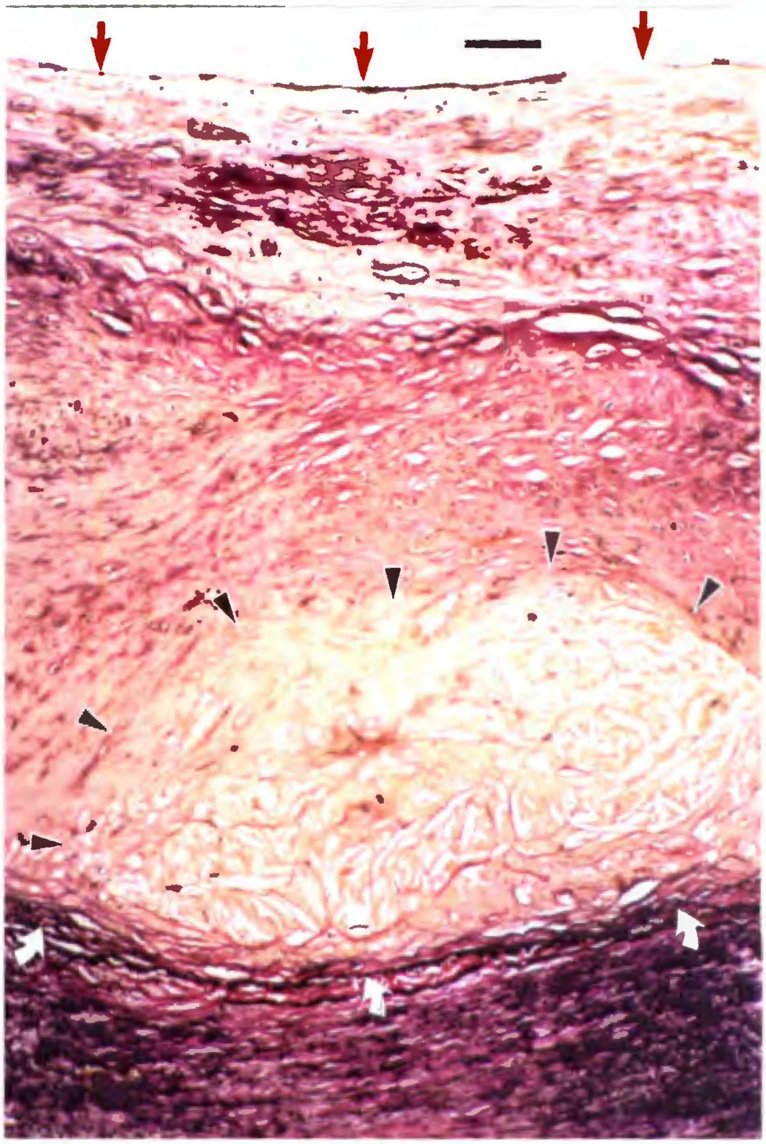

Scan 258. Hist 258/92 Film C188/7.

Figure 4.5 Stary type V (fibroatheroma). Peripheral atherosclerosis. The intima is demarcated by the endothelium (red arrows) and the internal elastica lamina (white arrows). The extent of intimal thickening is indicated by the fact that endothelium and internal elastic lamina are usually adjacent. An atheromatous core (arrowheads) contains numerous cholesterol crystals, indicating accumulated extracellular lipid. The rest of the thickened intima consists of connective tissue matrix, which typically contains collagens, proteoglycans and elastic fibres. Smooth muscle cells can secrete these proteins, as well as growth regulatory molecules and cytokines, after changing to a secretory phenotype (Ross, 1993). Iliac artery from a 49 year old man (sample #74). Post mortem interval 2 days. Stain EVG (combined Verhoeffs and Van Gieson's methods for connective tissue and elastin = elastic Van Gieson). Magnification x 320. Bar = 23.8 μm.

Scan 274. Hist 133/92. Film C188/15.

Figure 4.6 Stary type VIa (complicated thrombo haemorrhagic fibroatheroma). Peripheral atherosclerosis. The plaque of this fibroatheroma is complicated by a mural endothelial thrombus (red arrows) and internal haemorrhage (white arrows). Within the plaque there are elongated smooth muscle cells and mononuclear cells (arrowheads) which are probably macrophage foam cells. Femorotibial artery from a 55 year old woman (sample #17). Post mortem interval < 6 h. Stain HE. Magnification x 125. Bar = 58 μm.

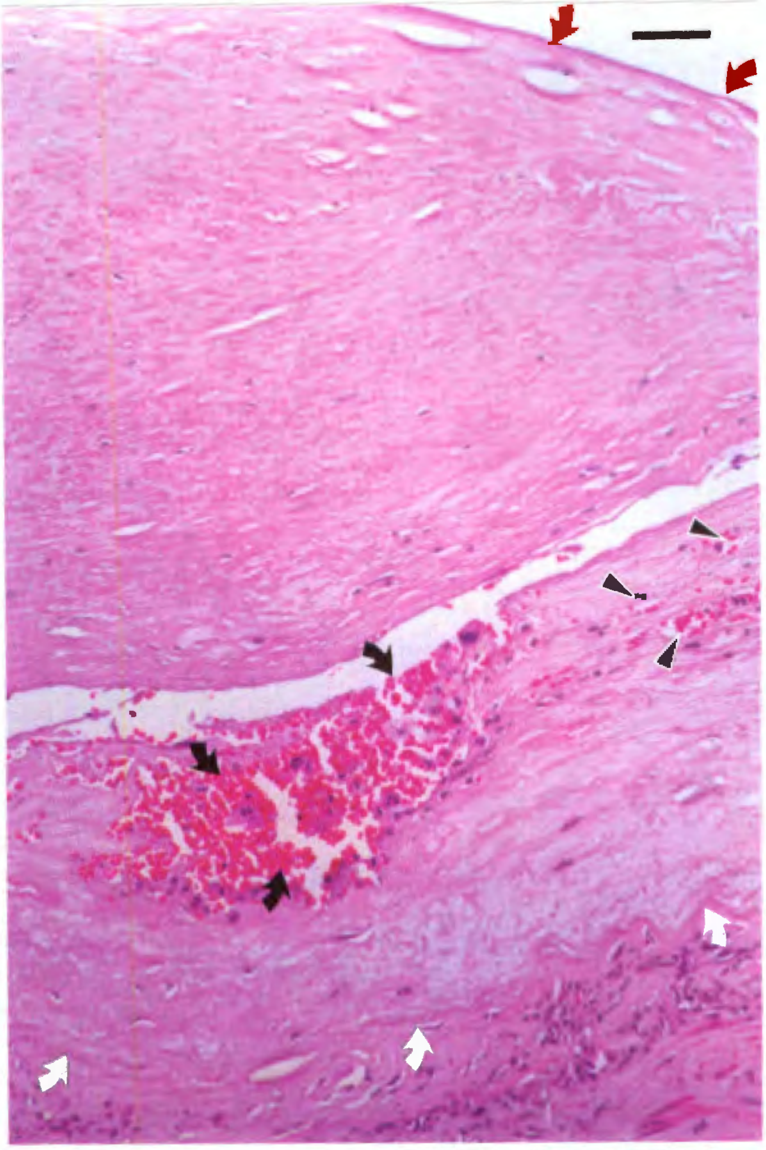

Scan 284. Hist 176/92. HE stain. Film C188/18.

Figure 4.7 Stary type VIc (complicated haemorrhagic fibroatheroma). Peripheral atherosclerosis. The intima is demarcated by the endothelium (red arrows) and the internal elastic lamina (white arrows). This fibroatheroma is complicated by haemorrhage (black arrows). Angiogenesis has resulted in secondary vascularisation of the plaque (arrowheads). When these channels bleed due to fissuring or ulceration, thrombi form and contribute to terminal myocardial, cerebral and peripheral infarctions (Ross, 1993). Femorotibial artery from a 66 year old man (sample #22). Stain HE. Post mortem interval < 6 h. Magnification x 125. Bar = 58 μm.

Scan 602. Hist 44/94. Film C188/5.

Figure 4.8 Stary type VII (calcified plaque). Peripheral atherosclerosis. The intima which is demarcated by red and white arrows, consists of of fibrous plaque overlying massive calcification. There is substantial deformity because the intima is thicker than the media, which is the layer of smooth muscle below the white arrows. In contrast, healthy, unthickened intima is a few microns deep. The changes demonstrated imply total loss of physiological vasomotor control to shunt peripheral circulation according to demand, which is why intermittent claudication is a symptom of peripheral atherosclerosis. Femorotibial artery from a 68 year old woman (sample #76). Stain HE. Post mortem interval < 6 h. Magnification x 50. Bar = 145 µm.

Scan 284. Hist 176/92. Film C189/13.

Figure 4.9 Stary typeVIII (fibrotic lesion = fibrous plaque). Peripheral atherosclerosis. The intima between the endothelium (red arrows) and internal elastic lamina (arrowheads) is a fibrous mass composed mainly of extracellular matrix, which is probably collagen. There is no discernible lipid. Femorotibial artery from a 66 year old man (sample #23). Post mortem interval < 6 h. Stain HE. Magnification x 50. Bar = 145 µm.

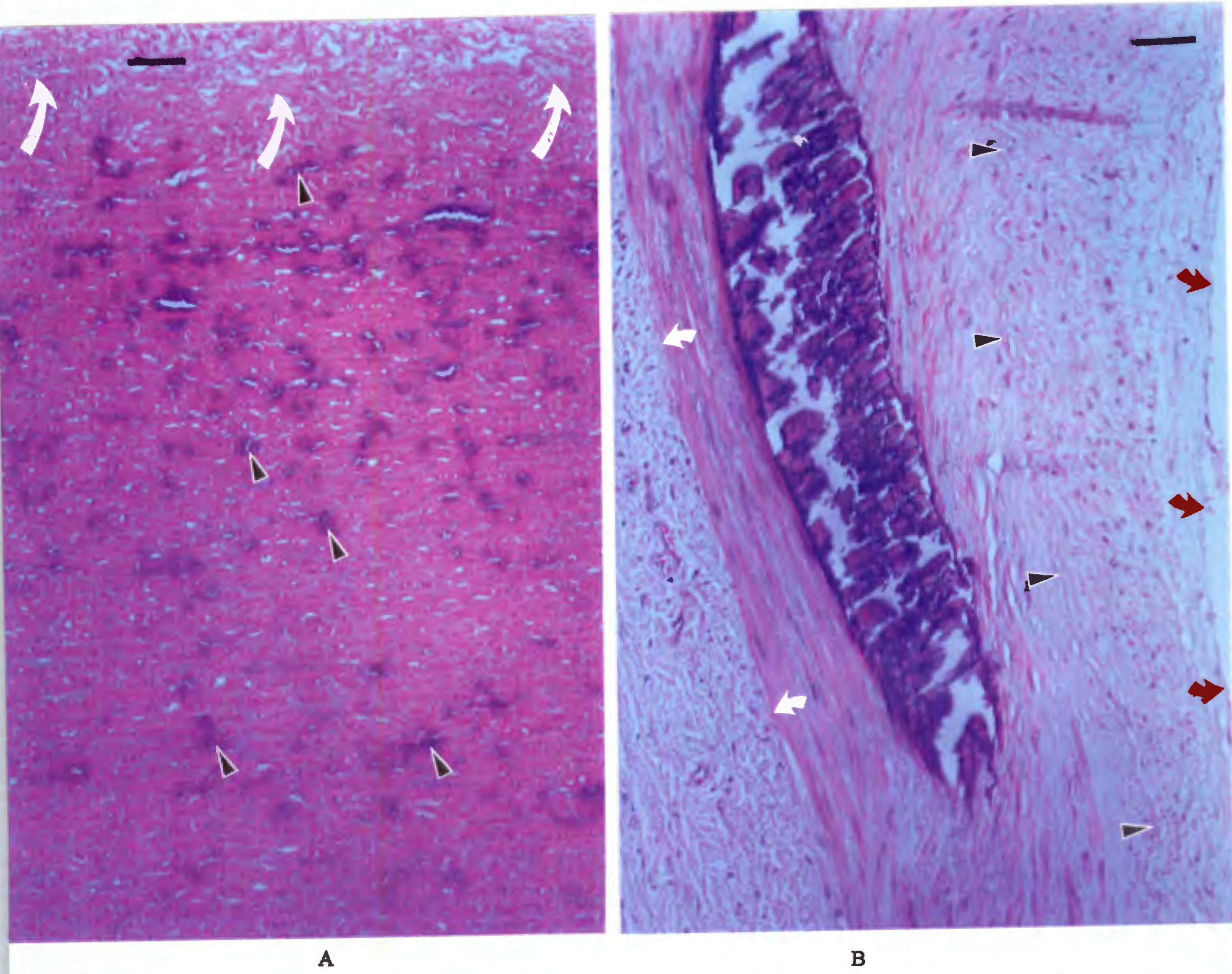

A = scan 254, Hist 143/92. B = scan 260, Hist 148/92. Film C189/9 (A) and C189/10 (B).

Figure 4.10 Arteriosclerosis. A and B demonstrate arteriosclerosis of different severity. The white arrows in A show the elastica externa and the start of the adventitia, and the arrow heads indicate foci of calcification. In B there is a solid mass of calcium in the media: red arrows = endothelium, arrowheads = internal elastic lamina, and white arrows = external elastic lamina. A = aorta of a 30 year old woman (sample #12) with a post mortem interval of 41 h. B = femorotibial artery of a 72 year old man (sample #13) with a post mortem interval of < 6 h. Magnification x 125. Bars = 58 µm. Stain HE.

4.2 PERFORMANCE CHARACTERISTICS OF MEASURING SYSTEM

The following experiments were performed to determine the performance characteristics of the measuring system and thereby optimise the settings of the system for fluorescence measurements.

4.2.1 Cut-off filter

Three colourless ultraviolet cut-off longpass filters viz. SCHOTT WG320, SCHOTT WG335 and SCHOTT WG345 were evaluated to determine which filter was best suited to reduce the interference from the scattered primary radiation. The filters were placed in front of the entrance slit of the monochromator. The fluorescence spectra (spectral intensities normalised to intensity at $\lambda = 360$ nm) of the sample (muscle) measured with no filter and with the above-mentioned filters are shown in Figure 4.11. The results demonstrate that although there is complete attenuation of the fluorescence intensity in the wavelength region below the cut-off wavelength, the spectra exhibited essentially the same spectral features. It appears that the scattered radiation has no marked effect on the fluorescence spectra. However, the filter has to be used to protect the photomultiplier from reflected radiation. The SCHOTT WG335 filter was used in all the subsequent fluorescence measurements.

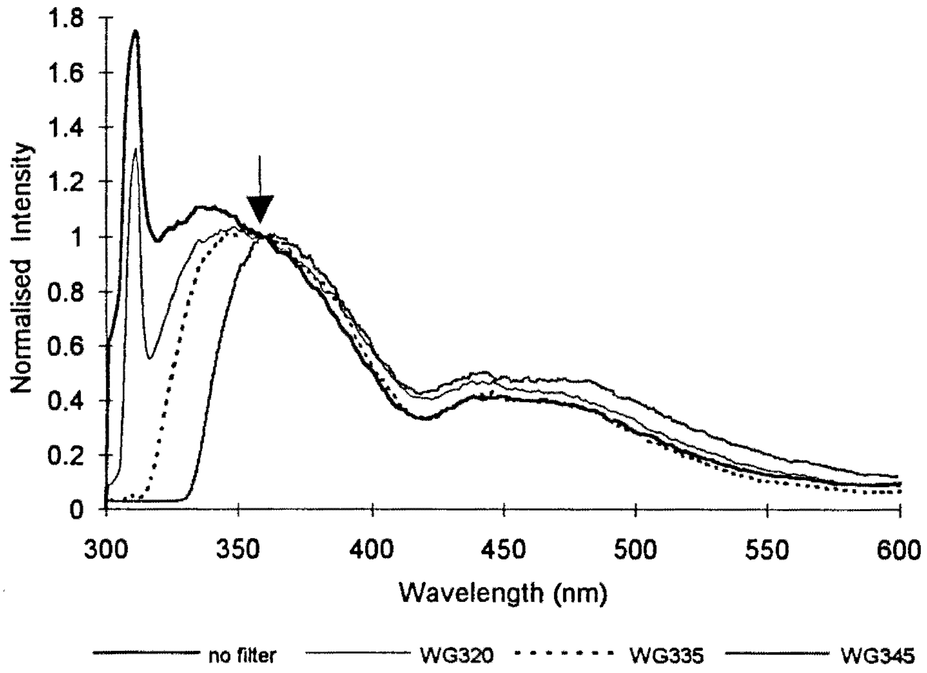

Figure 4.11 Effect of filters on the fluorescence lineshape (spectral intensities normalised to intensity at $\lambda = 360$ nm)

4.2.2 Photomultiplier tube voltage

The photomultiplier tube (PMT) voltage was varied to determine a suitable voltage to choose for the experiments. The results of varying the voltage are shown in Figure 4.12a (actual measurements) and Figure 4.12b (normalised spectra). An observation that reflects the relation between voltage applied to the PMT and the work function of its components is that, for the voltage range used, as the PMT voltage decreases, the fluorescence spectral intensities also decreases (see Figure 4.12a). When the spectral intensities are normalised to the fluorescence intensity at λ = 360 nm, there is, in general, a decrease in the normalised intensity with decreasing voltage (see Figure 4.12b). Examination of Figure 4.12b also indicates that there is an apparent levelling of the fluorescence spectra as a function of voltage. This is due to the sequence in which each of the scans was performed and the dependence of the fluorescence intensities on exposure of the sample (arterial tissue) to XeCl laser radiation (see section 4.3.2) and not as a result of a malfunction of the PMT. The spectrum corresponding to each of the chosen PMT voltages was acquired in the following order: 800V, 700V, 600V, 500V, 900V. A PMT voltage of 800V (arbitrary choice) was chosen for all the experiments.

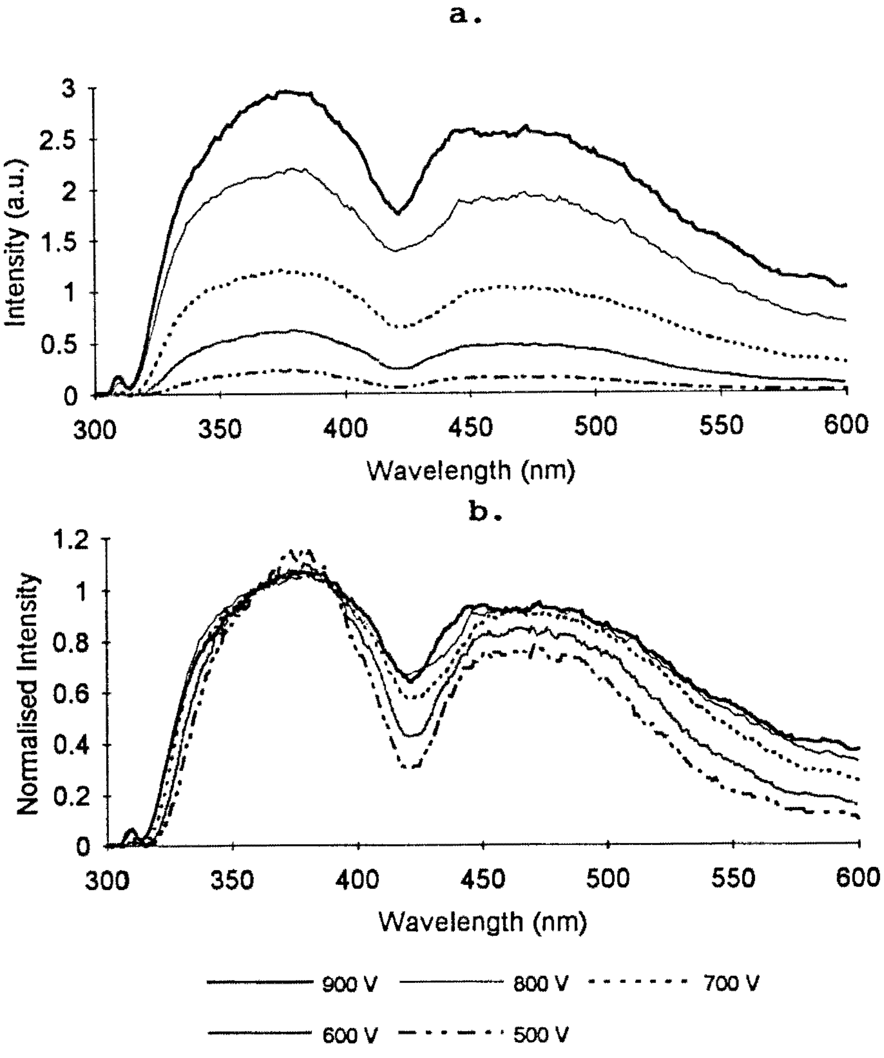

Figure 4.12 Change in fluorescence lineshapes as a result of varying the PMT voltage. **a**: actual fluorescence measurements. **b**: spectral intensities normalised to intensity at λ = 360 nm

4.2.3 DELAY

The delay between the onset of the laser pulse and sampling the fluorescence signal is equal to the delay scale setting plus a 25 ns trigger discriminator delay (see Figure 3.3). This trigger discriminator delay is inherent in the STANFORD 250 boxcar averager and integrator system. The effect of varying the delay is shown in Figure 4.13a (actual measurements) and Figure 4.13b (normalised spectra). The fluorescence intensity is constant for delay settings ≤1 µs from the onset of the laser pulse. Based on these observations, we assume that the gate is positioned on the tail of the fluorescence pulse. There is a noticeable reduction in the spectral intensities when the delay is set at 10 µs. At delay times ≥ 100 µs there is a complete decay of the fluorescence signal. A delay setting of 10 ns was used for all the experiments.

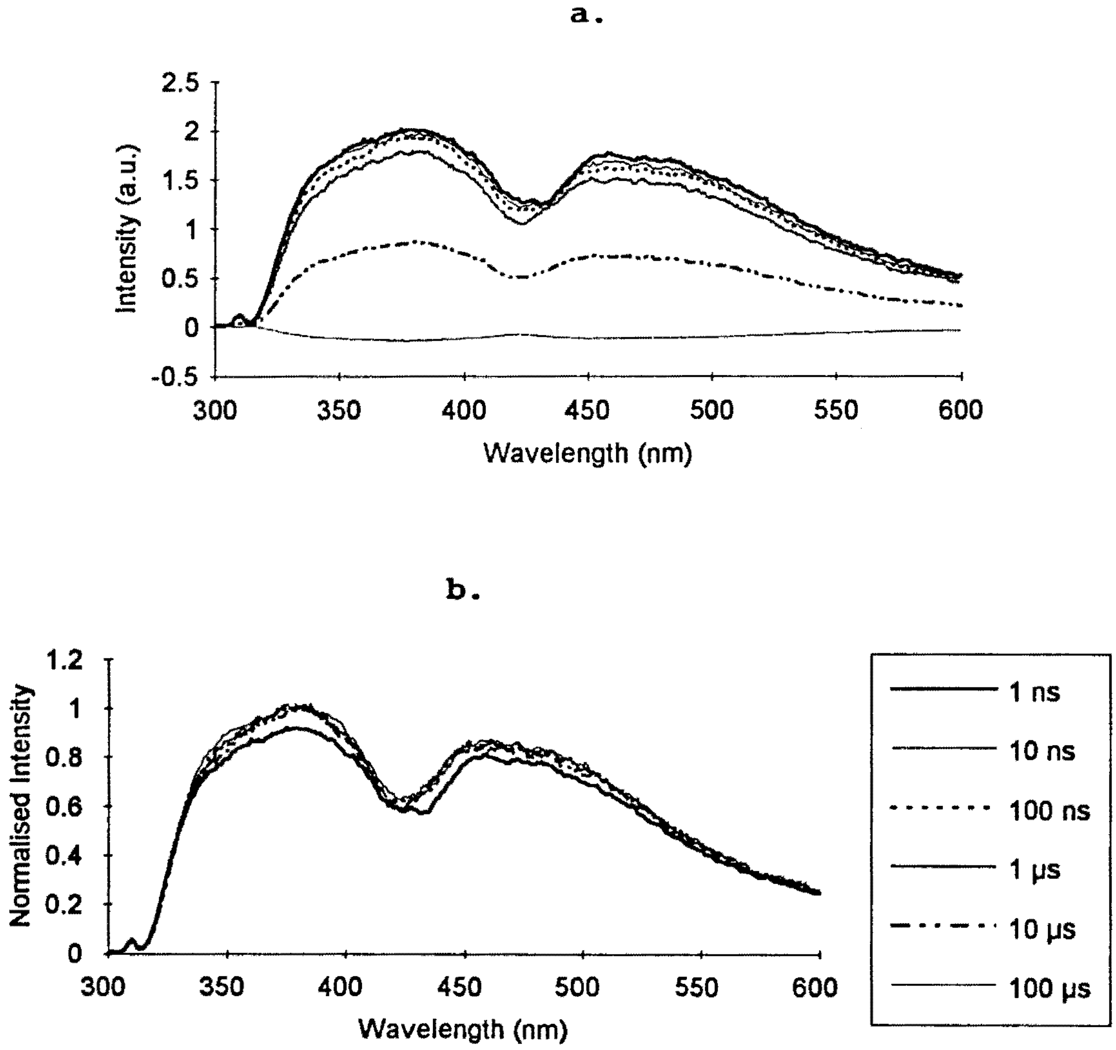

Figure 4.13 Effect of varying delay times between onset of laser pulse and fluorescence measurement. **a:** actual measurements. **b:** spectral intensities normalised to intensity at $\lambda = 380$ nm

4.2.4 Gate width

The output from the integrator is normalised by the gate width to provide a voltage which is proportional to the average of the input signal during the sampling gate. The effect of varying the gate width is shown in Figure 4.14a (actual measurements) and Figure 4.14b (normalised spectra). The gate widths did not have an appreciable effect on the fluorescence lineshape except at the gate width of 1 ns where the fluorescence intensities are significantly lower and are very noisy in the wavelength region ≈ 365 nm to ≈ 395 nm. A gate width of 10 ns was used in all the experiments.

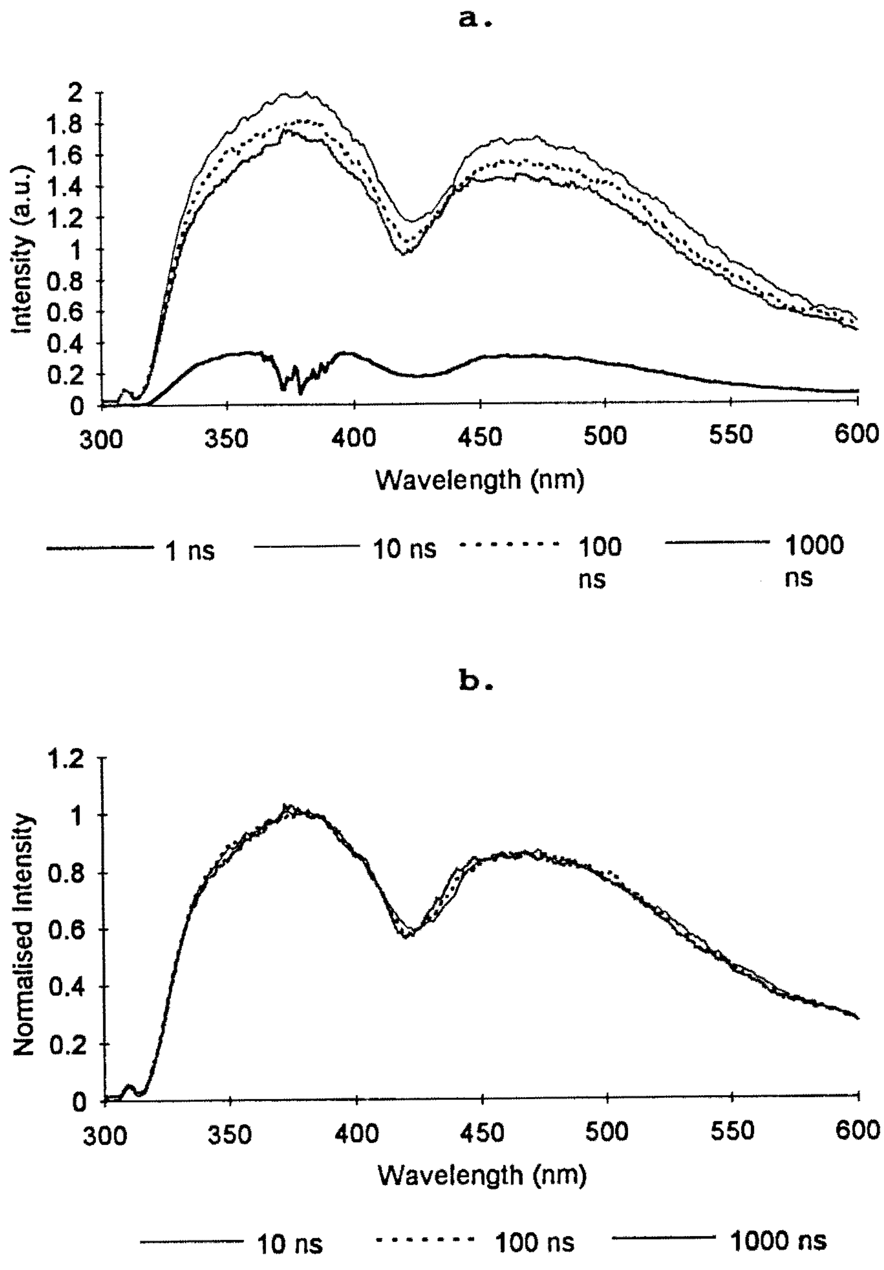

Figure 4.14 Effect of varying gate width. a: actual fluorescence measurements. b: spectral intensities normalised to intensity at $\lambda = 380$ nm

4.2.5 Monochromator slit width

In this experiment the entrance slit width of the monochromator was kept fixed at 1 mm. The exit slit width of the monochromator was varied in steps of 0.5 mm. The effect of changing the slit width did not significantly alter the fluorescence signal as can be seen by examining the normalised fluorescence spectra shown in Figure 4.15. Since the resolution of the fluorescence maxima was not critical in these experiments, the exit slit was fixed at 1 mm.

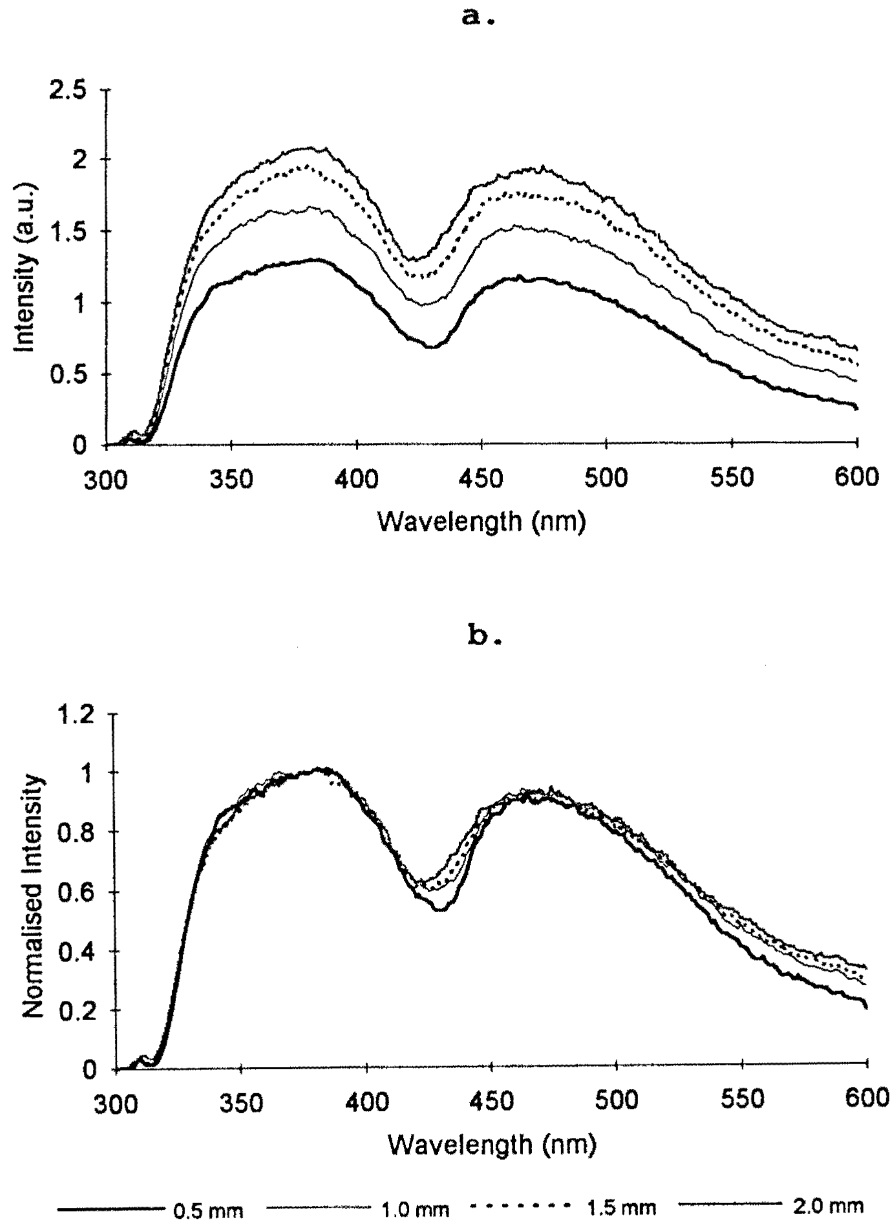

Figure 4.15 Effect of monochromator slit width. **a**: actual fluorescence measurements. **b**: spectral intensities normalised to intensity at $\lambda = 380$ nm

4.3 BASELINE MEASUREMENTS

4.3.1 Background radiation

Since the boxcar is gated to integrate the signal only during the fluorescence pulse, all sources of background radiation (such as room lights) would be excluded. This was verified by operating the laser with the beam shuttered and recording the fluorescence spectrum in the wavelength region 300 nm to 600 nm. The exponential moving average (10 samples) of the fluorescence intensity as a function of wavelength is shown in Fig. 4.16. Although the fluorescence spectrum displays a relatively high intensity at λ = 585 nm, this was not reproduced in further measurements. In comparison to the fluorescence intensity from a tissue sample (compare with scale of Y-axis in Figures 4.11 - 4.15), the background radiation contribution to the fluorescence spectrum is negligible. Consequently, the fluorescence measurements were not corrected for background radiation.

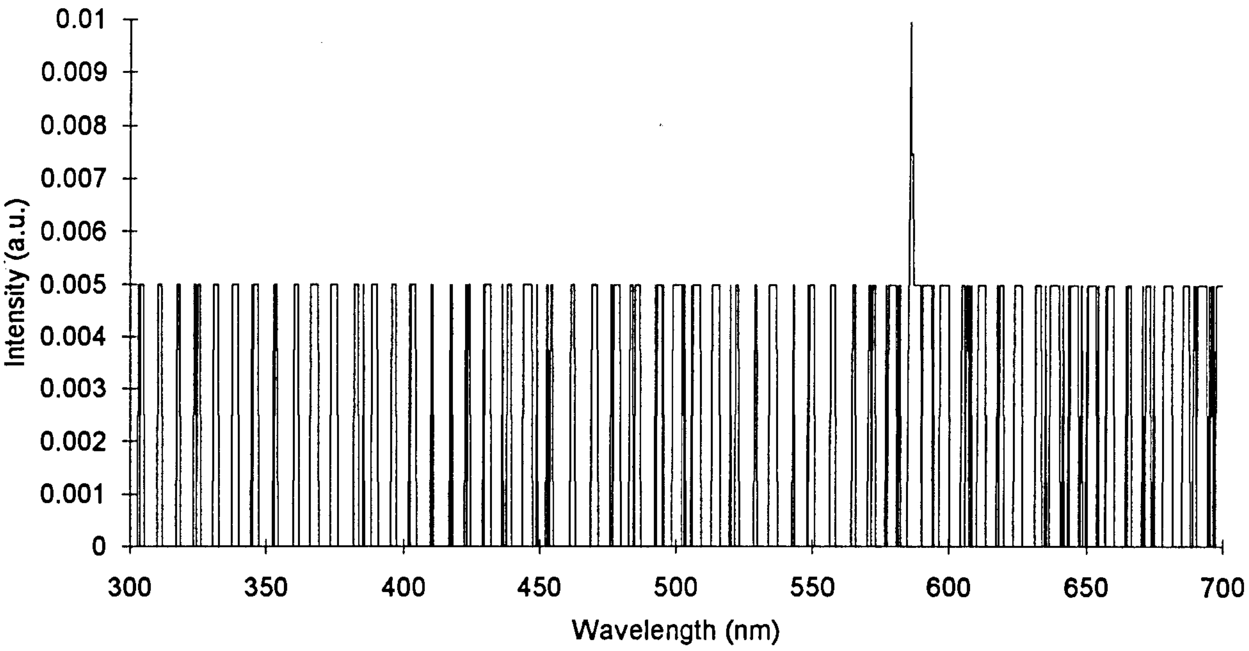

Figure 4.16 Background fluorescence

4.3.2 Fluorescence from sample as a function of exposure to laser radiation

a. Fixed wavelength

With the experimental method employed in this study, the fluorescence spectra are obtained by scanning the monochromator at a fixed rate, viz., 100 nm per minute. This means that the sample is exposed to 600 pulses per minute when the pulse repetition frequency of the laser is 10 Hz.

The variation of fluorescence intensity from a tissue sample as a result of exposure to the laser radiation was determined at two wavelengths, viz., $\lambda = 380$ nm and 460 nm. In this experiment the monochromator was set at a fixed wavelength and the sample was irradiated at the rate of 600 pulses per minute for 8 minutes. The fluorescence intensity as a function of time (i.e. with pulse rate 10 Hz) is shown in Figure 4.17 for $\lambda = 380$ nm. Also shown in Figure 4.17 is the exponential best fit curve to the data. Since there is no drift in the average laser output (see Figure 3.2), the best fit curves indicate that the fluorescence intensity decays exponentially with exposure to laser radiation and is represented by the following equation:

$$I = ae^{-bt} + c$$

where

I : fluorescence intensity, t : time in s and a, b, c are constants.

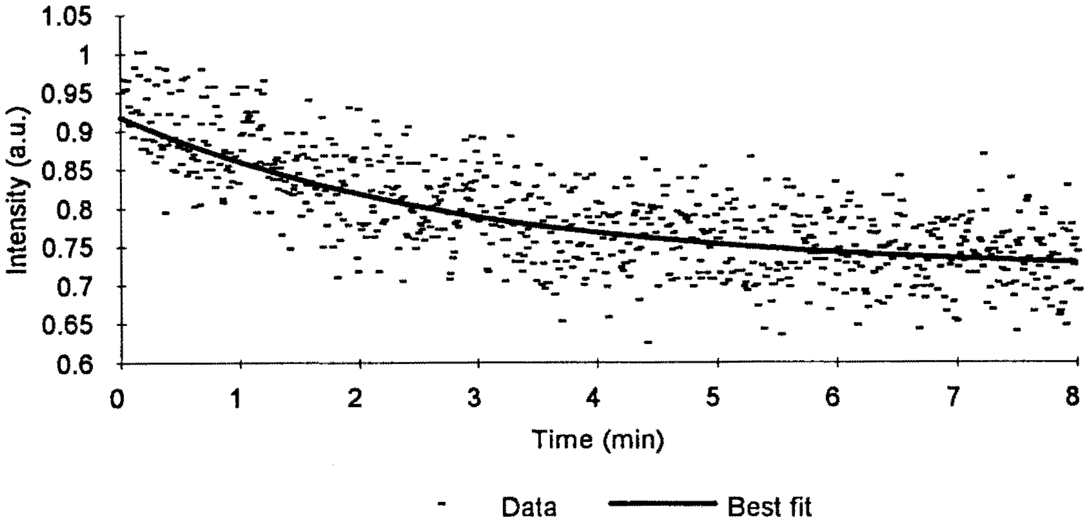

Figure 4.17 Variation of fluorescence intensity with time for $\lambda = 380$ nm

In the case of λ = 380 nm the values of the coefficients of the equation $I = ae^{-bt} + c$ are:

$a = 2.16 \times 10^{-1}$, $b = 5.98 \times 10^{-3}$, $c = 6.93 \times 10^{-1}$

In the case of λ = 460 nm the values of the coefficients of the equation $I = ae^{-bt} + c$ are:

$a = 1.82 \times 10^{-1}$, $b = 4.68 \times 10^{-3}$, $c = 4.94 \times 10^{-1}$

The best fit exponential decay curves for λ = 380 nm and λ = 460 nm when compared (see Figure 4.18) indicate that the fluorescence intensity decays at different rates for the two wavelengths. However, this difference in decay is noticeable for times > ≈3 min. Since a spectrum is acquired in 3 min., it may be assumed that the rate of decay of the fluorescence intensity are almost constant (within 1%) for λ = 380 nm and λ = 460 nm.

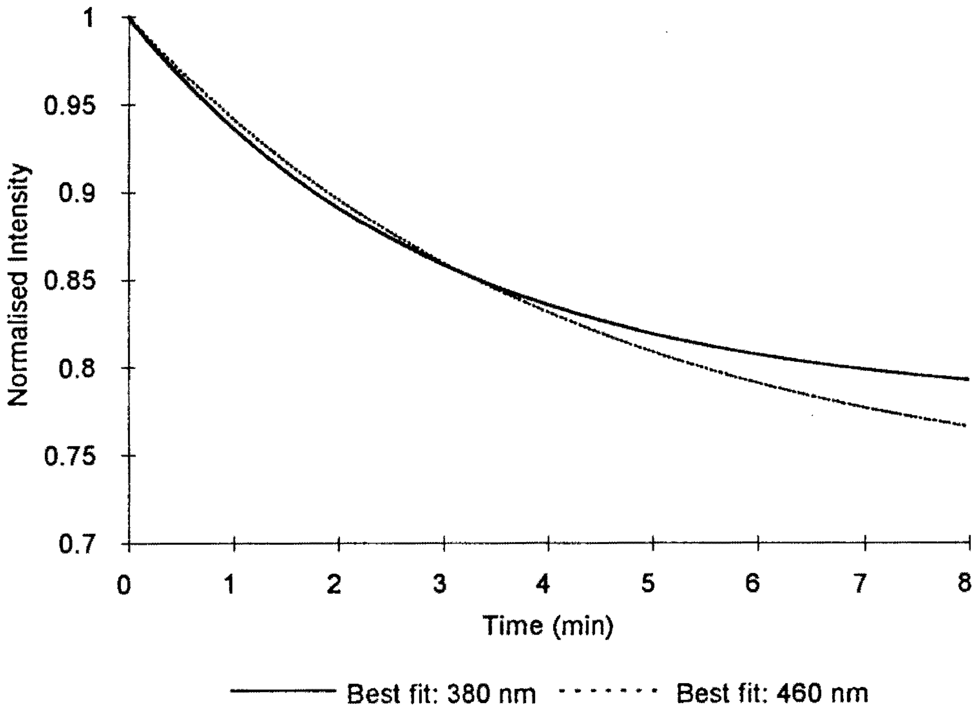

Figure 4.18 Comparison of decay of fluorescence intensities for λ = 380 nm and λ = 480 nm

b. Time dependence of fluorescence spectra

Five consecutive fluorescence scans (see Figure 4.19) were recorded from a tissue sample. In each scan the sample was exposed to 1200 laser pulses at the same spot on the sample. The time for each scan was 2 min. and the time between scans was approximately 1 min. Examination of the fluorescence spectra show that while there is a decrease in the fluorescence intensity with increasing exposure to the excitation radiation, the decrease is not uniform for all the wavelengths between λ = 320 nm and λ = 520 nm. The curves in Figure 4.19 are derived from successive groups of 1200 pulses, as indicated in the figure. However, the pulses providing the point with wavelength λ = 420 (say) are the 600th pulses of each group. Thus the relation between pulse number (N) and measured wavelength (λ) is $N = 6(\lambda - 320)$. A plot of the fluorescence spectral intensity at N pulses, N + 1200 pulses, .. , N + 4800 pulses is shown in Figure 4.20.

From Figure 4.20 it can be seen that there is a significant decrease in the fluorescence intensities in the wavelength range ≈ 360 nm to ≈ 390 nm. This means that significant photobleaching of the samples was occurring during the experiments. This is contrary to what has been reported in the literature by Pettit *et al* (1990). They report that repeated spectrum acquisition indicated that no significant photobleaching of the samples occurred during their experiments using a XeF laser.

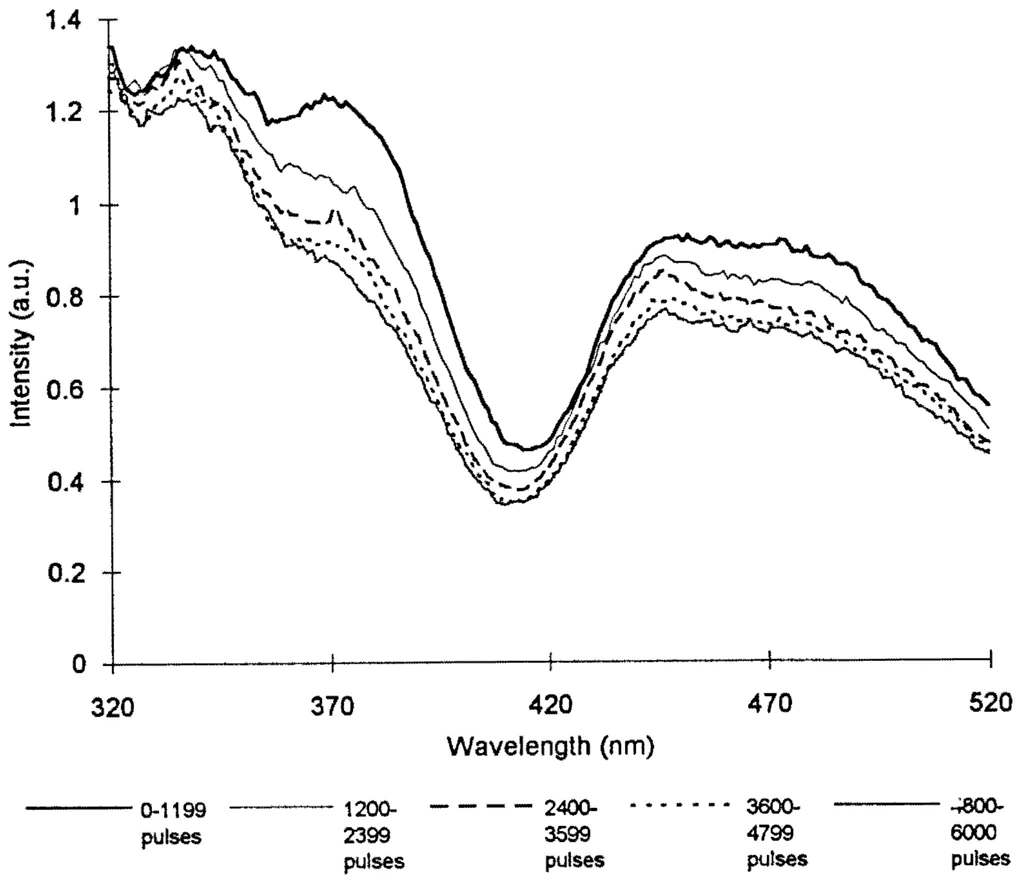

Figure 4.19 Successive fluorescence signals from tissue

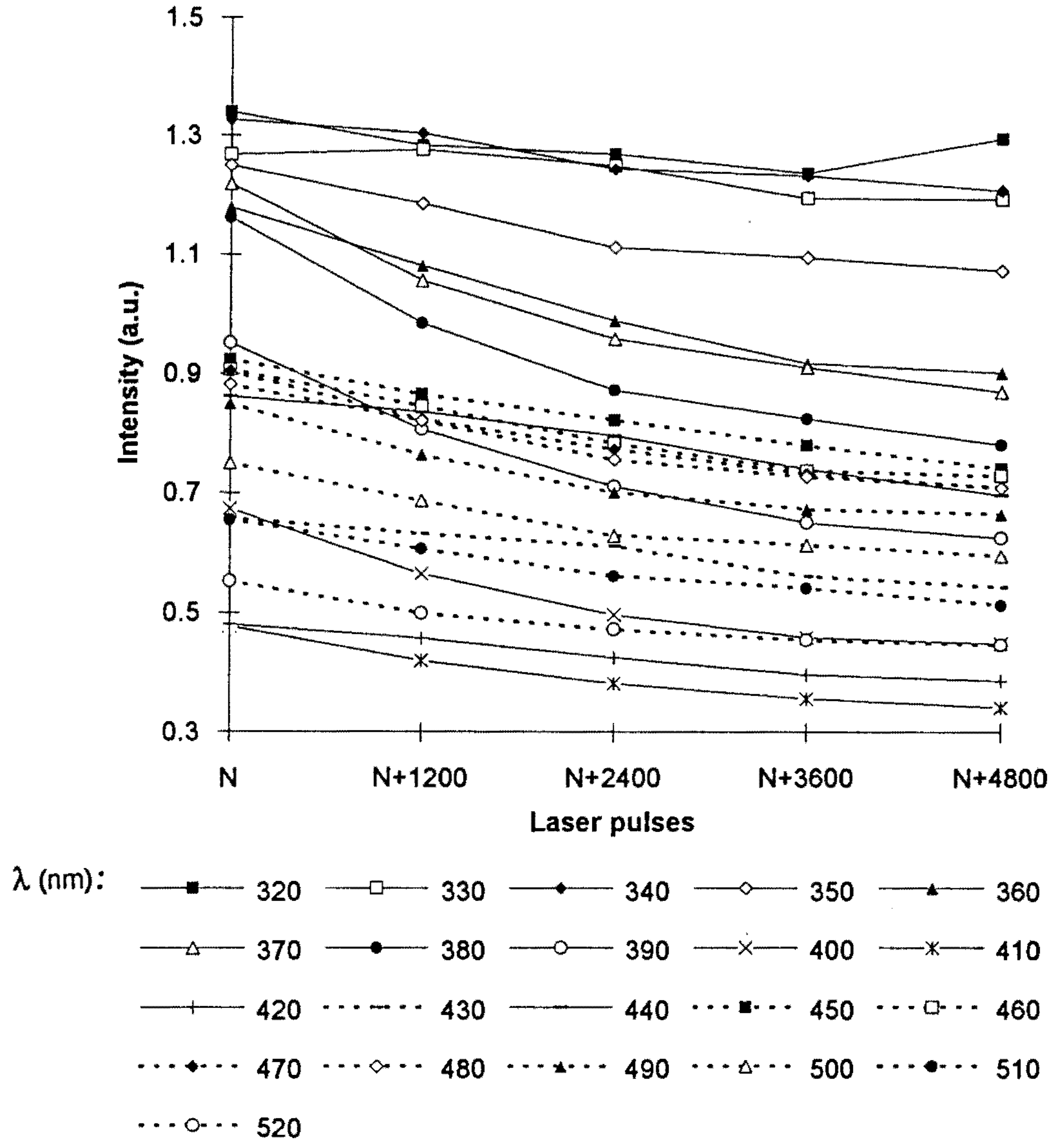

Figure 4.20 Change in fluorescence intensity as a function of exposure of tissue to laser pulses

4.4 FLUORESCENCE MEASUREMENTS

Representative fluorescence spectra for tissue samples classified as normal and Stary types II, III, V, VI, VIa, VIc, VII, VIII are shown in Figures 4.21 to 4.29 respectively. Combination of Stary types, viz., I-II, II-III, IIa-III, III-IV, VI-VII, VIc-VIII, VI-VIII and VII-VIII are shown in Figures 4.30 to 4.37, respectively. A representative fluorescence spectrum of a sample classified as arteriosclerotic tissue is shown in Figure 4.38.

A brief qualitative description of the fluorescence lineshapes corresponding to the different tissue types shown in Figures 4.21 to 4.38 is given in the captions of the Figures.

From Figures 4.21 to 4.38 and an analysis of the fluorescence spectra not shown here, it can be seen that there is a great deal of variability in the fluorescence signals from the different tissue types. However, the fluorescence signals display some general trends as described below.

The uniform lineshapes of all tissue types in the wavelength range $\lambda = 300$ nm to 335 nm, viz., a constant increase of fluorescence intensity towards longer wavelengths in this range, is a result of selective absorption of radiation by the filter placed in front of the entrance slit of the monochromator. Hence, this characteristic of the spectra must be considered as an artefact of the measurement system.

Another feature in all the spectra is the peak at $\lambda = 308$ nm. This is an artefact of the backscattered XeCl laser radiation.

The spectra may be described in two ways. It would appear that the spectra are characterised by two broad intensity maxima (peaks) located in the wavelength range $\lambda \cong$ 360 nm to $\cong$ 400 nm and $\lambda \cong$ 440 nm to $\cong$ 500 nm and intensity minima (dips or valleys) in the fluorescence lineshapes at $\lambda \cong$ 420 nm, $\cong$ 460 nm, $\cong$ 540 nm and $\cong$ 580 nm.

Another way of looking at the spectra is to say that the fluorescence lineshapes are characterised by a broadband fluorescence emission with the dips indicating the fluorescence reabsorption.

The dips observed at $\lambda \cong$ 420 nm, $\cong$ 540 nm and $\cong$ 580 nm may be attributed to the reabsorption of fluorescence by oxy-haemoglobin in the tissue. The absorption spectrum of blood shown in Figure 4.39 displays peaks at $\lambda = 418$ nm, 544 nm and 578 nm which are due to the Soret, α- and β bands of oxygenated haemoglobin, respectively (Furzikov *et al*, 1988).

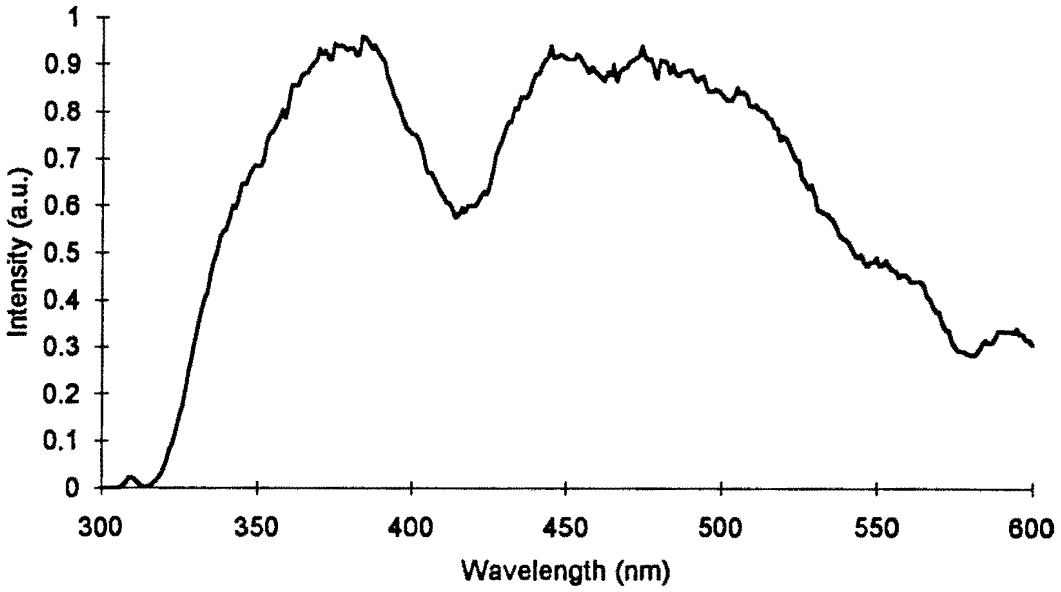

Figure 4.21 Fluorescence spectrum of a normal aorta (25 year old man). The fluorescence lineshape displays a peak at ≈ 380 nm and a plateau between ≈ 440 nm and ≈ 510 nm with a pronounced dip at ≈ 420 nm and slight dips at ≈ 540 nm and ≈ 580 nm.

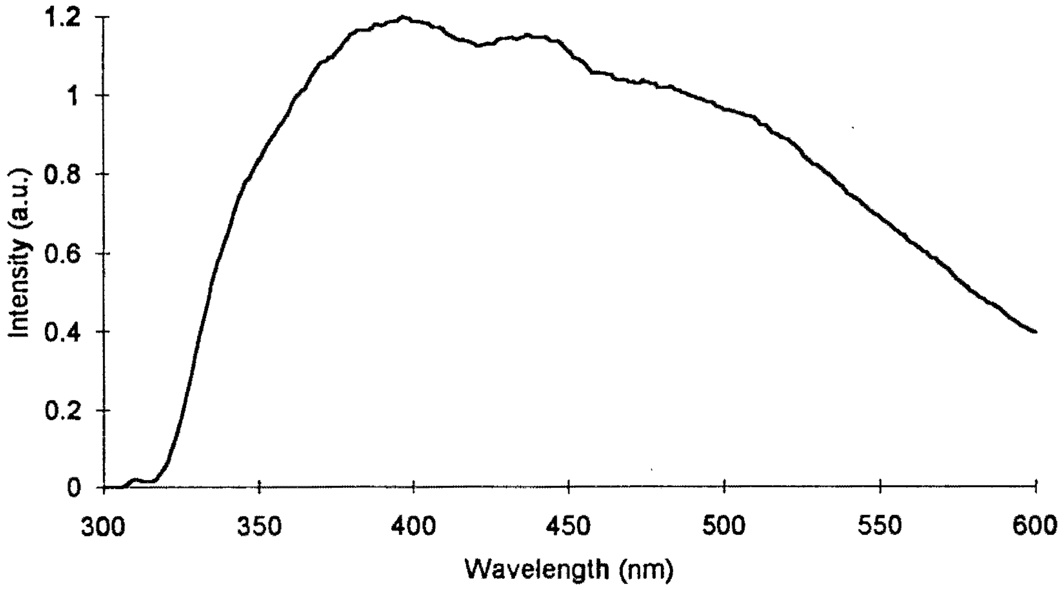

Figure 4.22 Fluorescence spectrum of a Stary type II aorta (31 year old man). The fluorescence lineshape displays a broad emission continuum between 300 nm to 600 nm with a maximum intensity at ≈ 390 nm. There is a slowly descending slope from ≈ 390 nm to ≈ 500 nm and then a steeper drop in intensity from ≈ 500 nm to 600 nm. There are fluorescence intensity dips at ≈ 420 nm and ≈ 460 nm.

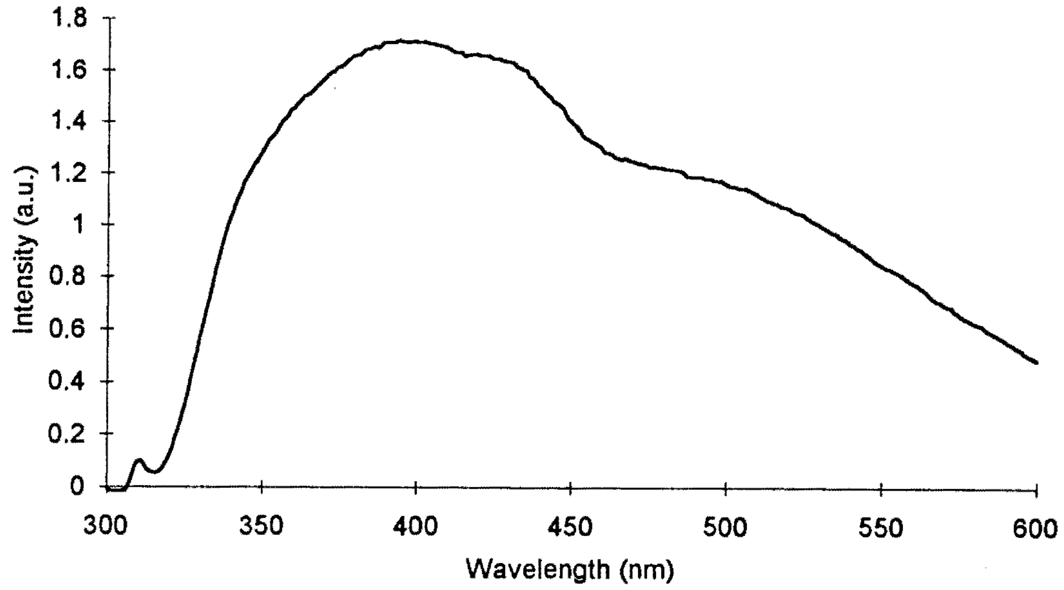

Figure 4.23 Fluorescence spectrum of a Stary type III aorta (31 year old man). The fluorescence lineshape displays a broad emission continuum between 300 and 600 nm. There is a slow decrease in intensity from ≈ 390 nm to ≈ 420 nm with a slight dip at ≈ 420 nm. There is a steeper decrease in intensity from ≈ 430 nm to 600 nm with a pronounced dip at ≈ 460 nm.

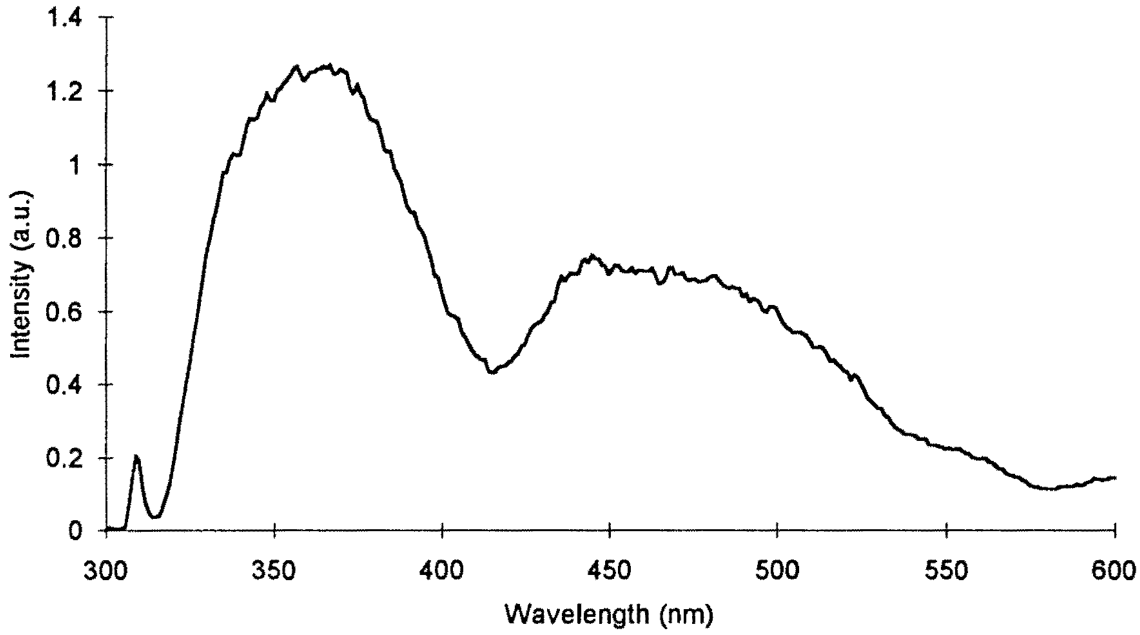

Figure 4.24 Fluorescence spectrum of a Stary type V iliac artery (28 year old woman). The fluorescence lineshape displays a symmetric peak at ≈ 370 nm with a steep decrease in intensity to ≈ 420 nm. The intensity increases to ≈ 440 nm from whence it gradually decreases to ≈ 480 nm and then undergoes a steeper decrease to ≈ 600 nm with dips at ≈ 535 nm and ≈ 580 nm.

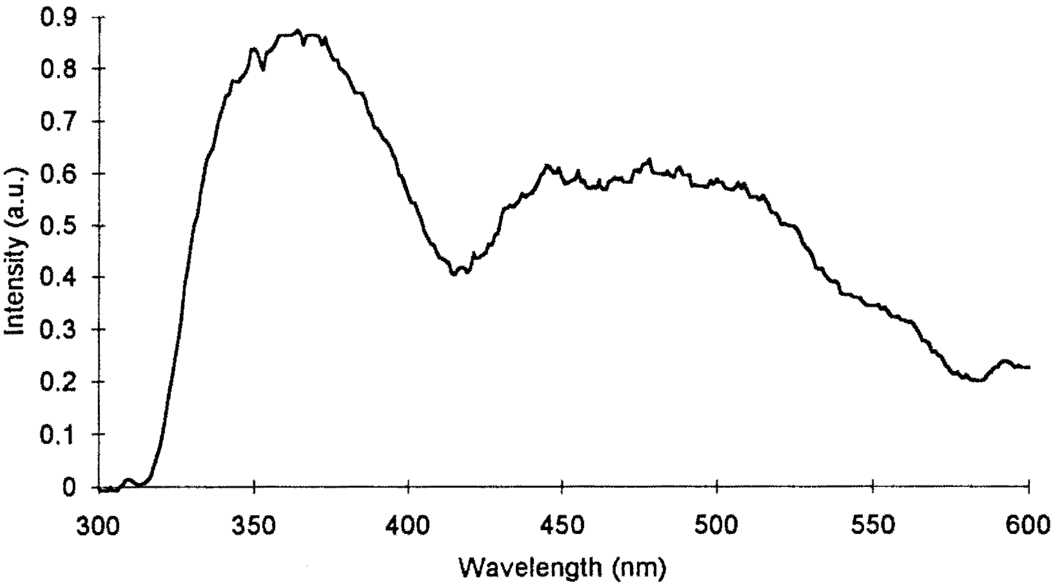

Figure 4.25 Fluorescence spectrum of a Stary type VI femorotibial artery (72 year old man). The fluorescence lineshape displays a peak at ≈ 365 nm and a pronounced dip at ≈ 420 nm. There is a plateau between ≈ 440 nm and 510 nm. The intensity then falls rapidly from ≈ 510 nm to 600 nm with dips at ≈ 530 nm and ≈ 580 nm.

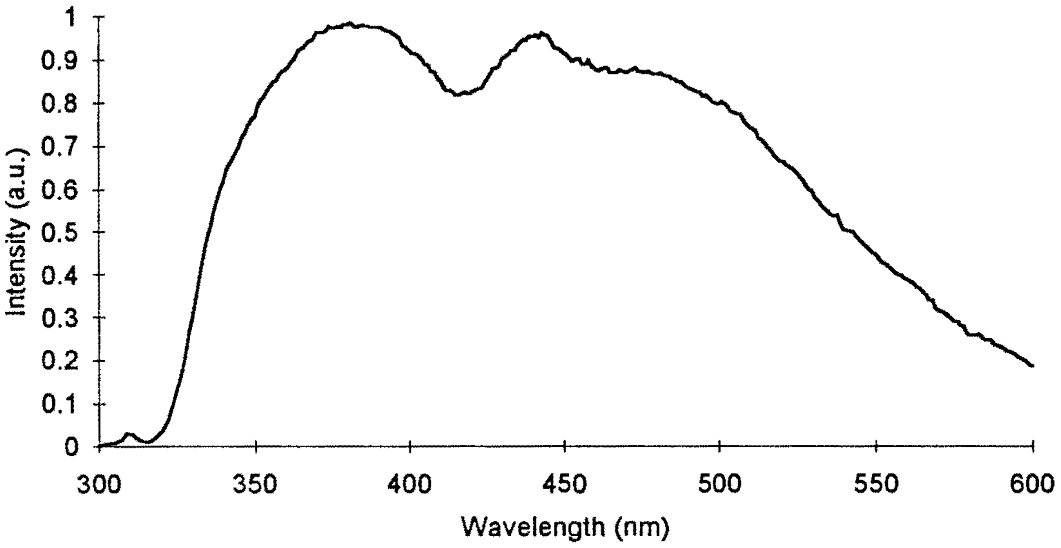

Figure 4.26 Fluorescence spectrum of a Stary type VIa femorotibial artery (55 year old woman). The fluorescence lineshape displays a plateau between ≈ 370 nm and ≈ 500 nm with a pronounced dip at ≈ 420 nm and a slight dip at ≈ 460 nm. The intensity drops off rapidly from ≈ 500 nm to 600 nm

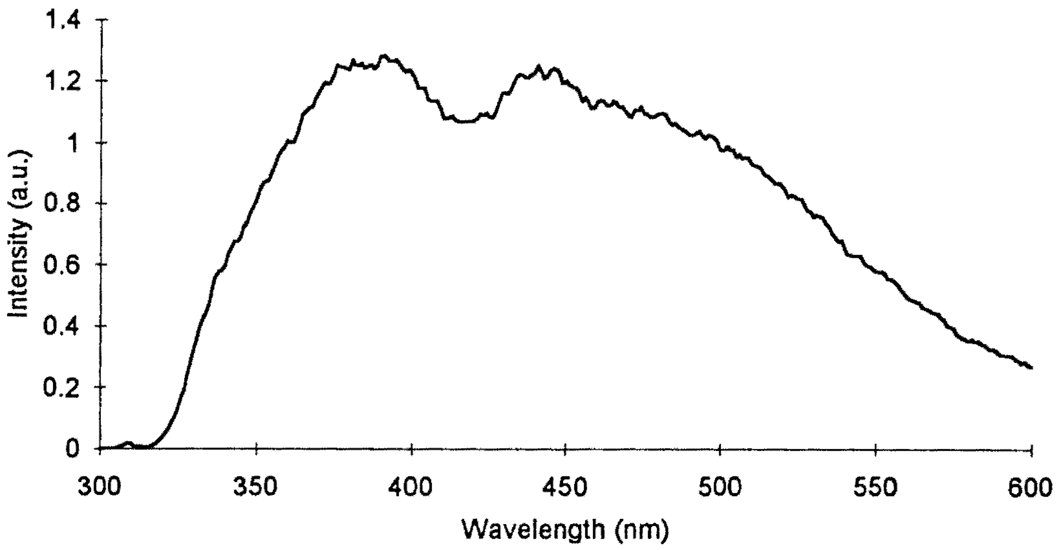

Figure 4.27 Fluorescence spectrum of a Stary type VIc aorta (44 year old man). The fluorescence displays a broad emission continuum between 300 nm and 600 nm with a pronounced dip at ≈ 420 nm and a slight dip at ≈ 460 nm.

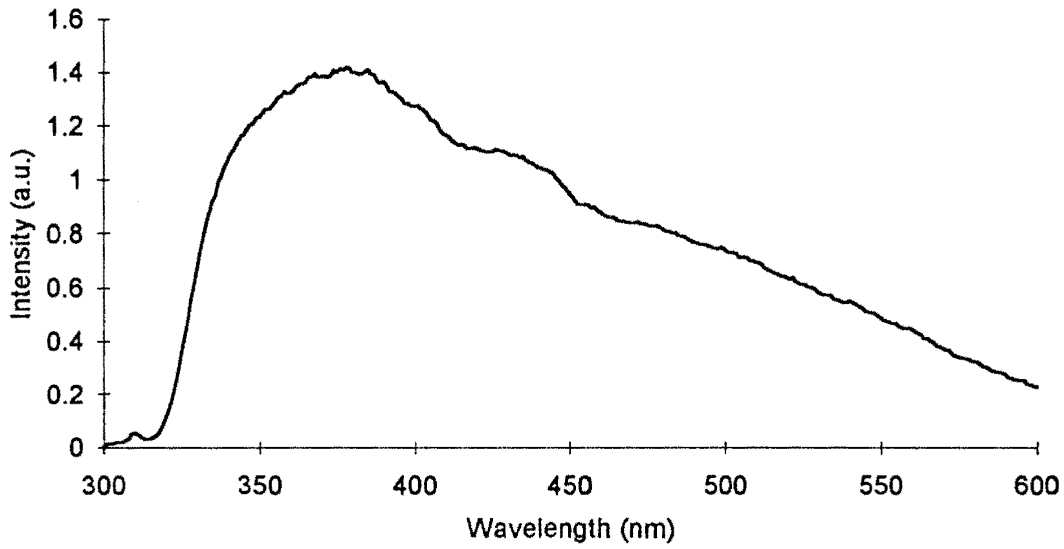

Figure 4.28 Fluorescence spectrum of a Stary type VII femorotibial artery (65 year old man). The fluorescence lineshape displays a "skewed distribution" with a uniform decrease in intensity for λ > 370 nm. Two dips at ≈ 420 nm and ≈ 460 nm can be seen on the decreasing limb of the curve.

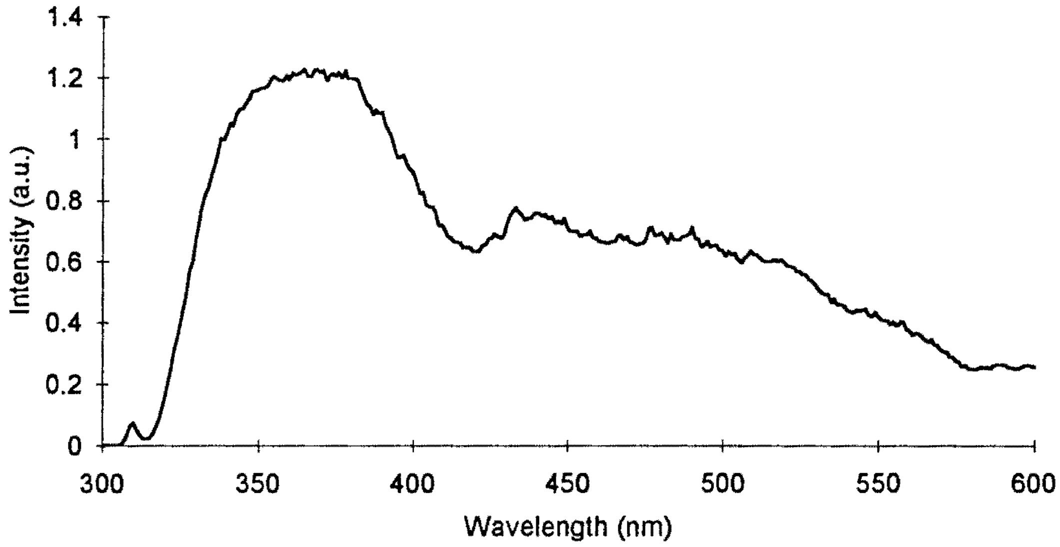

Figure 4.29 Fluorescence spectrum of a Stary type VIII femorotibial artery (78 year old woman). The fluorescence lineshape displays a broad peak between ≈ 350 nm and ≈ 380 nm and a pronounced dip at ≈ 420 nm. The curve between ≈ 460 nm and ≈ 520 nm shows a uniform and slight decrease in intensity. For λ > 520 nm there is a steeper decrease in intensity with dips at ≈ 540 nm and ≈ 580 nm.

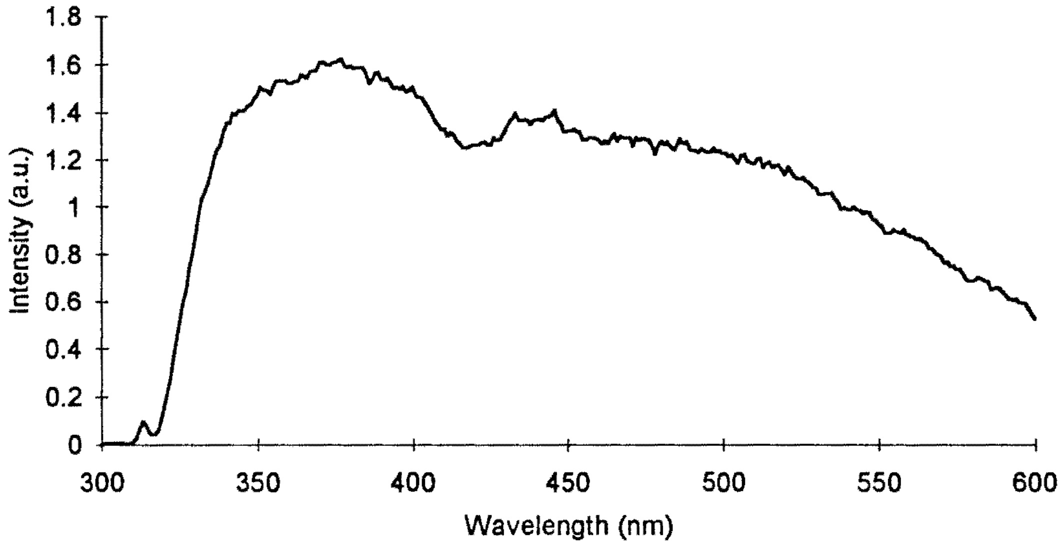

Figure 4.30 Fluorescence spectrum of a Stary type I-II aorta (35 year old man). The fluorescence lineshape displays a broad peak between ≈ 340 nm and ≈ 390 nm with a pronounced dip at ≈ 420 nm, a slight dip at ≈ 460 nm and a slight shoulder at ≈ 520 nm.

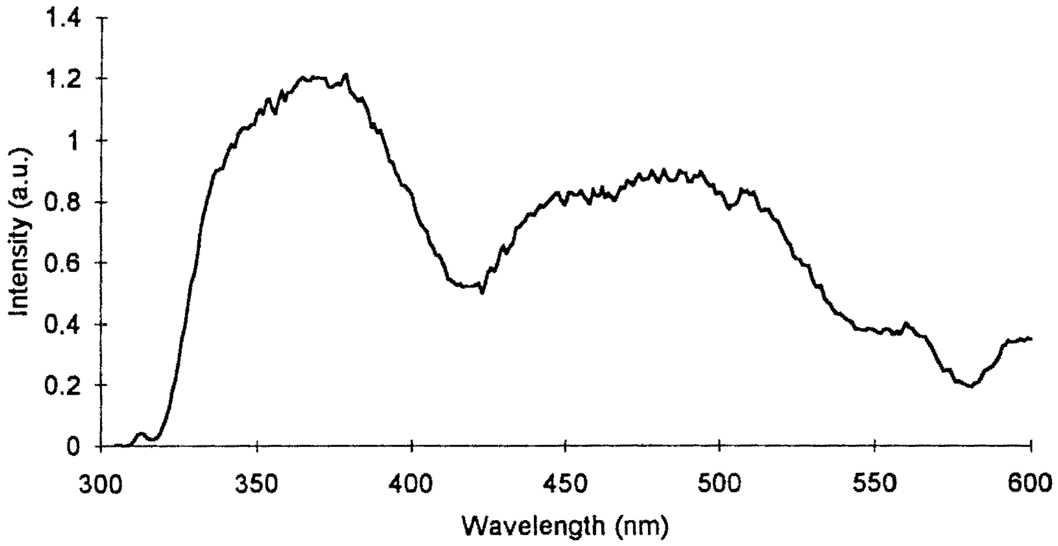

Figure 4.31 Fluorescence spectrum of a Stary type II-III iliac artery (35 year old man). The fluorescence lineshape displays a peak at ≈ 370 nm with a pronounced dip at ≈ 420 nm. There is a broad intensity maximum between ≈ 440 nm and ≈ 500 nm with a steep drop in intensity for λ > 500 nm. There are pronounced dips in the curve at ≈ 540 nm and ≈ 580 nm.

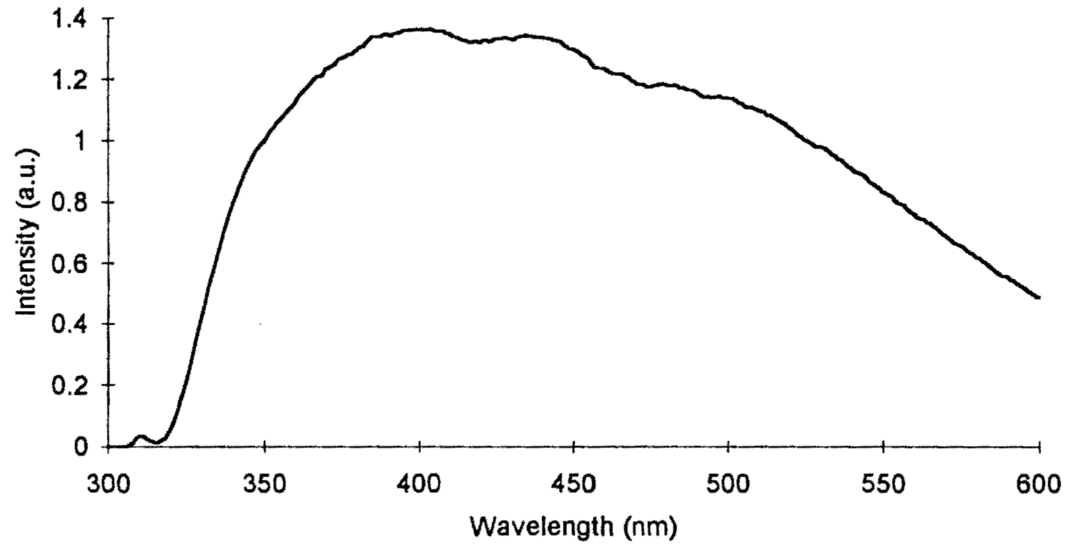

Figure 4.32 Fluorescence spectrum of a Stary type IIa-III aorta (30 year old man). The fluorescence lineshape displays a broad peak between λ = 315 nm to 600 nm with a maximum intensity at ≈ 390 nm. There is a slowly descending slope from ≈ 390 nm to ≈ 500 nm and then a steeper drop in intensity from ≈ 500 nm to 600 nm. There are intensity dips at ≈ 420 nm and ≈ 460 nm.

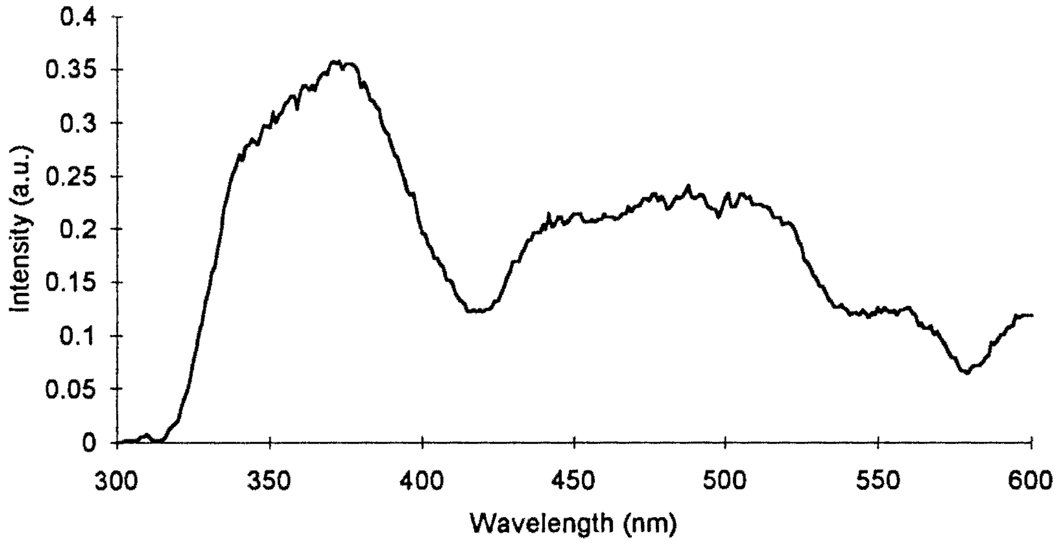

Figure 4.33 Fluorescence spectrum of a Stary type III-IV aorta (20 year old man). The fluorescence lineshape displays a peak at ≈ 370 nm with a pronounced dip at ≈ 420 nm. There is a flat intensity maximum between ≈ 440 nm and ≈ 500 nm with a steep drop in intensity for λ > 500 nm. There are pronounced dips in the curve at ≈ 540 nm and ≈ 580 nm.

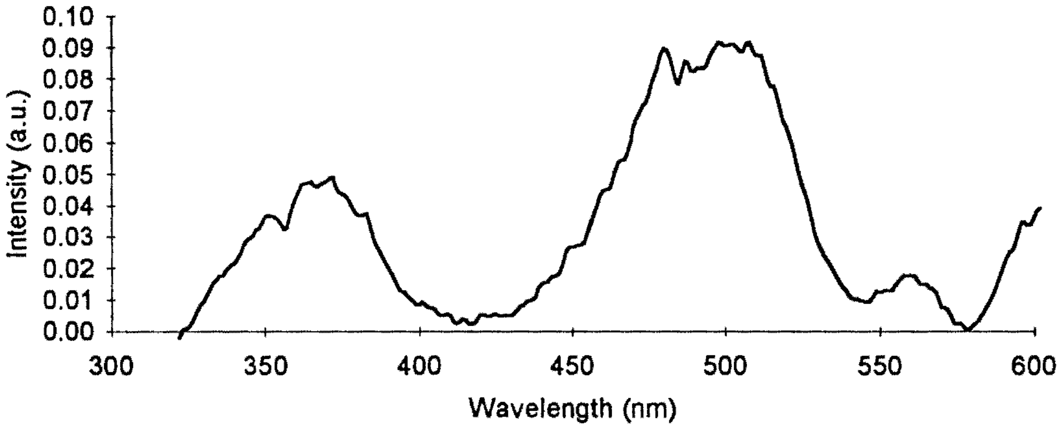

Figure 4.34 Fluorescence spectrum of a Stary type VI-VII femorotibial artery (65 year old man). The fluorescence lineshape displays two peaks at ≈ 370 nm and ≈ 500 nm with a pronounced dip at ≈ 420 nm and dips at ≈ 540 nm and ≈ 580 nm.

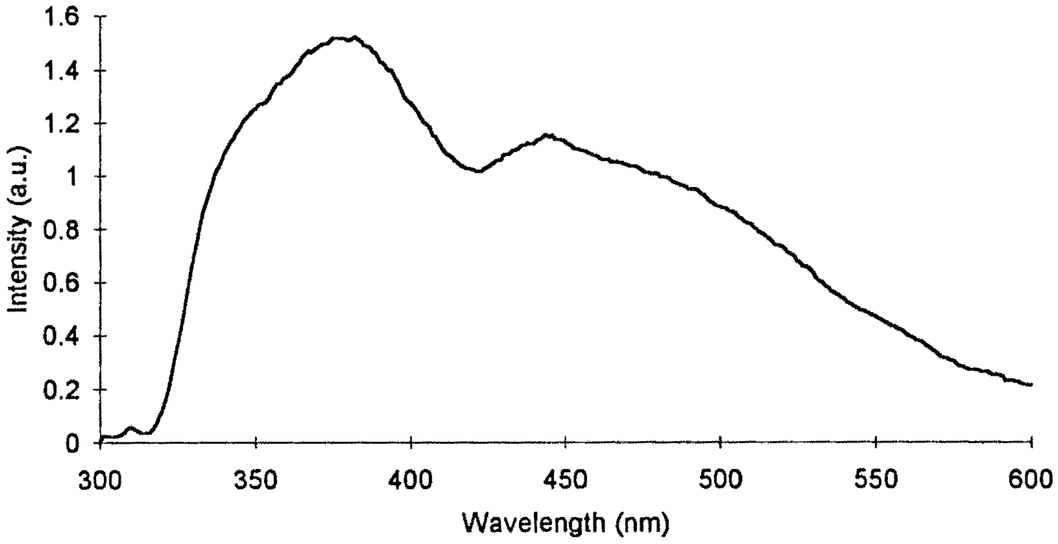

Figure 4.35 Fluorescence spectrum of a Stary type VI-VIII femorotibial artery (65 year old man). The fluorescence lineshape displays a peak at ≈ 380 nm with a pronounced dip at ≈ 420 nm and a slight dip at ≈ 460 nm on the decreasing limb of the lineshape.

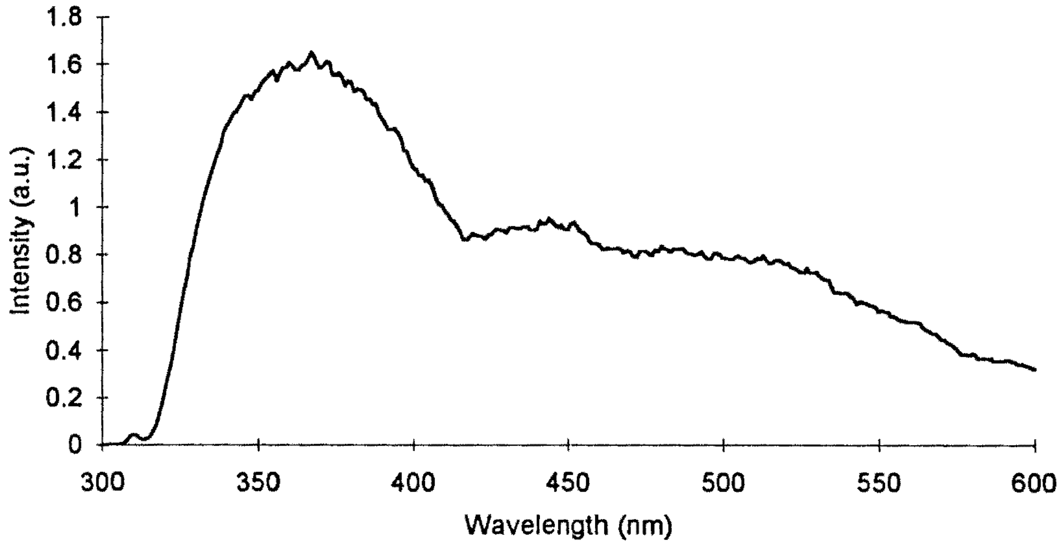

Figure 4.36 Fluorescence spectrum of a Stary type VIc-VIII femorotibial artery (78 year old woman). The fluorescence lineshape displays a peak at ≈ 360 nm and ≈ 380 nm and a dip at ≈ 420 nm. The curve between ≈ 420 nm and 600 nm shows a uniform and slight decrease in intensity with dips at ≈ 460 nm, ≈ 540 nm and ≈ 580 nm.

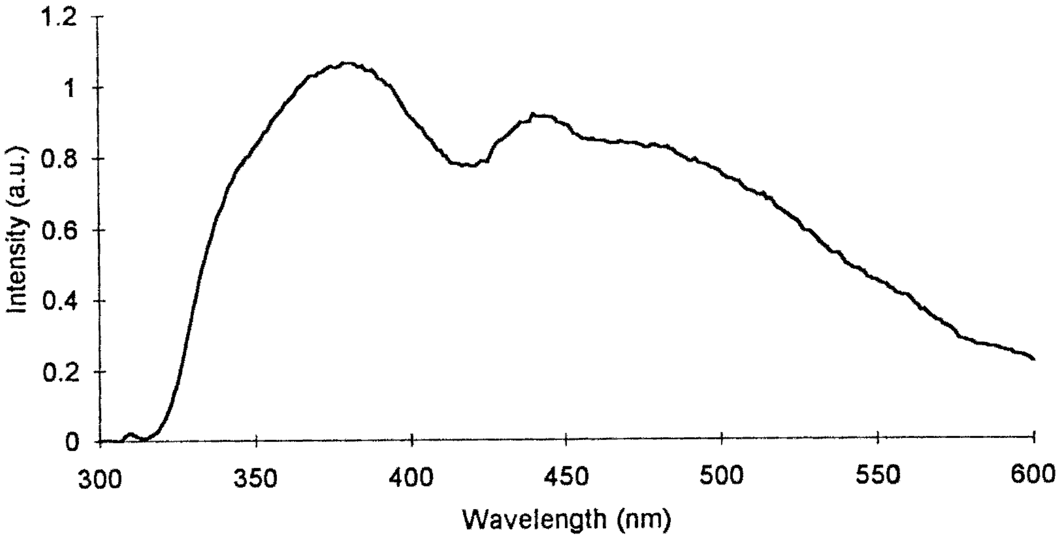

Figure 4.37 Fluorescence spectrum of a Stary type VII-VIII femorotibial artery (67 year old woman). The fluorescence lineshape displays a peak at ≈ 380 nm with a pronounced dip at ≈ 420 nm and a slight dip at ≈ 460 nm.

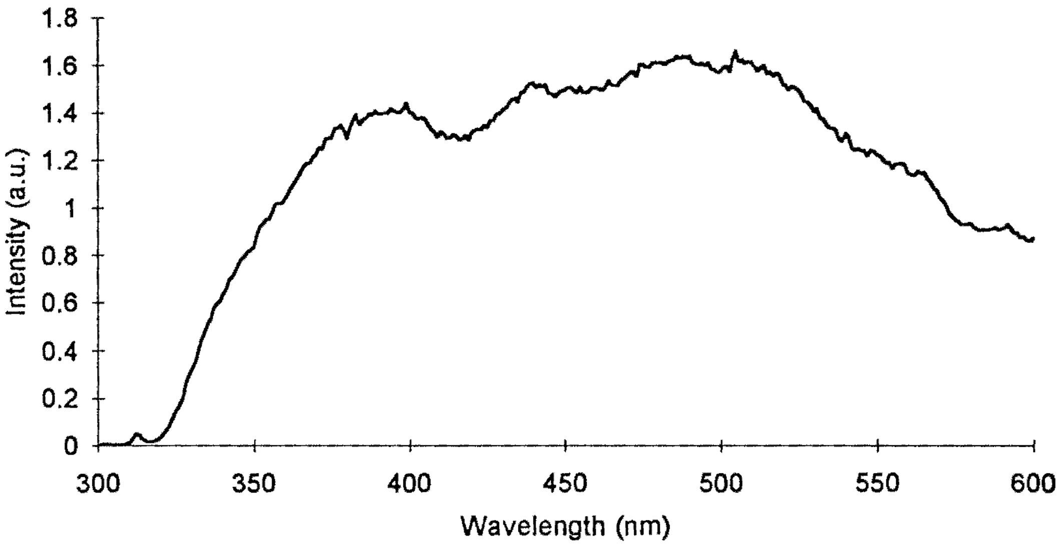

Figure 4.38 Fluorescence spectra of an femorotibial artery with arteriosclerosis (71 year old man). The fluorescence lineshape displays a broad emission continuum with dips at ≈ 420 nm, ≈ 460 nm, ≈ 540 nm and ≈ 580 nm. There are two intensity maxima at ≈ 400 nm and ≈ 510 nm.

The prominent oxy-haemoglobin dip at λ ≅ 420 nm in almost all the fluorescence spectra is present in varying degrees. In some cases, the dip is absent or not very well pronounced, e.g., representative spectrum of Stary type III tissue shown in Figure 4.23. A comparison of the ratio of the intensity of the peak at λ = 380 nm and the intensity of the dip at λ = 420 nm (see Figure 4.40) shows this variation. The ratio I(380 nm) : I(420 nm) for normal tissue and atherosclerotic tissue is 1.32 ± 0.51 and 1.88 ± 0.93, respectively. Here the ratio is expressed as mean ± standard deviation. Furthermore, the ratio I(380 nm) : I(420 nm) for normal tissue indicates that the reabsorption dip due to oxy-haemoglobin is not very pronounced. This result is not in agreement with the findings of Richards-Kortum *et al* (1989a).

Richards-Kortum *et al* (1989a) also indicate that cadaveric normal tissue has a higher average content of oxy-haemoglobin than atherosclerotic tissue. This is consistent with their observations that haemoglobin is taken up most readily in the intima of normal tissues, and less readily in the intima of atherosclerotic tissues.

In general, tissue samples obtained from cadavers will be exposed for varying periods of time to varying concentrations of free haemoglobin as red blood cells lyse. Thus, cadaveric tissues will contain varying amounts of oxy-haemoglobin.

The intensity maxima may be attributed to a number of fluorophores in arterial tissue. Three fluorophores, viz., collagen, elastin and tryptophan have been identified by Baraga *et al* (1990) as the primary source of fluorescence from the tissue. In brief

- tryptophan emission peaks between λ = 329 nm and 350 nm, depending on its local environment (see Figure 4.41a)
- collagen and elastin have emission peaks located very close to each other at λ = 383 nm and 379 nm respectively (see Figures 4.41b and 4.41c). These components can be spectroscopically separated due to the difference in their bandshapes: the emission bandshape of collagen (FWHM ≅ 40 nm) is significantly narrower than the elastin bandshape (FWHM ≅ 70 nm)
- emission at λ = 480 nm is largely due to elastin.

Table 4.3 contains the fluorescence emission characteristics of these fluorophores. It should be stated that the spectroscopic properties of many fluorophores are dependent on their local environment, changing for example as a function of concentration, pH or temperature (Lackowicz, 1983).

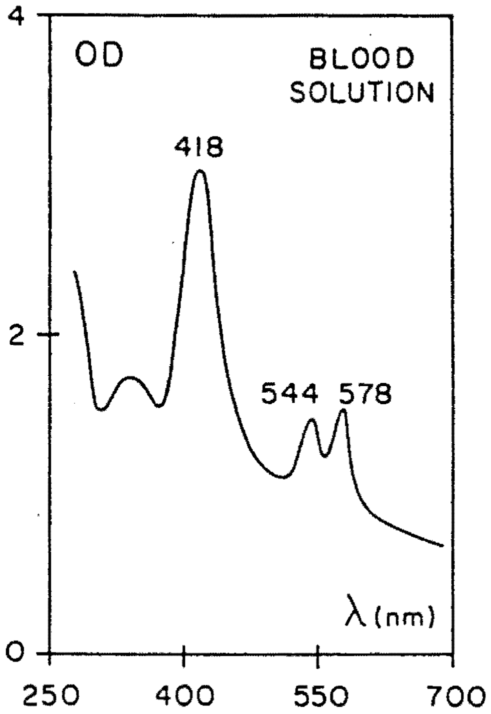

Figure 4.39 Absorption spectrum of human blood solution (from Furzikov *et al*, 1988)

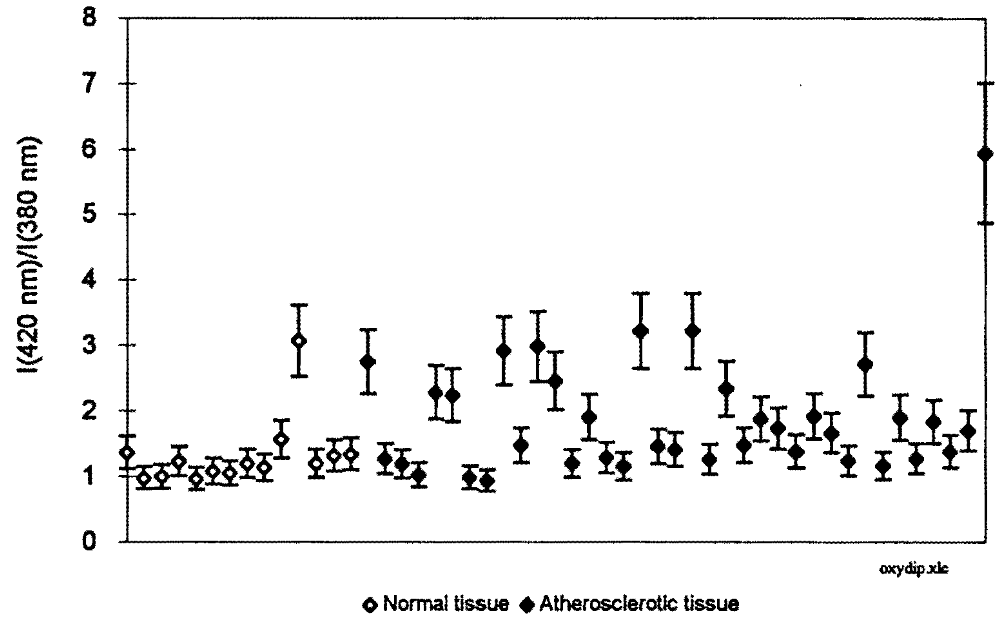

Figure 4.40 Ratio of fluorescence intensities at λ = 380 nm and λ = 420 nm for normal and atherosclerotic tissue

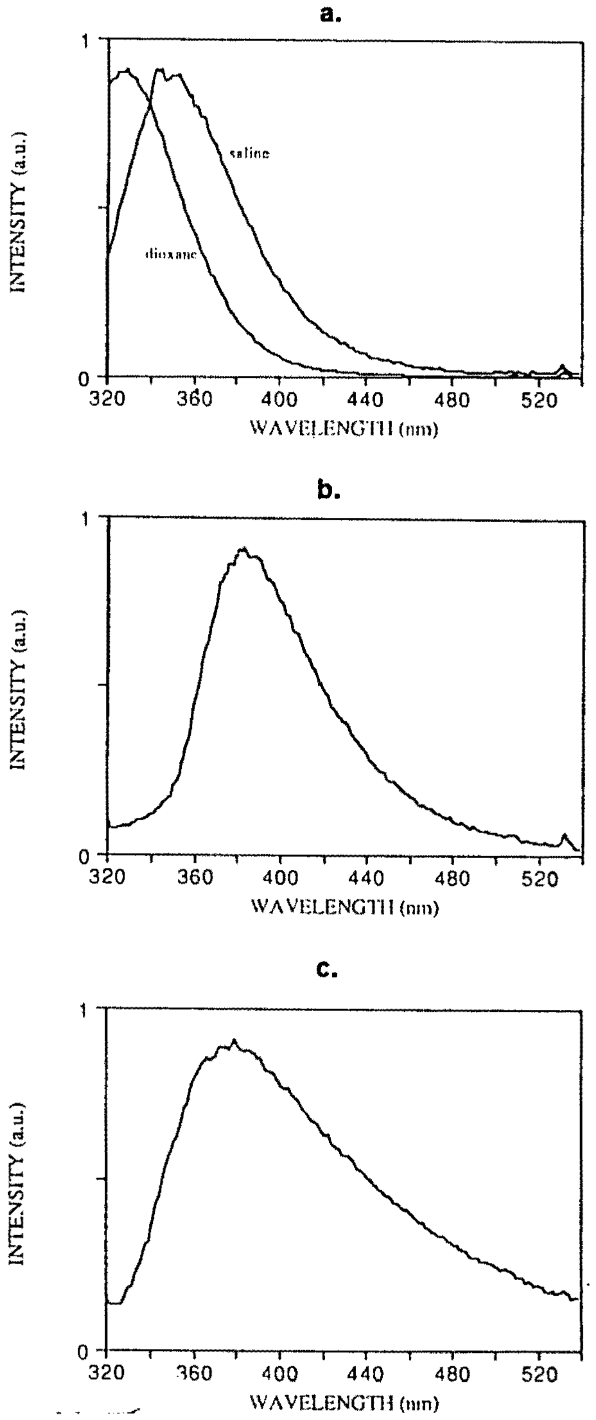

Figure 4.41 a. Laser induced fluorescence (LIF) emission spectra of L-tryptophan in dioxane (40 μM; $\lambda_x = 285$ nm) and saline solution (40 μM; pH = 7.4; $\lambda_x = 308$ nm). **b.** collagen type I, hydrated (Calbiochem, bovine Achilles tendon). c. Elastin, hydrated (Sigma, bovine neck ligament). (From Baraga *et al*, 1990)

Table 4.3 Laser induced fluorescence characteristics of tissue components (from Baraga *et al*, 1990)

Component	State	Peak wavelength (nm)	Full width at half maximum (nm)
Tryptophan	Aqueous	350	43
Tryptophan	1,4 dioxane	329	29
Collagen (type I)	Hydrated	383	40
Elastin	Hydrated	379	70

Richards-Kortum *et al* (1991) identified other potential fluorophores at $\lambda = 520$ nm, 535 nm and 595 nm due to pyridoxal 5'- phosphate and elastin. The excitation of these fluorophores is largely dependent on the wavelength of the impinging radiation.

For the fluorescence spectra obtained in this study, the peak at $\lambda \cong 380$ nm may be attributed to a combination of collagen and elastin and the peak at $\lambda \cong 480$ nm may be attributed to elastin.

The flat maxima or plateaus seen in a number of the fluorescence lineshapes (Figures 4.21 to 4.38) between $\lambda \cong 440$ nm and $\cong 520$ nm may be partially due to the fluorophores at $\lambda \cong 480$ nm and $\lambda \cong 520$ nm. The fluorophore at $\lambda \cong 535$ nm does not contribute to a noticeable peak, whereas the peak at $\lambda \cong 600$ nm in some of the spectra may be attributed to the fluorophore at $\lambda = 595$ nm.

More than one scan per sample was frequently performed to ensure that the fluorescence spectra were consistent. For each successive scan, there is reduction in the spectral intensities. The dependence of fluorescence spectral intensities on exposure of arterial tissue to XeCl laser radiation was shown in section 4.3.2. Based on the data obtained by examining the fluorescence spectra from 6 tissue samples (see Appendix G), there is in general, a reduction in fluorescence intensities of > 5% from one scan to the other. However, if the spectrum of each scan is normalised to the intensity at $\lambda = 380$ nm, then the normalised spectra are reproducible to 5%.

4.5 SPECTROSCOPIC IDENTIFICATION ALGORITHMS

One of the main aims of the thesis was the development of optimal spectroscopic criteria to distinguish between normal and atherosclerotic tissue.

A comparison of the absolute values of fluorescence intensities for the different tissue types as a basis for developing spectroscopic identification algorithms was not possible with the experimental method described in this thesis. The fluorescence emitted by the tissue is influenced by the various experimental parameters such as a. the random time variation in performing the experiments due to the availability of samples, b. changes in the experimental set-up mainly due to the XeCl laser facility being used for other purposes, and c. changes in beam intensity between experimental runs.

Other schemes were then explored to determine optimal diagnostic algorithms for the classification of tissue.

One way of evaluating the efficacy of the algorithm is to test its sensitivity, specificity and predictive value as defined below (Richards-Kortum *et al*, 1989b).

$$\text{Sensitivity} = \frac{no.of\ true\ positives}{total\ no.of\ atherosclerotic\ samples}$$

$$\text{Specificity} = \frac{no.of\ true\ negatives}{total\ no.of\ normal\ samples}$$

$$\text{Predictive value} = \frac{no.of\ true\ positives}{total\ no.of\ positives}$$

Here, positives refer to those samples diagnosed as being atherosclerotic tissue, ie., Stary types I to VIII. True positives denote positives actually displaying atherosclerosis, whereas, true negatives denote negatives which are actually normal.

In general, the sensitivity measures the ability of the algorithm to detect disease, while the specificity determines its ability to detect normal samples. A diagnostic algorithm to control laser ablation should maximise specificity in order to avoid perforation of the artery wall. Quantitative evaluation techniques (see below) were examined in order to determine which technique would provide the highest percentage of correctly diagnosed samples.

4.5.1 Quantitative evaluation of fluorescence spectra

Fourteen diagnostic algorithms (described below) were defined and applied to the fluorescence spectra obtained in this study. The algorithms combine 2, 3 or 4 fluorescence spectral intensities chosen at 10 nm wavelength intervals in the range 340 nm to 600 nm.

a. $R = I(\lambda_1)/I(\lambda_2)$

b. $S = [I(\lambda_1)]^{p_1} \times [I(\lambda_2)]^{p_2} \times [I(\lambda_3)]^{p_3}$

c. $T = [I(\lambda_1)]^{p_1} \times [I(\lambda_2)]^{p_2} \times [I(\lambda_3)]^{p_3} \times [I(\lambda_4)]^{p_4}$

d. $$U1 = \frac{I(\lambda_1)}{I(\lambda_2) + I(\lambda_3)}$$

$$U2 = \frac{I(\lambda_1)}{I(\lambda_2) - I(\lambda_3)}$$

e. $$V1 = \frac{I(\lambda_1) + I(\lambda_2)}{I(\lambda_3)}$$

$$V2 = \frac{I(\lambda_1) - I(\lambda_2)}{I(\lambda_3)}$$

f. $$W1 = \frac{I(\lambda_1) + I(\lambda_2)}{I(\lambda_3) + I(\lambda_4)}$$

$$W2 = \frac{I(\lambda_1) - I(\lambda_2)}{I(\lambda_3) + I(\lambda_4)}$$

$$W3 = \frac{I(\lambda_1) + I(\lambda_2)}{I(\lambda_3) - I(\lambda_4)}$$

$$W4 = \frac{I(\lambda_1) - I(\lambda_2)}{I(\lambda_3) - I(\lambda_4)}$$

g. $$X1 = \left(\frac{I(\lambda_1)}{I(\lambda_2)}\right)^{p_1} + \left(\frac{I(\lambda_3)}{I(\lambda_4)}\right)^{p_2}$$

$$X2 = \left(\frac{I(\lambda_1)}{I(\lambda_2)}\right)^{p_1} - \left(\frac{I(\lambda_3)}{I(\lambda_4)}\right)^{p_2}$$

where

$p_1, p_2, p_3, p_4 \in \{-2.00, -1.75, \ldots, 2\}$ and $p_1, p_2, p_3, p_4 \neq 0$

$\lambda_1, \lambda_2, \lambda_3, \lambda_4 \in$ {340 nm, 350 nm, .., 600 nm}

h. $$Y = \sum_{i}^{m} A_i / \sum_{j}^{n} A_j$$

where

$A_i = 0.5 \times 10 \times [I(10(i) + 330\text{ nm}) + I(10(i+1) + 330\text{ nm})]$

$A_j = 0.5 \times 10 \times [I(10(j) + 430\text{ nm}) + I(10(j+1) + 430\text{ nm})]$

$i = (\lambda_1 - 330)/10$

$m = (\lambda_2 - 340)/10$

$j = (\lambda_3 - 430)/10$

$n = (\lambda_4 - 440)/10$

$\lambda_1 \in$ {340 nm, 350 nm,..,390 nm}

$\lambda_2 \in$ {350 nm, 360 nm,..,400 nm}

$\lambda_3 \in$ {440 nm, 450 nm,.., 590 nm}

$\lambda_4 \in$ {450 nm, 460 nm,..,600 nm}

and

$\lambda_1 < \lambda_2$

The diagnostic algorithms were applied to the fluorescence spectra of the tissue samples that are classified in two ways, viz., (a) normal tissue and atherosclerotic tissue, and (b) non-fibrotic tissue and fibrotic tissue. The atherosclerotic tissue represents Stary type I to Stary type VIII. The non-fibrotic tissue represents the normal tissue as well as Stary type I to Stary type IV. The fibrotic tissue are the Stary type V to Stary type VIII.

For differentiating between normal and atherosclerotic tissue, the normal/atherosclerotic tissue classification is useful. For laser ablation it may be prudent to ablate advanced atherosclerotic tissue only, i.e., the fibrous tissue. Here the non-fibrotic/fibrotic classification would be useful.

In order to simulate the acquisition of all fluorescence spectral intensities from a single laser pulse, the fluorescence spectral intensities in each of the spectra were corrected for exposure to the laser radiation. The best fit decay curve for the fluorescence intensity at $\lambda = 380$ nm (see Figure 4.18) was used to correct the fluorescence intensities.

The sensitivity of each diagnostic algorithm was computed for specificities and predictive values set at 100%. In determining the sensitivity of each algorithm, a decision threshold, DT, was computed (O'Brien, 1989). DT is the maximum value of the algorithms for (a) the normal samples of the sample classification normal/atherosclerotic tissue, and (b) the non-fibrotic samples of the sample classification non-fibrotic/fibrotic tissue. In this way the specificity of each algorithm is maximised. The procedure for determining the uncertainties associated with algorithm scores are given in Appendix G.

Tables 4.5a and 4.5b contain the parameters that produced the highest sensitivities for each of the diagnostic algorithms described above for normal/atherosclerotic tissue and non-fibrotic/fibrotic tissue respectively.

Table 4.5a Parameters of algorithms with highest sensitivities for normal/atherosclerotic tissue classification

Algo-rithm	λ_1 (nm)	λ_2 nm)	λ_3 (nm)	λ_4 (nm)	p_1	p_2	p_3	p_4	DT	Sensi-tivity (%)
R	340	460							0.80 ± 0.14	62
	350	390							0.86 ± 0.10	62
S	410	400	480		-1.50	2.00	-0.50		1.26 ± 0.20	78
	410	400	480		-0.75	1.00	-0.25		1.12 ± 0.09	78
	540	370	550		-1.50	0.25	1.25		1.04 ± 0.07	78
	540	380	550		-1.50	0.25	1.25		1.05 ± 0.06	78
T	360	540	550	590	0.25	-1.75	1.75	-0.25	1.09 ± 0.09	81
	400	430	540	550	0.25	-0.25	-0.25	0.25	0.99 ± 0.03	81
	410	450	440	400	-1.00	-1.00	0.75	1.25	1.15 ± 0.10	81
	430	540	400	550	-1.00	-1.00	1.00	1.00	0.97 ± 0.10	81
U1	350	390	480						0.44 ± 0.05	68
	400	440	410						0.53 ± 0.03	68
U2	350	530	590						2.90 ± 0.24	62
V1	340	400	590						4.12 ± 0.62	51
V2	340	450	340						0.32 ± 0.02	19
W1	400	580	410	540					0.93 ± 0.05	73
W2	380	480	390	410					0.13 ± 0.02	65
W3	340	370	530	590					5.97 ± 0.54	65
W4	390	500	410	550					0.71 ± 0.05	78
X1	550	430	400	540	1.00	0.50			1.87 ± 0.08	84
X2	360	590	540	550	0.25	1.75			0.10 ± 0.07	81
	550	540	590	360	1.50	0.25			0.09 ± 0.08	81
Y	340	350	450	460					0.87 ± 0.12	62
	340	370	440	480					0.78 ± 0.08	62
	340	370	450	470					1.55 ± 0.16	62
	340	380	450	470					2.18 ± 0.19	62
	340	400	440	470					2.23 ± 0.16	62
	340	400	460	560					0.83 ± 0.06	62

Table 4.5b Parameters of algorithms with the highest sensitivities for the non-fibrotic/fibrotic tissue classification

Algorithm*	λ_1 (nm)	λ_2 (nm)	λ_3 (nm)	λ_4 (nm)	p_1	p_2	p_3	p_4	DT	Sensitivity (%)
R'	400	560							2.19 ± 0.22	63
S'	490	550	570		-0.25	2.00	-1.75		1.39 ± 0.09	74
	500	550	570		-0.25	1.75	-1.50		1.32 ± 0.07	74
	500	550	570		-0.25	2.00	-1.75		1.40 ± 0.09	74
	510	550	570		-0.25	1.75	-1.50		1.33 ± 0.08	74
	510	550	570		-0.25	2.00	-1.75		1.42 ± 0.09	74
	520	550	570		-0.25	1.50	-1.25		1.27 ± 0.06	74
	520	550	570		-0.25	1.75	-1.50		1.36 ± 0.08	74
	560	550	570		-0.75	2.00	-1.25		1.51 ± 0.12	74
	560	550	570		-0.50	1.50	-1.00		1.38 ± 0.08	74
	560	550	570		-0.25	0.75	-0.50		1.18 ± 0.03	74
T'	490	470	550	570	-0.75	0.50	2.00	-1.75	1.39 ± 0.09	74
	490	480	550	570	-1.00	0.75	2.00	-1.75	1.41 ± 0.10	74
	500	490	550	570	-1.00	0.75	2.00	-1.75	1.45 ± 0.09	74
	500	490	550	570	-0.75	0.50	2.00	-1.75	1.43 ± 0.09	74
	520	530	550	570	-0.75	0.75	1.75	-1.75	1.45 ± 0.09	74
	550	570	550	560	-1.00	-0.50	1.75	-0.25	1.18 ± 0.03	74
	560	550	550	570	-1.00	0.75	2.00	-1.75	1.77 ± 0.27	74
	560	550	550	570	-1.00	1.00	2.00	-2.00	1.91 ± 0.32	74
	560	550	550	570	-0.75	0.25	2.00	-1.50	1.63 ± 0.02	74
	560	570	550	560	-1.00	-1.00	1.50	0.50	1.38 ± 0.08	74
	570	460	550	440	-1.00	-0.25	1.00	0.25	1.32 ± 0.06	74
	570	490	550	530	-1.00	-0.25	1.00	0.25	1.21 ± 0.40	74
	570	500	550	530	-1.00	-0.25	1.00	0.25	1.22 ± 0.04	74
	570	510	550	520	-1.00	0.25	1.25	-0.50	1.21 ± 0.06	74
	570	520	550	570	-1.00	-0.25	1.50	-0.25	1.27 ± 0.06	74
	570	530	550	560	-1.00	-0.25	1.50	-0.25	1.26 ± 0.07	74
	570	560	550	570	-1.00	-0.75	2.00	-0.25	1.51 ± 0.12	74
	570	560	550	540	-1.00	-0.50	1.75	-0.25	1.34 ± 0.10	74
	570	570	550	490	-1.00	-0.75	2.00	-0.25	1.39 ± 0.09	74
	570	570	550	500	-1.00	-0.75	2.00	-0.25	1.40 ± 0.09	74
	570	570	550	510	-1.00	-0.75	2.00	-0.25	1.42 ± 0.09	74
	570	570	550	500	-1.00	-0.50	1.75	-0.25	1.32 ± 0.07	74
	570	570	550	510	-1.00	-0.50	1.75	-0.25	1.33 ± 0.08	74
	570	570	550	520	-1.00	-0.50	1.75	-0.25	1.36 ± 0.08	74

Table 4.5b (continued)

Algorithm*	λ_1 (nm)	λ_2 (nm)	λ_3 (nm)	λ_4 (nm)	p_1	p_2	p_3	p_4	DT	Sensitivity (%)
U1'	390	510	590						1.01 ± 0.05	63
	390	510	600						1.06 ± 0.06	63
	390	520	600						1.09 ± 0.04	63
	400	400	560						0.69 ± 0.03	63
	400	540	560						1.00 ± 0.08	63
	400	540	590						1.16 ± 0.07	63
	400	540	600						1.20 ± 0.10	63
	400	550	560						1.05 ± 0.08	63
	400	550	600						1.27 ± 0.09	63
	400	560	560						1.09 ± 0.12	63
	400	560	570						1.20 ± 0.10	63
	400	560	590						1.30 ± 0.08	63
	400	560	600						1.34 ± 0.15	63
	400	570	600						1.45 ± 0.14	63
	400	590	550						1.25 ± 0.07	63
	400	590	600						1.63 ± 0.14	63
	410	420	600						0.78 ± 0.08	63
U2'	370	580	600						21.15 ± 74.02	33
	390	540	580						5.62 ± 0.52	33
	390	580	600						22.90 ± 77.63	33
V1'	340	390	600						4.80 ± 0.56	63
	350	390	600						4.97 ± 0.54	63
	360	390	600						5.12 ± 0.49	63
	370	390	600						5.24 ± 0.43	63
	400	360	600						4.88 ± 0.44	63
	400	370	600						5.34 ± 0.49	63
	400	380	600						5.41 ± 0.42	63
	410	370	600						5.19 ± 0.44	63
	410	380	600						5.26 ± 0.38	63
	420	370	600						5.10 ± 0.50	63
	420	380	600						5.17 ± 0.44	63
	430	370	600						5.26 ± 0.45	63
	430	380	600						5.33 ± 0.40	63
	440	370	600						5.44 ± 0.43	63
	530	390	600						4.67 ± 0.28	63
	540	390	600						4.56 ± 0.29	63
	550	390	600						4.50 ± 0.32	63
	560	390	600						4.50 ± 0.28	63
	570	390	600						4.42 ± 0.27	63
	580	390	600						4.35 ± 0.31	63
	590	390	600						4.40 ± 0.30	63
	590	400	590						3.59 ± 0.27	63
V2'	490	410	600						0.08 ± 0.03	07

Table 4.5b (continued)

Algorithm*	λ_1 (nm)	λ_2 (nm)	λ_3 (nm)	λ_4 (nm)	p_1	p_2	p_3	p_4	DT	Sensitivity (%)
W1'	520	550	520	570					1.10 ± 0.01	74
W2'	550	570	520	540					0.09 ± 0.01	74
	550	570	520	550					0.09 ± 0.01	74
	550	570	520	570					0.10 ± 0.01	74
	550	570	530	560					0.11 ± 0.01	74
W3'	370	370	580	600					42.30 ± 148.0	33
W4'	380	450	570	580					4.23 ± 1.40	63
X1'	380	390	420	590	1.00	0.25			2.30 ± 0.06	74
	550	570	440	460	0.75	0.25			2.23 ± 0.04	74
	550	570	530	490	0.75	0.25			2.15 ± 0.03	74
	550	570	530	500	0.75	0.25			2.16 ± 0.03	74
	550	570	540	510	1.00	0.25			2.23 ± 0.05	74
	550	570	550	510	1.00	0.25			2.20 ± 0.05	74
	550	570	570	520	1.00	0.25			2.16 ± 0.04	74
	590	400	400	590	0.50	0.25			1.90 ± 0.01	74
X2'	530	510	570	550	0.25	1.00			0.18 ± 0.02	78
Y'	340	400	590	600					25.37 ± 3.08	48

* The algorithms to distinguish between non-fibrotic and fibrotic tissue are denoted with a prime notation.

Analysis of the optimal sensitivities obtained for the diagnostic algorithms indicate that the sensitivities are greater for the tissue classification normal/atherosclerotic than the tissue classification non-fibrotic/fibrotic. The algorithm score:

$$X1_A = \left(\frac{I(550\,nm)}{I(430\,nm)}\right) + \left(\frac{I(400\,nm)}{I(540\,nm)}\right)^{0.5}$$

produced the highest sensitivity to distinguish between normal and atherosclerotic tissue, viz., 84%, i.e., 14 out of 14 normal samples (100%) and 31 out of 37 atherosclerotic samples (84%) were correctly identified.

The algorithm score:

$$X2'_A = \left(\frac{I(530\,\text{nm})}{I(510\,\text{nm})}\right)^{0.25} - \left(\frac{I(570\,\text{nm})}{I(550\,\text{nm})}\right)$$

produced the highest sensitivity to distinguish between non-fibrotic and fibrotic tissue, viz., 78%, i.e., 24 out of 24 non-fibrotic samples and 21 out of 27 fibrotic samples were correctly identified.

The results also show that the algorithms containing a combination of four spectral fluorescence intensities produced the higher sensitivities.

Scatter plots for the algorithm scores $X1_A$ and $X2'_A$ are given in Figure 4.42 and Figure 4.43, respectively.

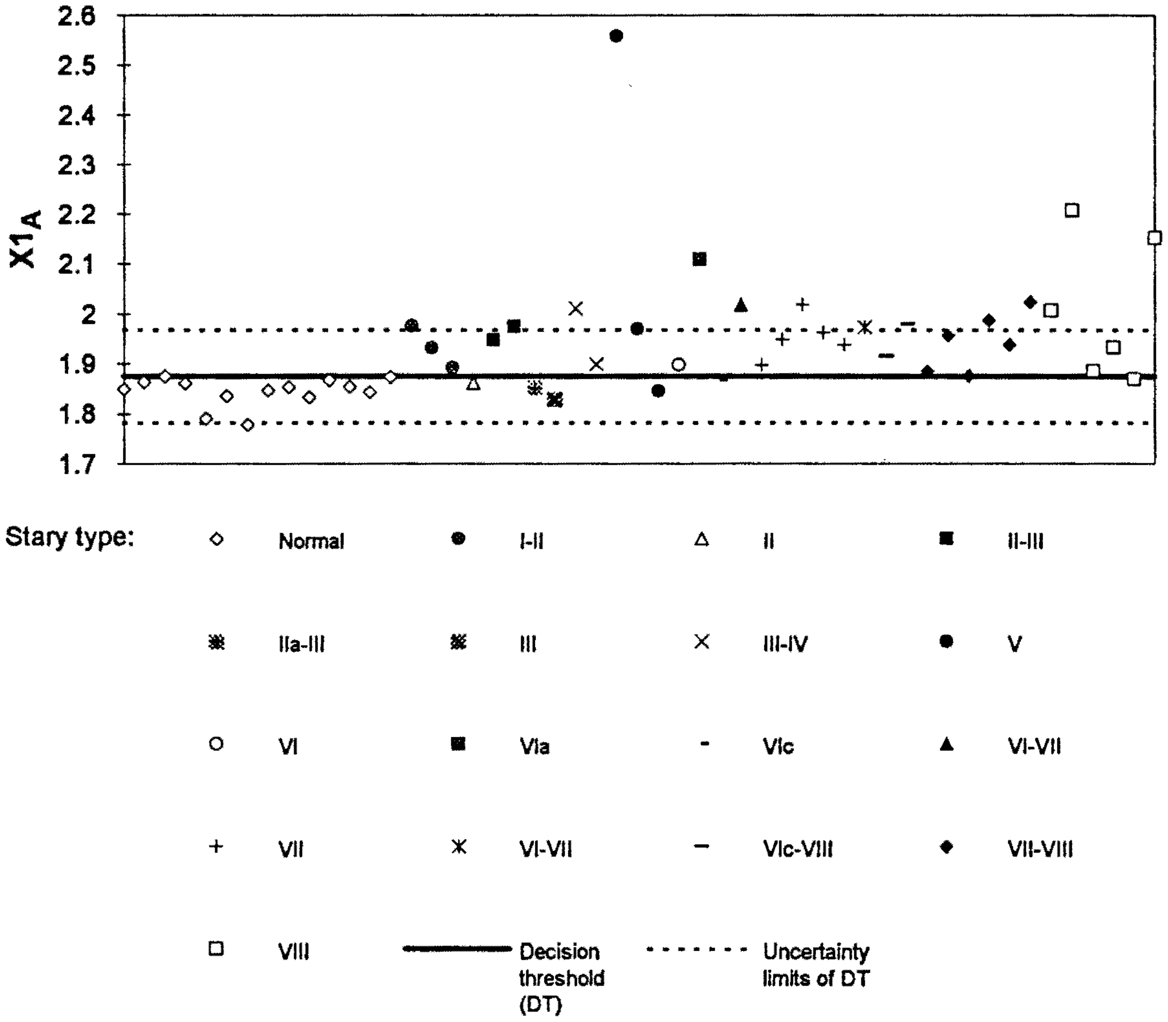

Figure 4.42 Scatter plot for the algorithm score $X1_A = \left(\frac{I(550\,\text{nm})}{I(430\,\text{nm})}\right) + \left(\frac{I(400\,\text{nm})}{I(540\,\text{nm})}\right)^{0.5}$.

Uncertainty of individual data points: ± 5%

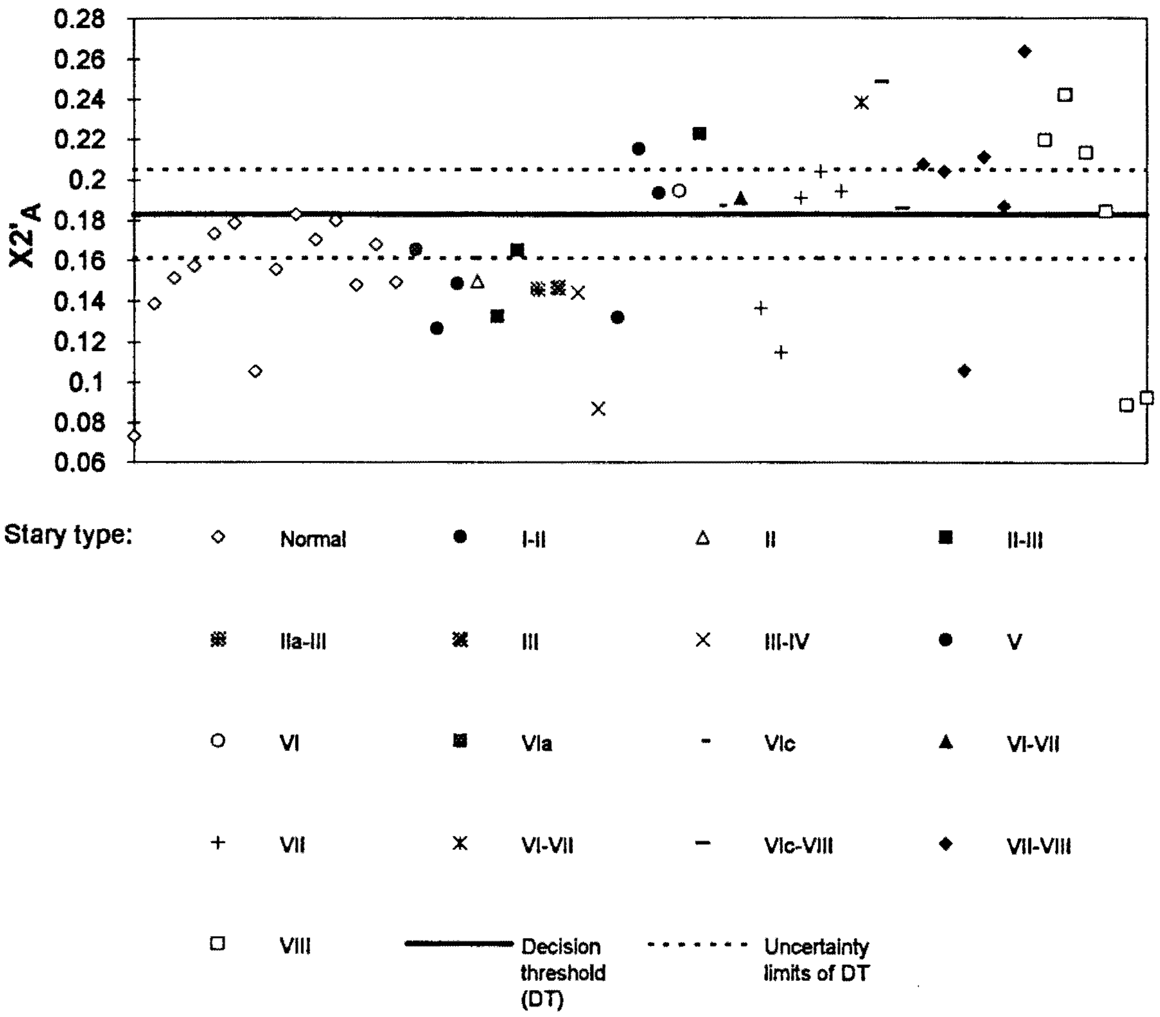

Figure 4.43 Scatter plot for the algorithm score $X2'_A = (\frac{I(530\,\text{nm})}{I(510\,\text{nm})})^{0.25} - (\frac{I(570\,\text{nm})}{I(550\,\text{nm})})$.

Uncertainty of individual data points: ± 12%

4.6 VARIATION OF DISTANCE BETWEEN DELIVERY/COLLECTION FIBRE AND SAMPLE

4.6.1 Aim and method

The aim of this experiment was to investigate how the fluorescence spectra depend on the distance between the delivery/collection fibres and the sample. The objective of the experiment was to simulate fluorescence during ablation, as it would be difficult to determine the fibre-end to sample distance precisely. The experimental setup of the fibres and sample is illustrated in Figure 4.44. In this experiment, the delivery fibre and the collection fibre were placed adjacent and parallel to each other and fixed together. This arrangement was then moved in steps of 1 mm of *z*, where *z* is the distance from the surface of the sample (sample classified as normal tissue).

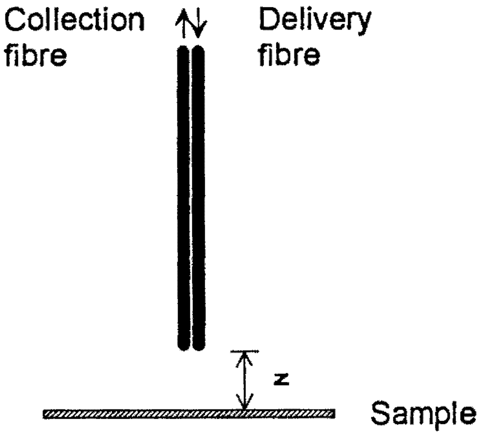

Figure 4.44 Geometry of the delivery/collection fibres relative to the sample

4.6.2 Results and analysis

The fluorescence lineshapes for distances, $z = 0, 1,..,8$ mm are shown in Figures 4.45a-i. From these figures it can be clearly seen that the fluorescence intensities are sensitive to *z*. There are significant changes in the fluorescence lineshapes as *z* increases from 0 mm to 2 mm. In this context, z = 0 mm denotes that the delivery/collection fibres are in contact with the sample. For $z \geq 2\,\text{mm}$, the fluorescence lineshapes show minor variation. An indication of the constancy of the fluorescence lineshapes for $z \geq 2\,\text{mm}$ is seen in Figure 4.46. In Figure 4.46, the fluorescence spectral intensities have been normalised to the fluorescence intensity at $\lambda = 380$ nm. Here, the normalised fluorescence intensity is defined as $R_{\text{norm}} = I(\lambda) / I(380\,\text{nm})$.

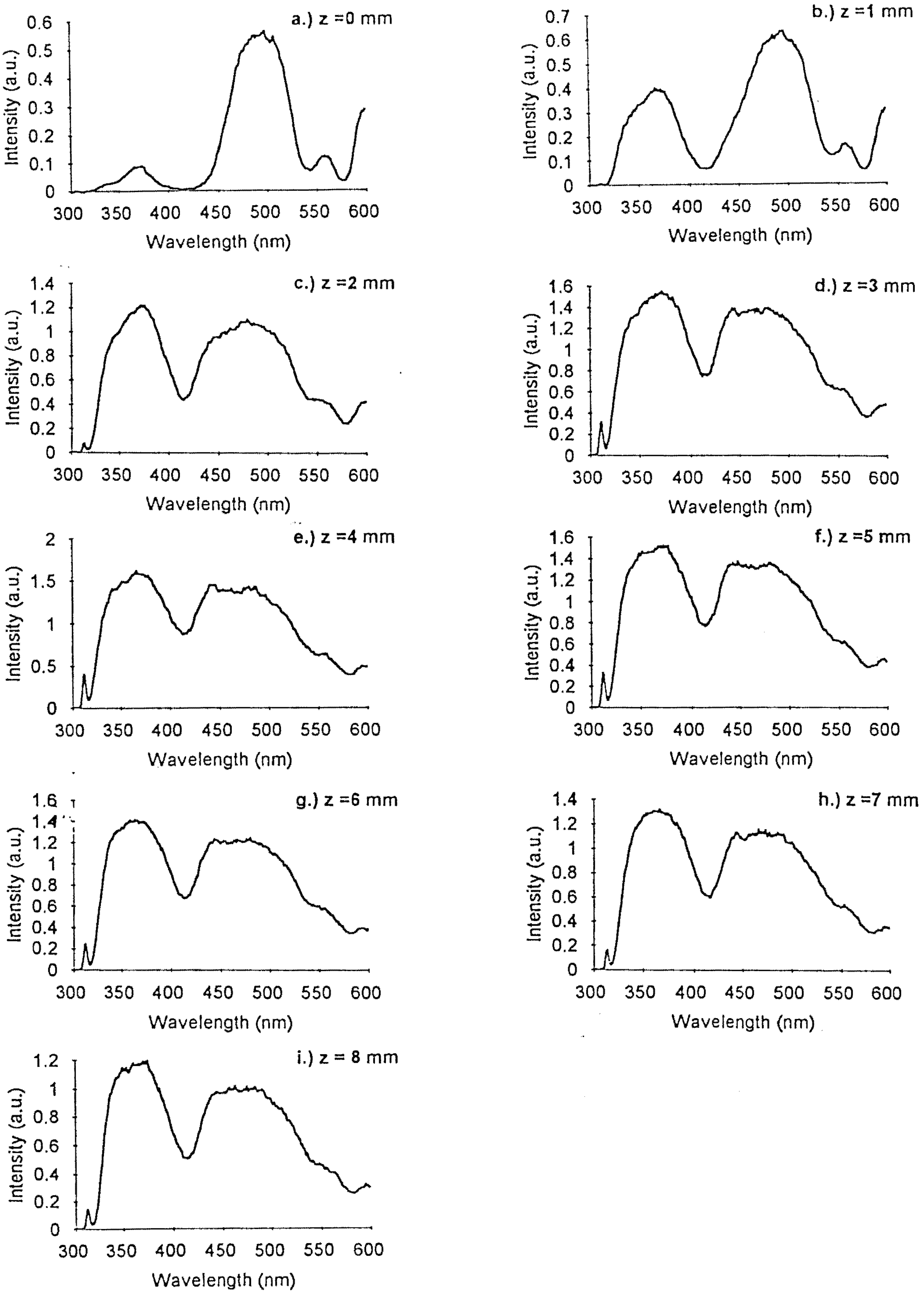

Figure 4.45 Changes in the fluorescence lineshapes for z = 0, 1,.., 8 mm

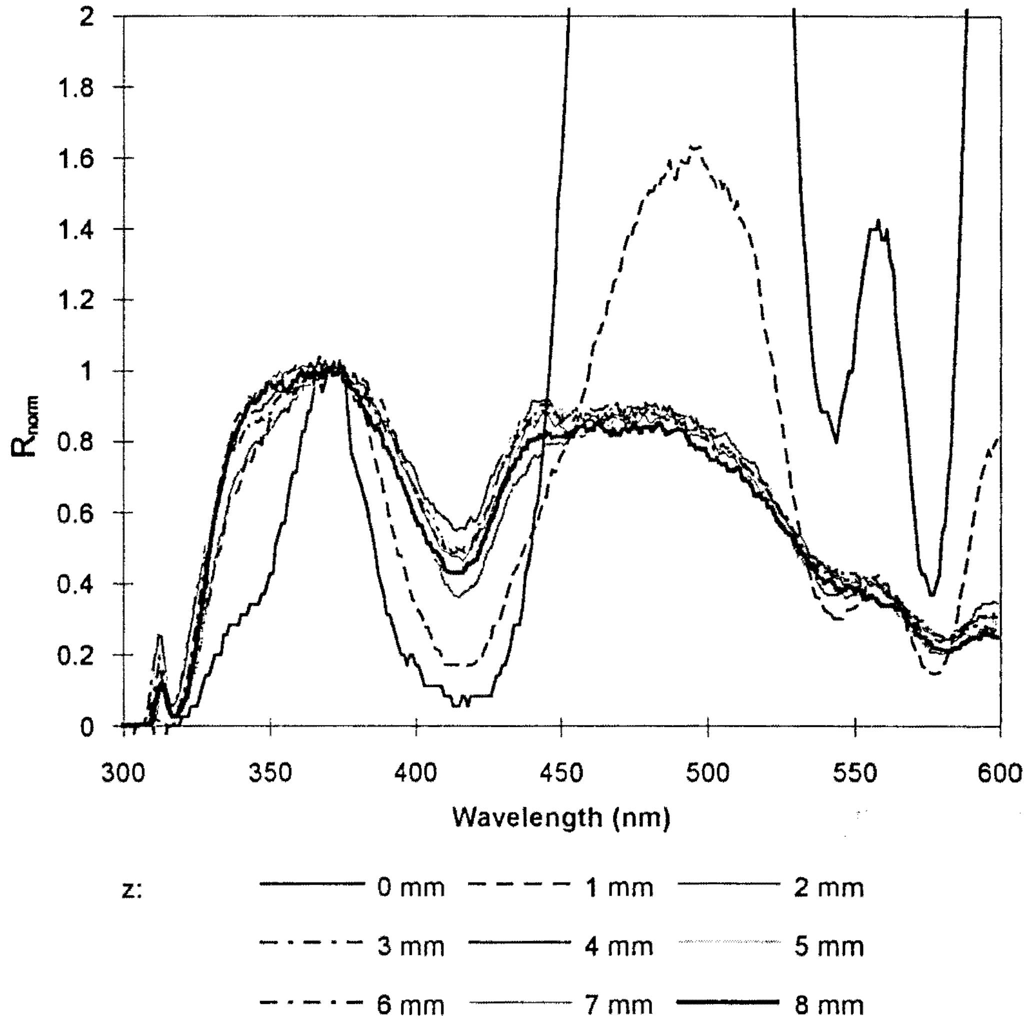

Figure 4.46 Plot of $R_{norm} = I(\lambda) / I(380\,nm)$ vs λ

We note from Figures 4.45a-i and Figure 4.46 that there are changes in the positions, intensity and widths of the main peaks and dips of the fluorescence spectra. As z increases the resolution of the peaks and dips, in general, decreases.

Lets denote the wavelengths at the intensity maxima or peaks at $\lambda \cong 370$ nm, $\cong 500$ nm and $\cong 560$ nm by P1, P2 and P3, respectively and the wavelength of the intensity minima or dips at $\lambda \cong 418$ nm, $\cong 540$ nm and $\cong 580$ nm by D1, D2 and D3, respectively. The intensity maxima and minima as a function of z are tabulated in Table 4.6

Table 4.6 Intensity maxima and minima as a function of z

	Wavelength at intensity maxima, λ (± 2 nm)			Wavelength at intensity minima, λ (± 2 nm)		
z (mm)	P1	P2	P3	D1	D2	D3
0	372	495	559	417	544	576
1	369	498	559	417	546	579
2	374	481	560	416	543	580
3	372	-	558	416	542	580
4	367	-	559	416	550	582
5	368	-	559	415	551	582
6	364	-	-	415	-	582
7	366	-	-	418	-	582
8	365	-	-	414	-	582

In summary, the following changes occur when z changes:

P1: The peaks are shifted towards shorter wavelengths as z increases. This shift is approx 10 nm ($364\,\text{nm} \le \lambda \le 374\,\text{nm}$).

P2: The general trend is a shift in the peaks towards shorter wavelengths as z increases. However, there is a larger shift (approx 20 nm) compared to P1.

P3: The peak lies within a very narrow wavelength range, viz., $558\,\text{nm} \le \lambda \le 560\,\text{nm}$. For $z \ge 6$ mm, the peak is no longer distinguishable.

D1: The dip lies within a very narrow wavelength range viz. $414\,\text{nm} \le \lambda \le 418\,\text{nm}$

D2: The dip is shifted towards longer wavelengths, i.e., $544\,\text{nm} \le \lambda \le 551\,\text{nm}$ as z increases. For $z \ge 6$ the dip is no longer distinguishable.

D3: There is a shift in the dip towards longer wavelengths. The wavelength shift is approximately 6 nm, viz., $576\,\text{nm} \le \lambda \le 582\,\text{nm}$.

a. Fluorescence intensity changes as a function of z

From Figure 4.46 it can be seen that there are steep increases in the fluorescence intensity, particularly where there are reabsorption dips (ie. at $\lambda \cong 420$ nm, $\cong 540$ and $\cong 580$ nm) for z = 0 mm, 1 mm and 2 mm. The ratio, $P_z = (I(\lambda,z) - I(\lambda,z-1)) / I(\lambda,z-1)$ may be used as a measure of the changes in the fluorescence intensity with increasing z (see Table 4.7). Some general trends in the values of P_z are evident. $P(\lambda,z)$ is very high for z = 1 mm and z = 2 mm in the wavelength range $320\,\text{nm} \le \lambda \le 440\,\text{nm}$. Furthermore, it can be seen from Table 4.7 that P_z is significantly higher at the reabsorption dips mentioned above.

Table 4.7 Values of P_z for λ = 320, 340,.., 600 nm

λ (nm)	$P_{z=1\,mm}$ (%)	$P_{z=2\,mm}$ (%)	$P_{z=3\,mm}$ (%)	$P_{z=4\,mm}$ (%)	$P_{z=5\,mm}$ (%)	$P_{z=6\,mm}$ (%)	$P_{z=7\,mm}$ (%)	$P_{z=8\,mm}$ (%)
320	600	200	319	-7	-19	-33	-30	-20
340	873	226	42	9	-3	-6	-9	-9
360	448	207	31	2	-4	-4	-7	-10
380	468	232	26	3	-5	-9	-8	-8
400	767	458	42	10	-7	-12	-9	-18
420	800	604	65	16	-8	-11	-10	-18
440	367	333	49	7	-7	-10	-9	-13
460	41	155	35	1	-6	-8	-7	-11
480	13	87	28	2	-5	-8	-12	-10
500	11	66	27	-1	-4	-9	-6	-15
520	12	92	26	1	-3	-7	-12	-10
540	65	255	48	6	-2	-10	-6	-18
560	29	166	44	<1	-3	-7	-10	-17
580	37	281	50	9	-5	-7	-11	-20
600	9	34	16	<1	-11	-11	-10	-15

Figure 4.47 shows the variation of the fluorescence intensity with z for λ = 320, 340, .., 600 nm. We note that for λ = 340, 360, .., 440 nm, $I(\lambda)$ increases rapidly for z = 0, 1, 2, 3 mm. For λ = 440, 460, .., 600 nm, there is a slight increase in $I(\lambda)$ for z = 0 mm and z = 1 mm, whence $I(\lambda)$ increases rapidly to z = 3 mm. In general, there is a smaller increase in $I(\lambda)$ from z = 3 mm to z = 4 mm. $I(\lambda)$ decreases slowly in the range z = 4, 5, .. 8 mm for λ = 540, 560, .., 600 nm and more rapidly for λ = 340, 360, .., 540 nm.

b. Integrated fluorescence intensity changes as a function of z

The integrated fluorescence intensity, $I_{int} = \int_{300\,nm}^{600\,nm} I(\lambda)\,d\lambda$ vs *z* (see Figure 4.48) displays a similar relationship to the plot of $I(\lambda)$ vs *z* shown in Figure 4.47. The integrated fluorescence intensity was determined by calculating the area under the fluorescence curve, as follows:

$$I_{int} = \int_{300\,nm}^{600\,nm} I(\lambda)\,d\lambda \cong [\sum_{i=300}^{600} (I(i+1\,nm)+I(i\,nm))]/2$$

It can be seen in Figure 4.48 that the slope is the steepest in the range z = 1 mm to z = 2 mm.

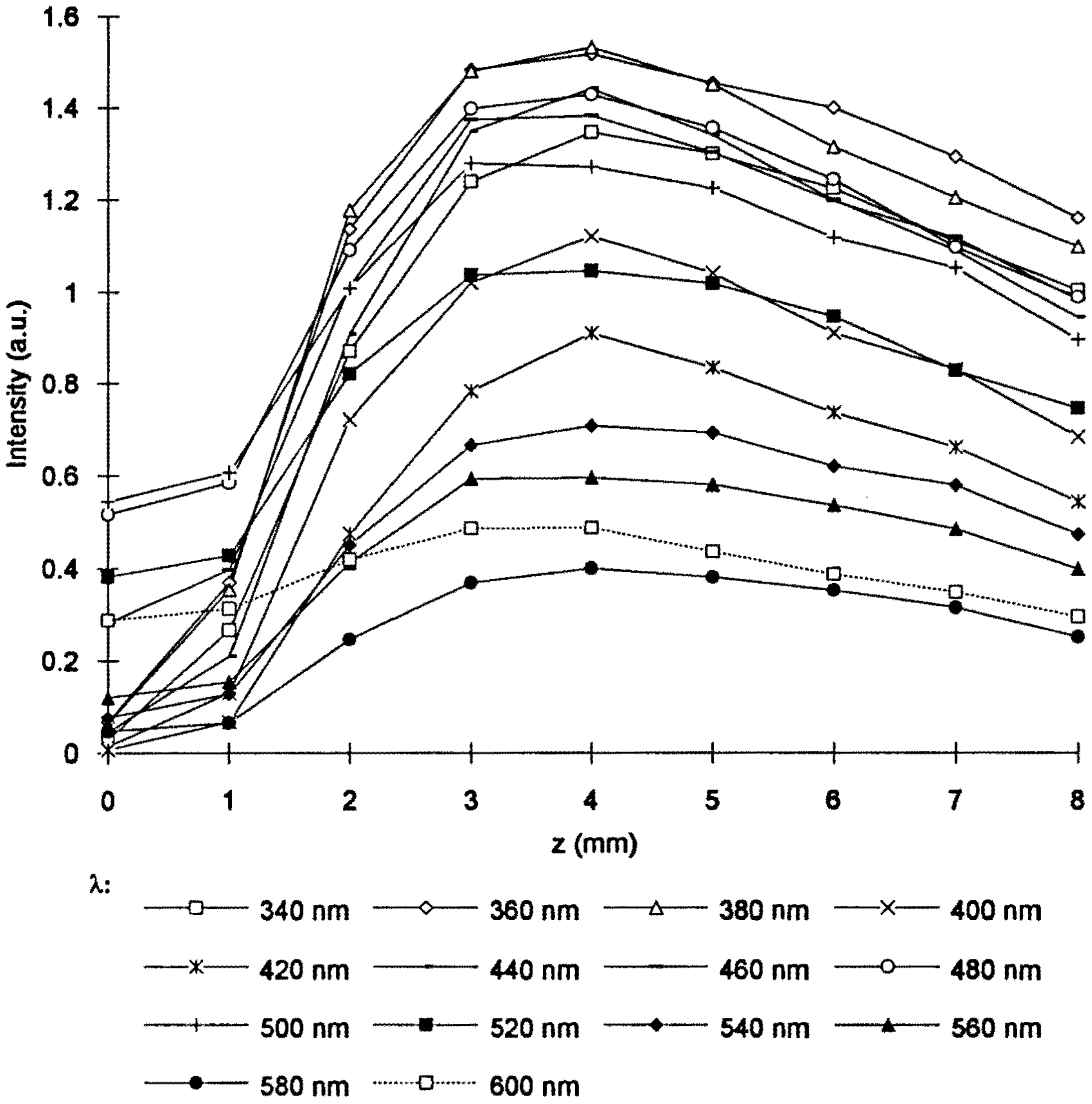

Figure 4.47 Plot of I(λ) vs *z*

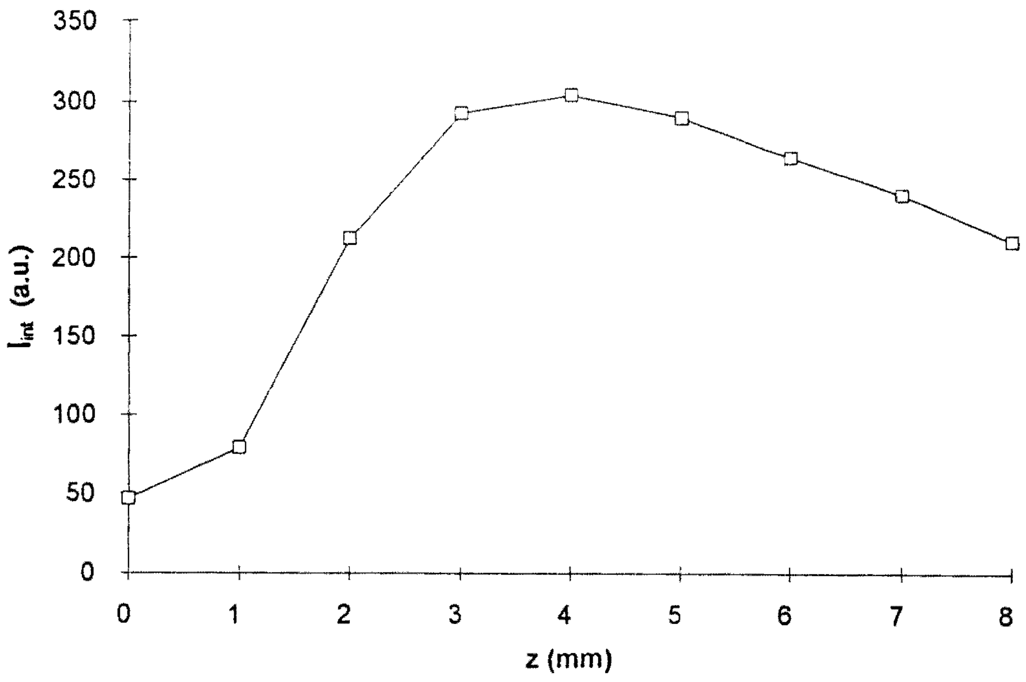

Figure 4.48 Plot of integrated fluorescence intensity (I_{int}) vs z

c. Change in normalised fluorescence intensities (normalisation intensity I(380 nm))

A plot of R_{norm} vs z for λ = 340, 360, .., 600 nm is shown in Figure 4.49. Analysis of the results show that R_{norm} decreases in the range $0\,\text{mm} \le z \le 1\,\text{mm}$ (except for spectral intensities at λ = 340 nm, 400 nm and 420 nm). $R_{norm} = I(500\,\text{nm}) / I(380\,\text{nm})$ experiences the steepest drop in the range $0\,\text{mm} \le z \le 1\,\text{mm}$. In general, R_{norm} is constant for $z \ge 4$ mm.

4.6.3 INTERPRETATION OF RESULTS

The fluorescence intensity detected at a tissue surface depends on the distribution of the excitation light in the tissue, the fluorescence quantum yield, the path length of the fluorescent light in the tissue, and the tissue absorption coefficient, μ_a, for the fluorescence (Keijzer *et al*, 1989). The path length is determined by both the actual distance between the excitation site and the detection point and the scattering properties of the tissue (scattering coefficient, μ_s; the mean cosine of the scattering angle, g, and the index of refraction mismatch at the surface). Since all these factors determining the fluorescence depend on wavelength, measured fluorescence spectra change when the point of measurement is displaced.

As the laser energy density at the surface of the tissue is lower than the threshold for ablation of vascular tissue, it may be concluded that the changes in the spectra are related to geometrical effects.

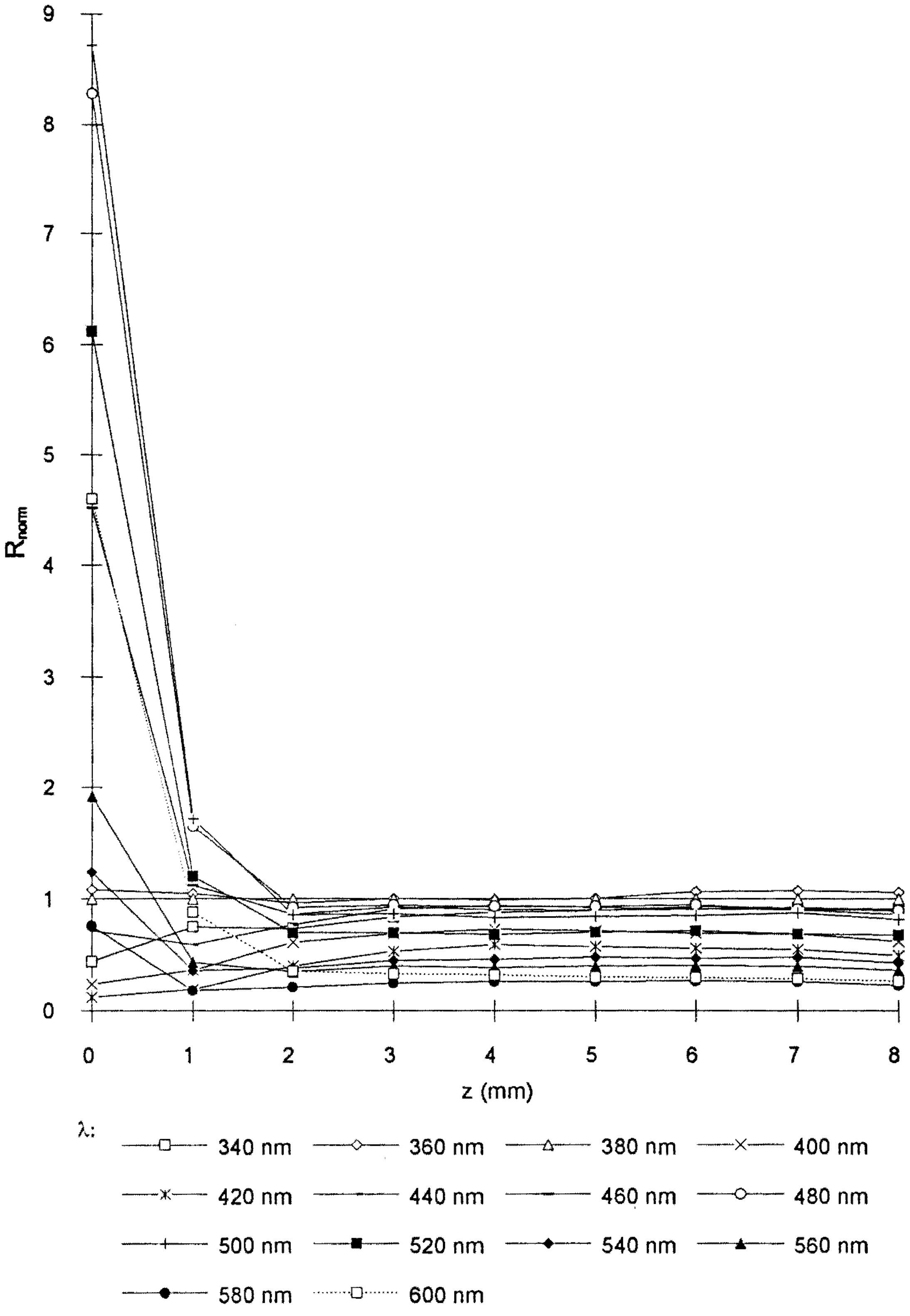

Figure 4.49 Plot of $R_{norm} = I(\lambda) / I(380\,nm)$ vs *z*

4.7 ANGLE OF SAMPLE RELATIVE TO DELIVERY/COLLECTION FIBRES

4.7.1 Aim and method

The purpose of this experiment was to investigate whether the fluorescence emitted by the sample depends on the angle of the sample relative to the delivery/collection fibres. The geometry of the set-up is shown in Figure 4.50. If the fluorescence depends on the angle of the sample relative to the delivery/collection fibre (which is the most likely *in-vivo* situation), this could complicate the interpretation of fluorescence signals.

In this experiment, the angle of the sample plane, α, relative to the delivery/collection fibre was varied from 90° to 160° in steps of 10° and the fluorescence lineshapes recorded for each value of α. The sample was classified as Stary type V.

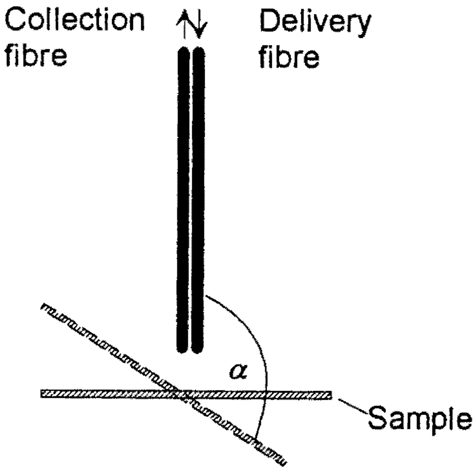

Figure 4.50 Geometry of delivery/collection fibres relative to change in angle of sample

4.7.2 Results and analysis

The fluorescence lineshapes for α = 90°, 100°, .., 160° are shown in Figure 4.51a. The fluorescence spectral intensities show a small decrease (< 21%) for α = 100°, .., 150° in the wavelength range 340 nm $\leq \lambda \leq$ 600 nm. There is a noticeable decrease in spectral intensities (< 31%) from $\alpha = 90°$ to $\alpha = 100°$ in the wavelength range 340 nm $\leq \lambda \leq$ 600 nm and a pronounced fall off in spectral intensities at α = 160° in the wavelength range 340 nm $\leq \lambda \leq$ 600 nm.

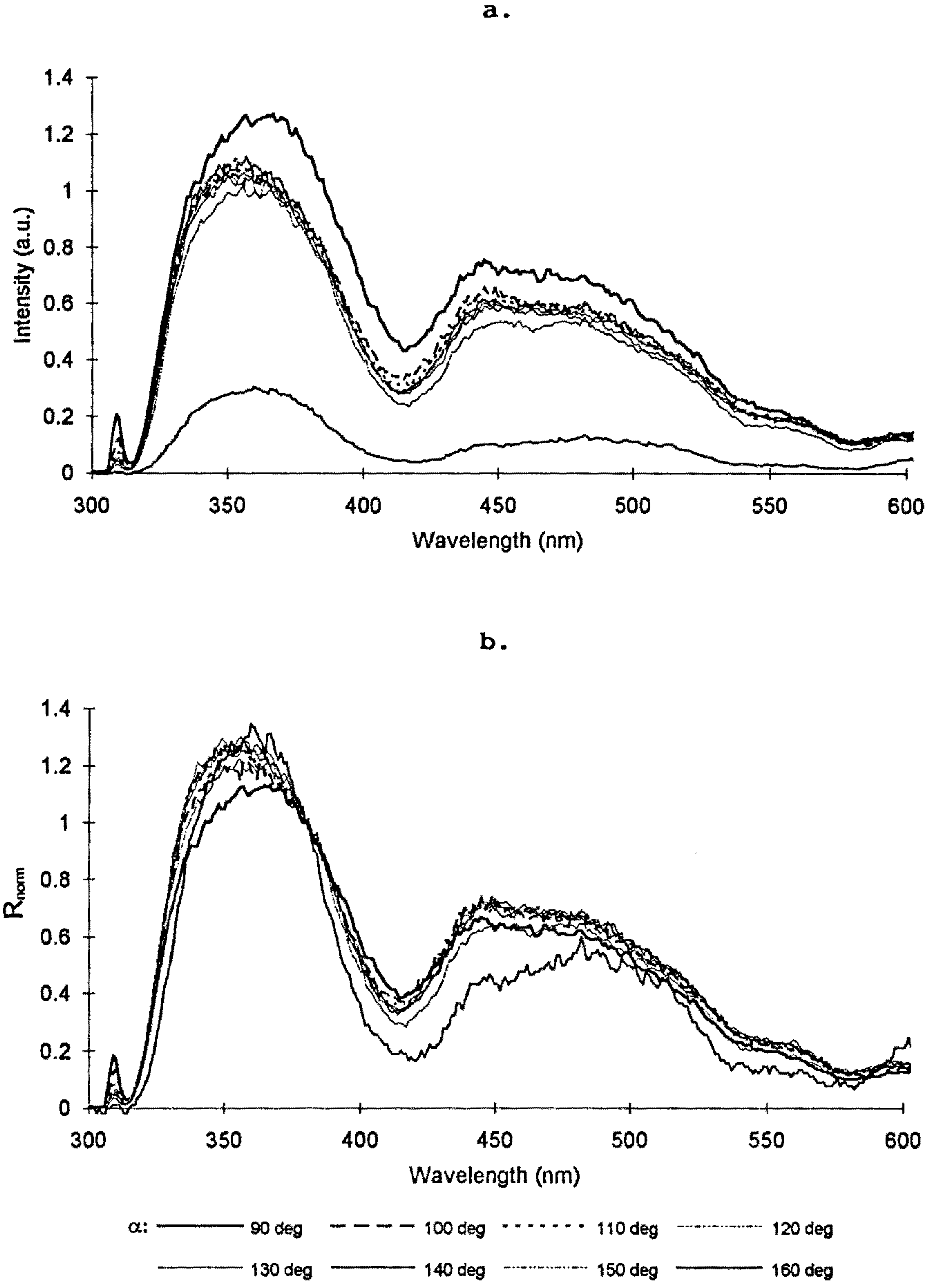

Figure 4.51 Results of varying α. **a:** actual fluorescence measurements. **b:** fluorescence intensities normalised to intensity at λ = 380 nm

Figure 4.51b shows a plot of the spectral intensities normalised to the spectral intensity at $\lambda = 380$ nm against wavelength.

We note from Figure 4.51b that R_{norm} is fairly constant for $\alpha = 90°, 100°, .., 150°$. R_{norm} for $\alpha = 160°$ is in general lower than R_{norm} for $\alpha = 90°, 100°, .., 150°$. This trend is also seen in the plot of R_{norm} vs α (see Figure 4.52).

Pronounced changes in R_{norm} with respect to α can be seen for $\lambda = 340$ nm and $\lambda = 360$ nm. Also noticeable is the fall off of R_{norm} from $\alpha = 150°$ to $160°$ for all wavelengths except $\lambda = 360$ nm and $\lambda = 600$ nm.

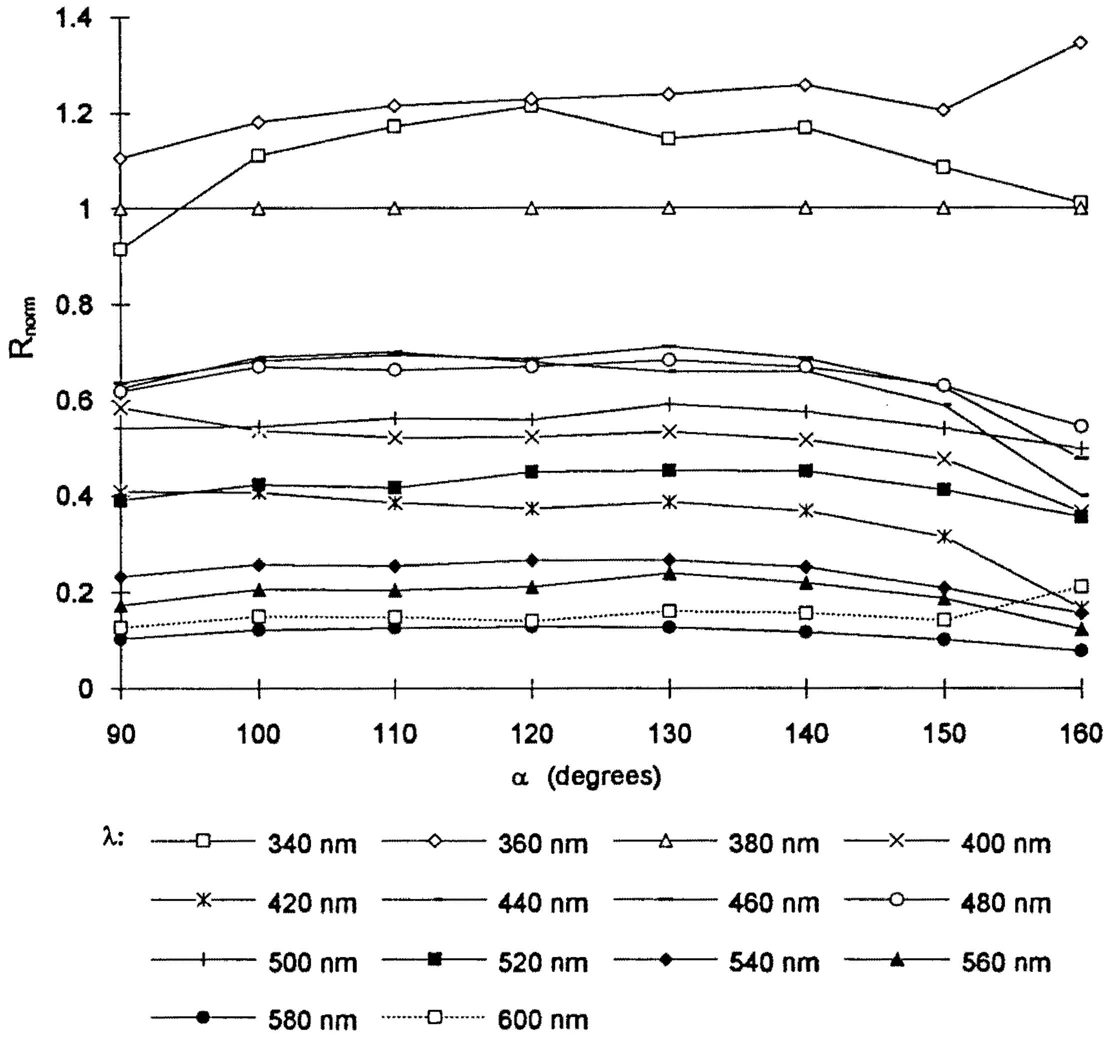

Figure 4.52 Plot of $R_{norm} = I(\lambda)/I(380 \text{ nm})$ vs α

4.8 ANALYSIS OF DIAGNOSTIC ALGORITHMS IN RELATION TO GEOMETRICAL EFFECTS

The algorithm scores $X1_A = (\frac{I(550\,nm)}{I(430\,nm)}) + (\frac{I(400\,nm)}{I(540\,nm)})^{0.5}$ and $X2'_A = (\frac{I(530\,nm)}{I(510\,nm)})^{0.25} - (\frac{I(570\,nm)}{I(550\,nm)})$ that produced the highest sensitivities for samples classified as normal/atherosclerotic tissue and samples classified as non-fibrotic/fibrotic tissue, respectively were tested to determine their sensitivity to the geometrical effects described in sections 4.6 and 4.7. Figures 4.53a, b and 4.54a, b show the algorithm scores $X1_A$ and $X2'_A$ plotted against z and α. It can be seen from these figures that the algorithm scores $X1_A$ and $X2'_A$ are sensitive to changes in z (normal sample) and α (Stary type V sample). Further computation was performed to determine which algorithms with high sensitivities are insensitive to changes in distance, z and angle, α.

From the analysis, the algorithms that produced the sensitivities ≥ 70% for normal/atherosclerotic tissue and non-fibrotic/fibrotic tissue are shown in Table 4.8.

Table 4.8 Parameters of algorithms with sensitivities ≥ 70%.

Algorithm*	λ_1 (nm)	λ_2 (nm)	λ_3 (nm)	λ_4 (nm)	p_1	p_2	p_3	p_4	DT	Sensitivity (%)
T	390	460	400	380	-1.00	-1.00	0.25	1.75	1.26 ± 0.16	70
W4	370	460	430	420					1.33 ± 3.43	70
	380	440	500	520					1.82 ± 3.64	70
X1	360	600	520	470	0.25	1.75			2.08 ± 0.06	70
	370	460	490	480	1.00	1.50			2.19 ± 0.07	70
	370	460	520	460	2.00	2.00			2.16 ± 0.20	70
	370	460	520	460	1.00	0.75			2.08 ± 0.08	70
	370	480	490	460	0.50	0.50			2.10 ± 0.32	70
	370	600	520	470	0.25	1.25			2.16 ± 0.05	70
	380	340	340	460	0.75	1.50			2.14 ± 0.08	70
	380	340	340	510	1.00	1.75			2.47 ± 0.13	70
	380	350	340	460	1.00	1.25			2.04 ± 0.08	70
	380	460	520	410	1.00	0.25			2.11 ± 0.08	70
	390	340	340	450	0.75	1.50			2.09 ± 0.07	73
	390	340	340	450	0.75	1.75			2.04 ± 0.07	73
	400	530	340	430	1.00	0.75			2.41 ± 0.24	73
	490	480	370	460	1.00	0.75			2.14 ± 0.05	70
	520	380	370	460	0.25	0.75			2.06 ± 0.05	70
	520	460	370	460	1.00	1.25			2.10 ± 0.11	70
	520	460	370	460	0.50	0.75			2.07 ± 0.06	70
	520	460	370	520	1.00	0.50			2.04 ± 0.04	73
	550	430	370	460	0.25	0.75			2.06 ± 0.08	70
X1'	350	600	590	340	0.50	1.00			2.23 ± 0.07	70

* The algorithms to distinguish between non-fibrotic and fibrotic tissue are denoted with a prime notation.

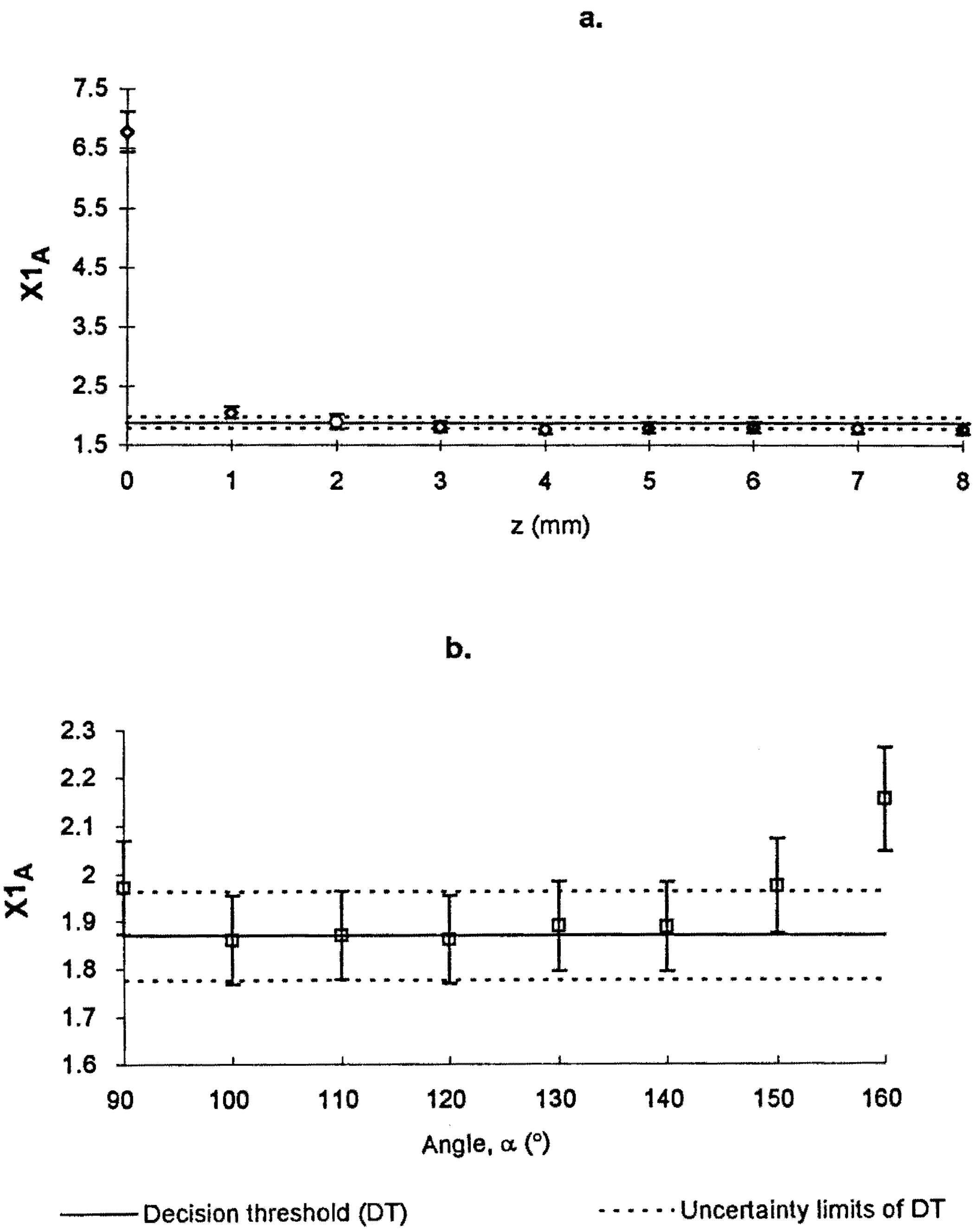

Figure 4.53 Plot of algorithm score $X1_A = (\frac{I(550\,nm)}{I(430\,nm)}) + (\frac{I(400\,nm)}{I(540\,nm))})^{0.5}$ vs *z* (Figure 4.53 a) and α (Figure 4.53b)

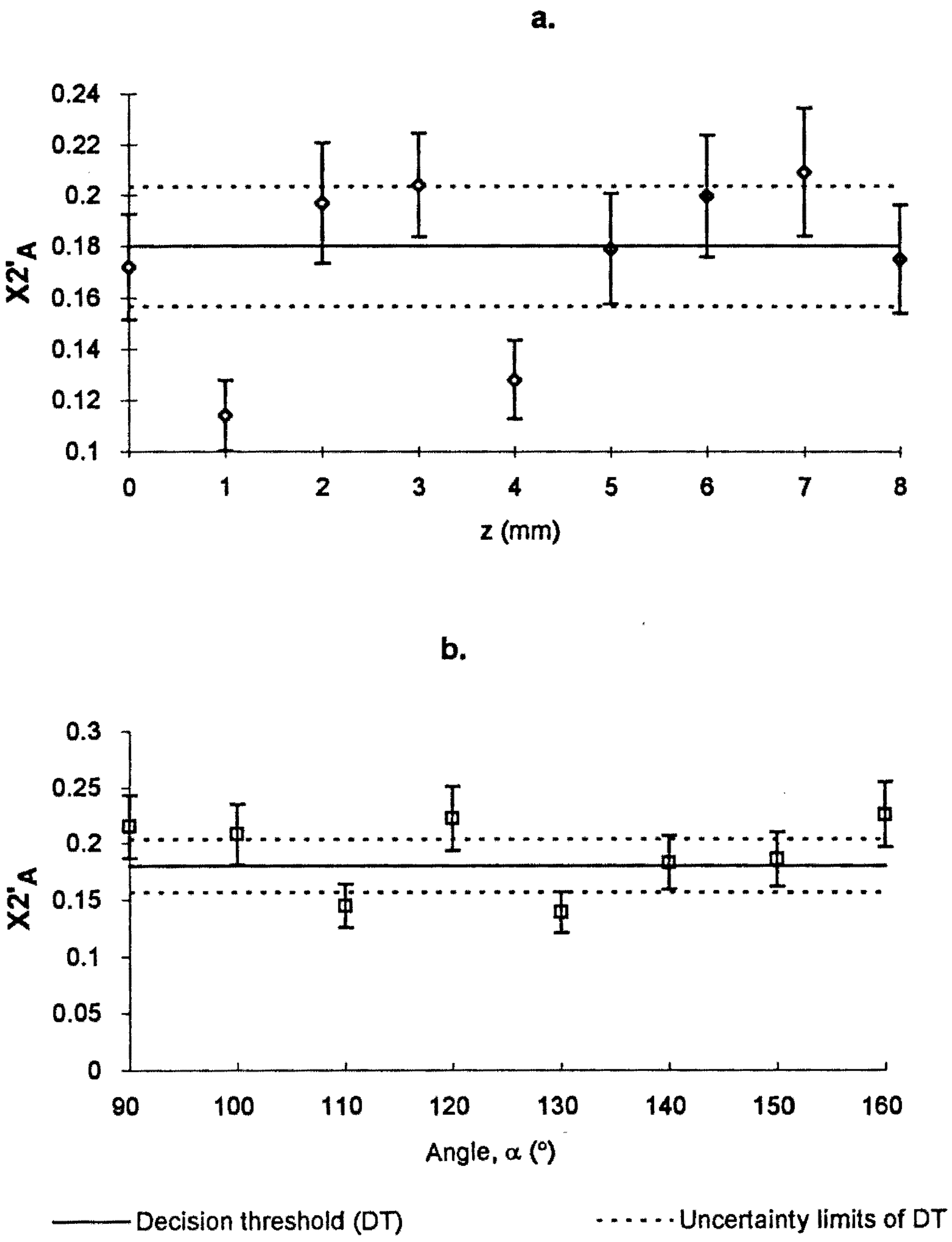

Figure 4.54 Plot of algorithm score $X2'_A = (\frac{I(530\,nm)}{I(510\,nm)})^{0.25} - (\frac{I(570\,nm)}{I(550\,nm)})$ vs z (Figure 4.54 a) and α (Figure 4.54b)

An examination of the algorithms presented in Table 4.8 shows that the algorithm defined as $X1 = (\frac{I(\lambda_1)}{I(\lambda_2)})^{P_1} + (\frac{I(\lambda_3)}{I(\lambda_4)})^{P_2}$ produced the most number of algorithm scores with sensitivities ≥ 70% that are insensitive to changes in *z* and α. Only one algorithm with sensitivity ≥ 70% intended to discriminate between non-fibrotic and fibrotic tissue was insensitive to changes in *z* and α. Four algorithm scores of sensitivities = 73% are able to discriminate between normal and atherosclerotic tissue.

An algorithm sensitivity of 73% means that the success rate of the algorithm's score to discriminate between normal tissue and atherosclerotic tissue is 100% for normal tissue, i.e., 14 out of 14 normal samples were correctly classified and 73% for atherosclerotic tissue i.e., 27 out of 37 atherosclerotic samples were correctly classified.

An algorithm sensitivity of 70% means that the success rate of the algorithm score to discriminate between non-fibrotic tissue and fibrotic tissue is 100% for non-fibrotic tissue i.e., 24 out of 24 non-fibrotic samples were correctly classified and 70% for fibrotic tissue, i.e., 19 out of 27 fibrotic samples were correctly classified.

Closer examination of Table 4.8 also reveals that the intensities at the dips in the fluorescence spectra due to fluorescence reabsorption at λ = 420 nm, 540 nm and 580 nm do not contribute significantly to the algorithms presented in Table 4.8.

A typical algorithm score that contains contributions from some of the major fluorophores found in arterial tissue, ie., tryptophan, λ = 340 nm and collagen/elastin, λ = 380 (Baraga *et al*, 1990), is:

$$X1_B = (\frac{I(380\,nm)}{I(340\,nm)})^{0.75} + (\frac{I(340\,nm)}{I(460\,nm))})^{1.50}$$

The scatter plot of this algorithm score $X1_B$ is shown in Figure 4.55 and plots of $X1_B$ against *z* and α are shown in Figures 4.56a and 4.56b.

The algorithm that had a sensitivity of 70% and was insenstitive to *z* and α to disriminate between non-fibrotic and fibrotic tissue is given by:

$$X1'_A = (\frac{I(350\,nm)}{I(600\,nm)})^{0.50} - (\frac{I(590\,nm)}{I(340\,nm))})$$

The scatter plot of this algorithm score $X1'_A$ is shown in Figure 4.57 and plots of $X1'_A$ against *z* and α are shown in Figures 4.58a and 4.58b.

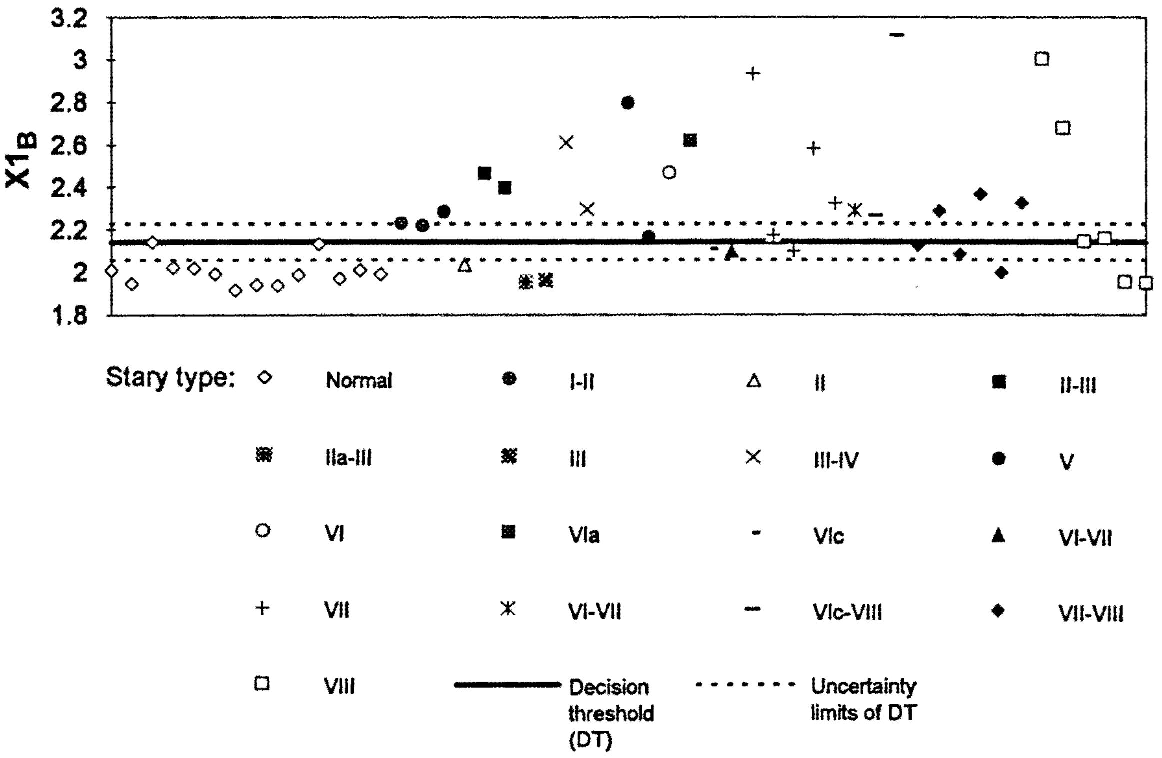

Figure 4.55 Scatter plot of algorithm score $X1_B = (\frac{I(380\,nm)}{I(340\,nm)})^{0.75} + (\frac{I(340\,nm)}{I(460\,nm)})^{1.50}$.

Uncertainty of data points: ± 4%

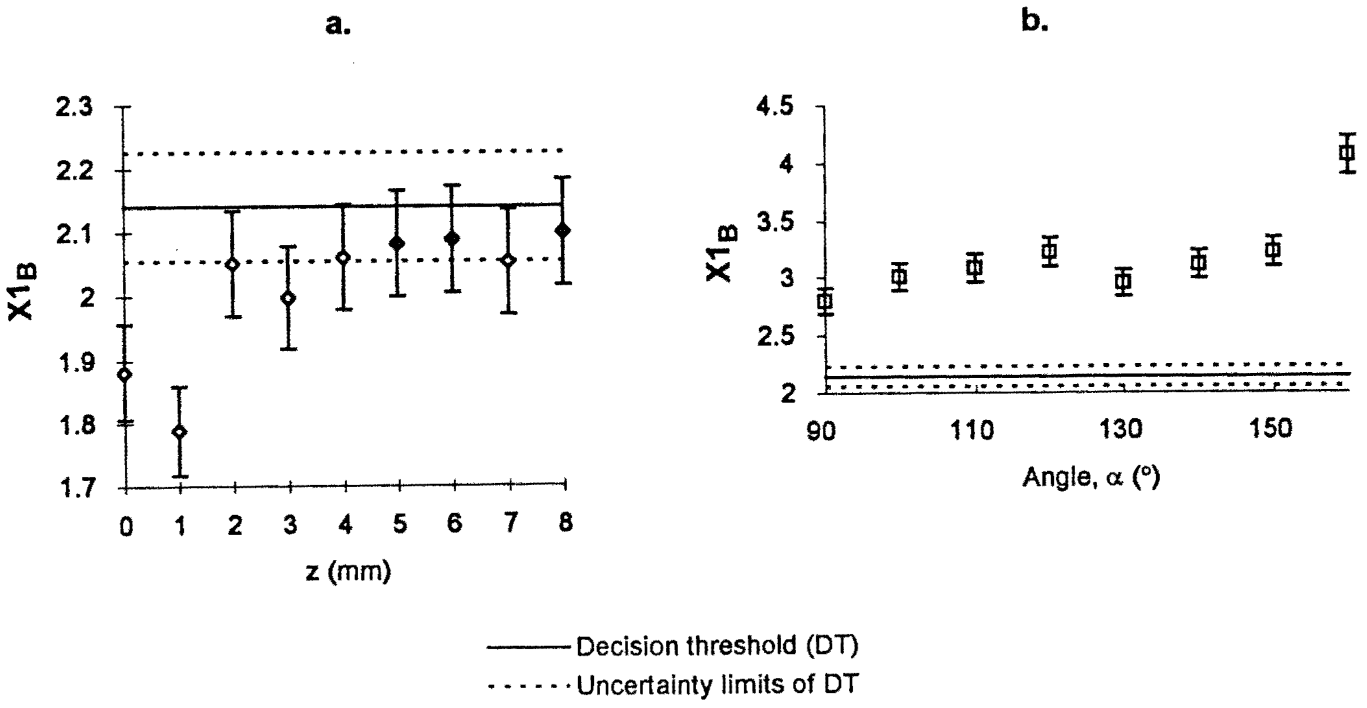

Figure 4.56 Plot of algorithm score $X1_B = (\frac{I(380\,nm)}{I(340\,nm)})^{0.75} + (\frac{I(340\,nm)}{I(460\,nm)})^{1.50}$ vs. *z* (Figure 4.56a) and α (Figure 4.56b)

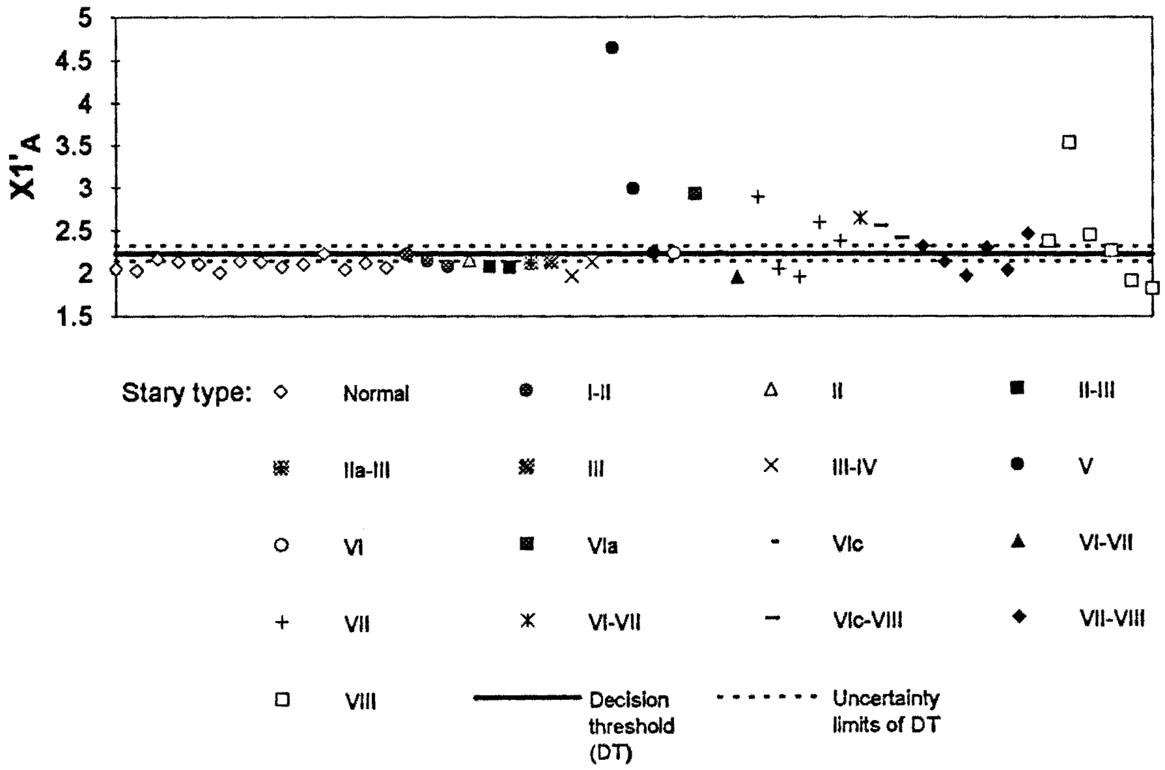

Figure 4.57 Scatter plot of algorithm score $X1'_A = (\frac{I(350\,nm)}{I(600\,nm)})^{0.50} + (\frac{I(590\,nm)}{I(340\,nm)})$.

Uncertainty of data points: ± 4%

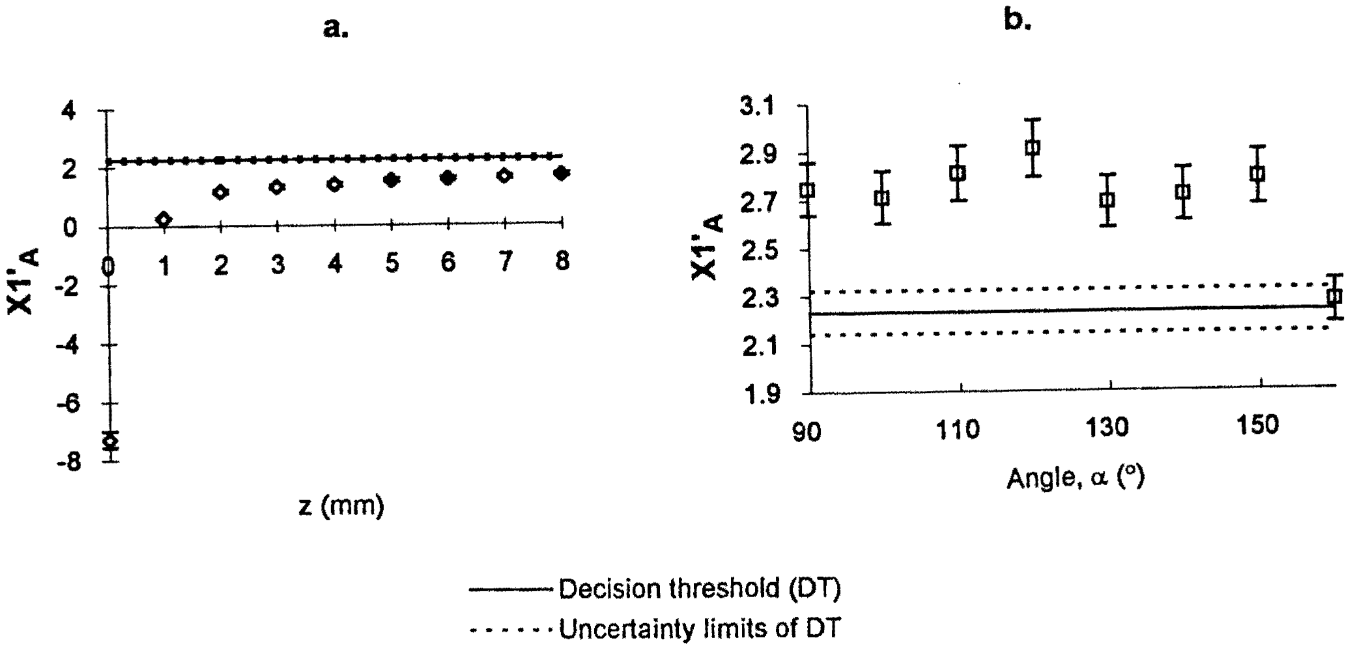

Figure 4.58 Plot of algorithm score $X1'_A = (\frac{I(350\,nm)}{I(600\,nm)})^{0.50} + (\frac{I(590\,nm)}{I(340\,nm)})$ vs.

z (Figure 4.58a) and α (Figure 4.58b)

CHAPTER 5

DISCUSSION AND CONCLUSIONS

5.1 METHODOLOGY

In this investigation, fluorescence characteristics of the intimas of three types of human arteries, viz., aorta, iliac and femorotibial arteries were investigated during irradiation by a pulsed XeCl excimer laser. For purposes of this study, the samples were grouped as normal arteries or as arteries in the different stages of atherosclerosis.

Extrapolation of the results from one artery type to another may not necessarily be straight forward as reported by Parazoglou *et al* (1990). They report that coronary arteries, for example, contain less collagen and elastin than other arteries. However, it is not clear whether the ratio of concentration of collagen to elastin is constant. Since collagen and elastin have been identified as the major fluorophores of the aortic wall (Baraga *et al*, 1990), the fluorescence lineshapes of the different arteries may differ. Furthermore, Papazoglou *et al* (1990) claim that smooth muscle cells are present in the coronaries and therefore the fluorescence spectra could be altered. Smooth muscle cells are generally recognised as a normal component of the intima in humans and in many other species, although some segments of arterial intima can be without smooth muscle cells (Stary, 1992b). Fitzmaurice *et al* (1989) found that the fluorescence in normal aorta and coronary artery were similar when using an argon laser (λ = 476 nm) as the source of excitation. In the description of human arterial intimas, Stary (1992b) makes no mention of the differences in arterial intimas. Since the intimas were probed by the XeCl laser in these experiments, it may be assumed that the type of artery will not alter the fluorescence spectrum.

For the excitation of fluorescence and the collection of the fluorescence radiation a dual fibre system was utilised, i.e., one fibre to deliver the excitation laser and the other fibre to collect the fluorescence signal. The single fibre system where a single fibre is used to deliver the excitation beam and ablate tissue as well as to collect the fluorescence signal is the configuration of choice as it obviates the need for additional bulk or size of the laser catheter. However, with the equipment available and proven in repeated use, it was felt appropriate to investigate thoroughly the properties of a separate delivery and collection fibre.

Fluorescence measurements were performed on the samples as soon as possible after removal from the patient. The postmortem interval varied from a few hours to a few days.

The samples were kept in an unfixed state in air at ambient temperature between removal from the patient and irradiation by the laser. Some researchers (e.g., Baraga *et al*, 1990) snap freeze the samples at < -50° until use. No fluorescence artefacts due to freezing were noted in the investigations of, for example, Baraga *et al* (1990).

The experiments were conducted with air as the medium between the fibres and the sample. While saline or blood would be the most likely situation *in vivo*, previous studies by Pettit *et al* (1990) and Morguet *et al* (1994) demonstrates that the surrounding medium (air, saline or blood) does not significantly alter the fluorescence spectra. Morguet *et al* (1994) report that the fluorescence spectra of calcified lesions are sensitive to the surrounding medium whereas the spectra of arterial media and lipid plaques are constant. In saline there is no clear cut difference between lipid plaques and calcified lesions. They used a XeCl laser (λ = 308 nm) as the source of excitation of the tissue. Furthermore, Pettit *et al* (1990) claim that the "fluorescence response is unaffected by arterial immersion in saline". They used a XeF laser (λ = 351 nm) as the source of excitation.

The measurement system employed in this study consisted of a spectrometer coupled to a boxcar averager and integrator system. A gated integrator amplifies and integrates the signal during the time the gate is open, ignoring noise and interference that may be present at other times. This results in an improved signal-to-noise ratio.

The fluorescence lineshape depends largely on the spectral response of the fluorescence detection system. A major component in the detection system is the spectral response of the photomultiplier tube. Here, a photomultiplier tube with a uniform response in the wavelength range 300 nm to 600 nm was used. This prevented any false fluorescence intensity maxima or minima. However, differences between spectra are more important than the spectral fluorescence lineshapes themselves.

For the classification of samples the protocol developed by Stary (1992b) was used. This protocol is recommended as it provides for a consistent way of classifying tissue.

5.2 FLUORESCENCE MEASUREMENTS

A considerable effort went into finding the optimal setting of the measuring system for the investigation of fluorescence from human arterial tissue. No experiments had been previously performed on arterial tissue in this laboratory.

The choice of filter that was used to reduce the interference from the scattered primary radiation meant that the fluorescence lineshapes were distorted in the wavelength range

$300 \leq \lambda \leq 350$ nm. For the purposes of comparison of the fluorescence spectra, the effect of the filter must be considered as a negligible but unavoidable artefact of the system.

The fluorescence spectral intensities are independent of the delay setting of the gate for delay times set at 1 ns, 10 ns, 100 ns and 1000 ns. This indicates that the fluorescence signal has a long decay time (> 1 μs). At delay settings of 10 μs no signal could be detected and this indicates that the fluorescence signal has completely decayed between 1 μs and 10 μs. Laufer *et al* (1988) reported that for tissue excited with a KrF excimer laser ($\lambda = 248$ nm) the fluorescence lasts no longer than 3.4 μs. This is within the range that was determined here for a XeCl excimer laser.

The study shows that fluorescence intensity from arterial tissues decreases exponentially with exposure to XeCl laser radiation. The pulse repetition frequency of the XeCl laser (10 Hz) means that the interval between pulses is 100 ms. The lifetime of the excited state is normally << 100 ms and hence all molecules should be in a relaxed state between laser pulses. Other processes within the tissue may result in the attenuation of the fluorescence intensities as a function of exposure to the excitation beam.

The fluorescence spectra obtained in this study are very similar to those obtained by Baraga *et al* (1990) and Laufer *et al* (1988). Baraga *et al* (1990) observed two peaks at 380 nm and 480 nm when excitation wavelengths between 306 nm and 310 nm were utilised. They also found a smaller peak at $\lambda = 335$ nm when the excitation wavelength was set at $\lambda = 308$ nm and attributed this peak to the fluorophore tryptophan. In this study, the peak at $\lambda \cong 335$ nm was suppressed due to the band-pass cut-off filter. However, on closer examination a shoulder around $\lambda \cong 340$ nm is visible in most of the fluorescence spectra. To some extent, the results are similar to those obtained by Laufer *et al* (1988). They found peak emissions at $\lambda = 370$ nm and $\lambda = 460$ nm (excitation radiation, $\lambda = 248$ nm) with a peak-to-peak intensity ratio consistent with the ratio obtained in this study for the various types of tissue. Morguet *et al* (1994) using a XeCl laser ($\lambda = 308$ nm) found that the autofluorescence spectrum of arterial tunica media in air typically displayed a plateau or a flat maximum between $\lambda = 370$ nm and 410 nm and a peak at $\lambda = 465$ nm of approximately double intensity.

Laufer *et al* (1988) found that the spectra of normal media was characterised by a broadband emission between 300 and 700 nm. Both maxima at $\lambda = 370$ nm and 460 nm were of equal relative intensity with an intensity ratio of 1.004 ± 0.087. In this study, the following result for the same ratio, viz., R= I(370 nm)/I(460 nm) = 0.95 ± 0.29 was obtained. This result is within the uncertainty range of the ratio obtained by Laufer *et al* (1988).

Morguet *et al* (1994) investigated the fluorescence from arterial media, lipid plaques and calcified lesions in air, saline and blood. It was found that the fluorescence spectra remained constant except for calcified lesions whose spectra changed with the surrounding optical medium. The fluorescence intensity for tissue with saline as the surrounding media was markedly lower than when it was in air. The fluorescence intensity of the spectra measured for tissue in blood was only slightly lower than when surrounded by saline.

Fluorescence spectra in this study were obtained from irradiation incident strictly perpendicular to the surface of tissue, for purposes of using the spectra to differentiate between normal and diseased arteries. There were significant changes in the fluorescence spectra as the distance between the sample and the delivery/collection fibres changed between 0 mm and 2 mm. The changes in the spectral intensities are not uniform for the range 0 mm $\leq z \leq$ 3 mm. This has serious implications for *in vivo* applications because the distance between the fibre and sample would be unknown. The present study was therefore crucial in order to propose algorithms that are insensitive to the changes in z.

When the sample angle, α, changed relative to the delivery/collection fibres, there was a very slight variation in the fluorescence spectra for angles $90° \leq \alpha \leq 150°$.

5.3 SPECTROSCOPIC IDENTIFICATION CRITERIA

The main aim of this study was to evaluate the fluorescence emitted by arterial tissue with a view to using it as a tool to develop optimal spectroscopic identification criteria (algorithms) to discriminate between normal and atherosclerotic arterial tissue.

A comparison of the absolute values of fluorescence intensities for the different tissue types as a basis for developing spectroscopic identification algorithms did not demonstrate sufficient analytical ability to achieve the aim of providing consistent methods of distinguishing abnormal intimal tissue, with the experimental method described in this thesis. Furthermore, comparison of absolute values of spectral intensities would be very difficult during *in vivo* applications due to change in the geometry of the fibre delivery and collection system as well as changes in the sample topology. Hence, algorithms that contain the ratio of spectral intensities and yield a dimensionless quantity were studied and analysed. There are many advantages in having dimensionless quantities as identification criteria as many problems that would otherwise be encountered in clinical work are eliminated, e.g., changes in sample topology.

Fourteen diagnostic algorithms that combine 2, 3 or 4 fluorescence spectral intensities chosen at 10 nm wavelength intervals in the range 340 nm to 600 nm were defined and applied to the fluorescence spectra. Diagnostic algorithms that are based on a limited number of spectral intensities will simplify clinical systems as optical multichannel analysers can be replaced by inexpensive narrow band filters and detectors. Thus practical applications of the finding of this thesis will be able to achieve a pragmatic balance between precision and technological simplicity. In determining the spectroscopic identification criteria, only wavelengths in integral multiples of 10 nm were considered. This was done on account of the fluorescence intensity not changing significantly within 10 nm.

The algorithms were defined in an arbitrary manner. The only condition being that the algorithms should yield a dimensionless quantity. There are numerous other algorithms that could be defined and applied to the fluorescence spectra. It is possible that higher success rates to distinguish between (a) normal and atherosclerotic tissue, and (b) non-fibrotic and fibrotic tissue would be achievable with these algorithms. Algorithms that combine more spectral intensities, i.e., > 5 spectral intensities may also improve the success rate. This is not certain, but it is clear that the necessary analytical equipment would be more complex and expensive.

The efficacy of the algorithms was evaluated by testing their sensitivity, specificity and predictive values. By maximising the specificities and predictive values of the algorithms, a decision threshold was calculated. The calculation of a decision threshold for the algorithm scores was based on optimising classification accuracy of the normal arteries. The shifting upwards of the decision threshold may be considered to reduce misclassification errors. For guidance of laser angioplasty, a decision threshold which increases the likelihood of correct classification of normal tissue is a requirement. Misclassification of atherosclerotic plaque as normal tissue may leave a greater amount of residual plaque whereas misclassification of normal artery wall as plaque risks vessel perforation. Higher algorithm sensitivities to distinguish between normal and atherosclerotic tissue and non-fibrotic and fibrotic tissue are also attainable but at the cost of a decrease in accuracy of detecting normal tissue as the specificities and predictive value of the algorithms will decrease.

All algorithms with high sensitivities contained contributions from a number of spectral intensities. These results do not necessarily support the empirical observation that the difference between the laser-induced fluorescence spectra of normal and atherosclerotic arterial tissue is manifested in a small number of important spectral features (O'Brien *et al*, 1990).

One of the characteristic features of the fluorescence spectra is the fluorescence intensity dips at $\lambda \cong 420$ nm, $\cong 540$ nm and $\cong 580$ nm due to fluorescence reabsorption by oxy-haemoglobin within the tissue. As noted previously, the fluorescence spectra may be significantly distorted due to a different permeability of tissue to haemoglobin postmortem (Pettit *et al*, 1990). It is important that the algorithms with the highest success rates for distinguishing between normal and atherosclerotic tissue do not contain spectral intensities of the aforementioned wavelengths. The algorithms proposed here that take into account geometrical effects do not contain spectral intensities that are distorted by oxy-haemoglobin.

The sensitivity of the algorithms was calculated by examining the algorithm score of each of the fluorescence spectra obtained from the 51 samples. The sensitivity was calculated by examining the algorithm score that correctly classified normal arteries without taking into account the uncertainties in the calculated data. Uncertainties in the algorithm scores varied and were obtained by examining the reproducibility of the fluorescence spectra. Uncertainties in the algorithm scores were generally low (< 10 %).

The algorithms with high sensitivities obtained for a fixed geometry i.e., $z = 2$ mm and $\alpha = 90°$ may fail to identify correctly normal/atherosclerotic and non-fibrotic/fibrotic tissue when there are significantly different values of z and α. This may have serious implications for *in vivo* studies. During in vivo procedures, ablation of the plaque will result in changes in z. This problem may be overcome by keeping z fixed. One way of doing this is to enclose the fibre tip of the collection fibre in a quartz glass thereby maintaining a fixed distance between the fibre tip an the sample. Algorithms proposed by other researchers (e.g., Baraga et al, 1990 and Morguet et al, 1994) were for fixed geometries. This limitation was avoided in the present work, by studying exhaustively the effect of variations in the geometrical parameters, z and α. Sensitive and specific algorithms were derived and studied with numeral variation as z and α varied within those ranges liable to be encountered in practice, in an *in vivo* situation.

Finally, the spectroscopic identification criteria established here can now be evaluated, *in vivo*, to determine its value as a means of differentiating between normal and atherosclerotic tissue as well as between non-fibrotic and fibrotic tissue.

5.4 LIMITATIONS OF STUDY

In this study, measurements of the fluorescence emitted by arterial tissue were performed in a gaseous (air) surrounding medium, *in vitro*. In an *in vivo* application, a liquid surrounding medium of blood or saline solution would be likely. However, Morguet *et al* (1994) and Pettit *et al* (1990) report that the fluorescence spectra , in general, remains unaffected by saline or blood as the surrounding medium (see section 5.1).

Fluorescence measurements were performed with the delivery/collection fibres making angles 90° - 160° to one sample. In, *in vivo* applications, the fibre will also be oriented at other angles to the axis of the vessel lumen, in regions where the vessels are straight for distances greater than $\approx$ 10 mm.

As further developments in laser associated technology are announced, in particular methods of producing radiation with different energies and leading it to the arterial intima, then the work described here can be modified, extended and repeated as necessary to ensure that further optimistaion in use of lasers for localisation and ablation of atheroma can take place.

5.5 CONCLUSIONS

This study had three goals: (a) to develop and evaluate spectral classification algorithms for discriminating normal and atherosclerotic arteries by their respective fluorescence spectra,(b) to determine whether the fluorescence signals could be utilised to diagnose the state of the tissue; and (c) to determine the influence of the geometry of the laser delivery and fluorescence collection system on the fluorescence signal.

(a) The results of this study show that fluorescence spectroscopy of arterial intimas may be used as a technique to distinguish between normal tissue and atherosclerotic tissue on the one hand and non-fibrotic and fibrotic tissue on the other. The sensitivity of the algorithm score $X1_A$ to discriminate between normal and atherosclerotic tissue is 84%. The sensitivity of the algorithm score $X2'_A$ to discriminate between non-fibrotic and fibrotic tissue is also 78%. These high algorithm sensitivities are remarkable in light of the heterogeneous nature of arterial tissue, especially atherosclerotic tissue.

(b) Due to the small sample population, no attempt was made to assess whether the fluorescence measurements may be utilised to diagnose the various stages of atherosclerosis of arterial tissue. However, with the algorithms proposed in this study we were able to discriminate between normal and atherosclerotic tissue as well as between non-fibrotic and fibrotic tissue with sensitivities of 84% and 78%, respectively.

(c) Investigations of the effects of the geometry of the delivery/collection fibres relative to the sample show that the fluorescence lineshapes can change dramatically with the distance, z, between the delivery/collection fibres and sample for $0 \text{ mm} \leq z \leq 3 \text{ mm}$. Variation of the angle of the delivery/collection fibres relative to the tissue surface does not significantly distort the fluorescence lineshapes. Several algorithms with sensitivities $\geq 70\%$ that are insensitive to the geometrical effects investigated are proposed to distinguish between normal and atherosclerotic tissue and non-fibrotic and fibrotic tissue.

This study shows that by using fluorescence spectroscopy together with the proposed algorithms, it is possible to discriminate between normal and atherosclerotic tissue and non-fibrotic and fibrotic tissue, *in vitro*. The results obtained in this study demonstrates the potential of fluorescence spectroscopy as a technique to guide laser ablation of atherosclerotic plaques *in vivo*.

APPENDIX A

ATHEROSCLEROSIS

This review is based on the article of Ross (1993).

A.1 INTRODUCTION

Atherosclerosis is not merely a disease in its own right, but a process that is the principal contributor to the pathogenesis of myocardial and cerebral infarction, gangrene and loss of function in the extremities. The process, in normal circumstances a protective response to insults to the endothelium and smooth muscle cells of the wall of the artery, consists of the formation of fibrofatty and fibrous lesions, preceded and accompanied by inflammation. The advanced lesions of atherosclerosis, which when excessive, become the disease and which may occlude the artery concerned, result from excessive inflammatory-fibro-proliferation response to numerous different forms of insult.

A.2 LESIONS OF ATHEROSCLEROSIS

The earliest recognisable lesion of atherosclerosis is the so-called "fatty streak", an aggregation of lipid-rich macrophages within the innermost layer of the artery wall, the intima. The ubiquity of the atherosclerotic process is attested to by finding of fatty streaks in the coronary arteries of half of the autopsy specimens from children aged 10 to 14. Animal observations have shown that fatty streaks precede the development of intermediate lesions, which are composed of layers of macrophages and smooth muscle cells and, in turn, develop into the more advanced, complex, occlusive lesions called fibrous plaques. The fibrous plaques increase in size and, by projecting into the arterial lumen, may impede the flow of blood. They are covered by a dense cap of connective tissue with embedded smooth muscle cells that usually overlays a core of lipid and necrotic debris. The fibrous plaques contain monocyte-derived macrophages, smooth muscle cells and T lymphocytes, many of which are activated, as evidenced by HLA-DR expression. Recent data have shown that most of the sudden deaths from myocardial infarcts are due to ruptures or fissures, particularly in the margins of the fibrous cap where there are more macrophages, resulting in haemorrhage into the plaque, thrombosis and occlusion of the artery.

A.3 RESPONSE TO INJURY AND ATHEROGENESIS

The hypothesis that an injury to the endothelium might precipitate the atherosclerotic process, was formally advanced in 1973. It has been continually modified particularly in 1986 to take account of accumulating observations. Manifestations of the dysfunction of the endothelium caused by injury, notably at branch points in the arterial tree, include increased trapping of lipoprotein in the artery and the appearance of specific adhesive glycoproteins on the surfaces of the endothelial cells.

Studies of animals with artificially induced hypercholesterolaemia have confirmed that three processes are involved in the formation of atherosclerotic lesions: (1) the proliferation of smooth muscle cells, macrophages and possibly lympocytes; (2) the formation by smooth muscle cells of a connective tissue matrix comprising elastic fibre proteins, collagen and proteoglycans; and (3) the accumulation of lipid and mostly free and esterified cholesterol in the surrounding matrix and the associated cells.

Progression of atherosclerotic lesions is thus marked by the accumulation of alternating layers of smooth muscle cells and lipid-laden macrophages. In monkeys and rabbits, as well as in humans, the arteries contain sites with retracted endothelial cells, which expose underlying lipid-filled macrophages, which, in turn, provide sites for platelet interactions leading to the formation of mural thrombi. Many of these exposed macrophages seem, as in other inflammatory responses, to be attempts by the macrophages to remove the accumulating lipid by circulating back to the lung, liver, spleen and lymph nodes. Advanced atherosclerotic lesions may develop at the same sites, particularly at branches and bifurcations, where the mural thrombi occur.

The formation of fibrous lesions in response to injury is not in itself remarkable; wound healing follows such a course, for example. But the response to arterial injury differs from that to the injury of most other tissues and organs in two respects. First, the principal source of connective tissue in the arterial wall is the smooth muscle cell. Second, the sources of arterial injury (hypercholesterolaemia, hypertension, cigarette smoking, diabetes, obesity and so on) are likely to be chronic, so that the progression from fatty streak to fibrous plaque is unlikely to be interrupted or, at best, may be episodic.

APPENDIX B

EXCIMER LASERS

B.1 INTRODUCTION

Excimer lasers form a family of lasers in which light is emitted by a short-lived molecule made up of one rare gas atom (e.g., argon, krypton, or xenon) and one halogen atom (e.g., fluorine, chlorine, or bromine). First demonstrated in the mid-1970s, excimer lasers have become important because they are the most powerful practical ultraviolet lasers. They also rely on an interesting and unusual set of physics principles (Hecht, 1988).

B.2 PHYSICAL FUNDAMENTALS

Rare-gas halides are peculiar molecules that emit laser light as a result of an unusual type of electronic transition. The two atoms are bound only when the molecule is in an excited state. That is the upper laser level. When the molecule decays to the ground state, which is the lower laser level, the molecule disintegrates. That produces a population inversion in a rather unusual way - there can't be any molecules in the lower laser level because the atoms are not bound together. Figure B.1 shows the energy levels of a typical rare-gas halide as a function of the spacing between the two atoms in the molecule, R (the rare gas) and H (the halide). The dip in the excited state curve shows where the molecules are metastable; the absence of a dip in the ground-state curve indicates that the molecules fall apart. When the molecule is excited, the energy is at a minimum when the two atoms are a certain distance apart, trapped in a potential well. When they are in that potential well, they can occupy several vibrational levels as well (shown as horizontal lines in the potential well). However, in the "ground state," with the lowest possible energy, there is no bonding energy to hold the two atoms together, and the molecule disintegrates (lower curve).

Excimer lasers are excited by passing a short, intense electrical pulse through a mixture of gases containing the desired rare gas and halogen. In general, 90% or more of the mixture is a buffer rare gas (typically helium or neon) that does take part in the reaction. The mixture contains a small percent of the rare gas (argon, krypton, or xenon) that becomes part of the excimer molecule, and a smaller fraction of molecules that supply the needed halogen atoms. The halogen atoms may come from halogen molecules such as F_2, Cl_2, or Br_2, or from molecules that contain halogens such as nitrogen trifluoride (NF_3). The reasons for avoiding pure halogens is their very reactivity.

Electrons in the discharge tube transfer energy to the laser gas, breaking up halogen molecules and causing formation of electronically excited molecules like xenon fluoride (XeF*, * indicating excited). The reactions involved are very complex, and depend on the type of gases. The molecules remain excited for about 10 ns, then drop to the ground state and dissociate. The molecular kinetics (as well as the duration of the driving electrical pulses) limit laser operation to pulses lasting tens or hundreds of ns. The energies involved are large, and output is at ultraviolet wavelengths.

Excimer laser repetition rates depend more on the power supply than on the gas. The principal limitation is speed of the high-voltage switches. The highest repetition rates are around 1000 Hz, but more typical values are tens to a few hundreds of Hertz. Pulse energies range from about 10 mJ to a few Joules, and differ according to the gases, with KrF and XeCl generally the most energetic. Average power - the product of pulse energy times repetition rate - can reach a few hundred Watts, although lower values are more common. In general the pulse energy tends to decrease with repetition rate.

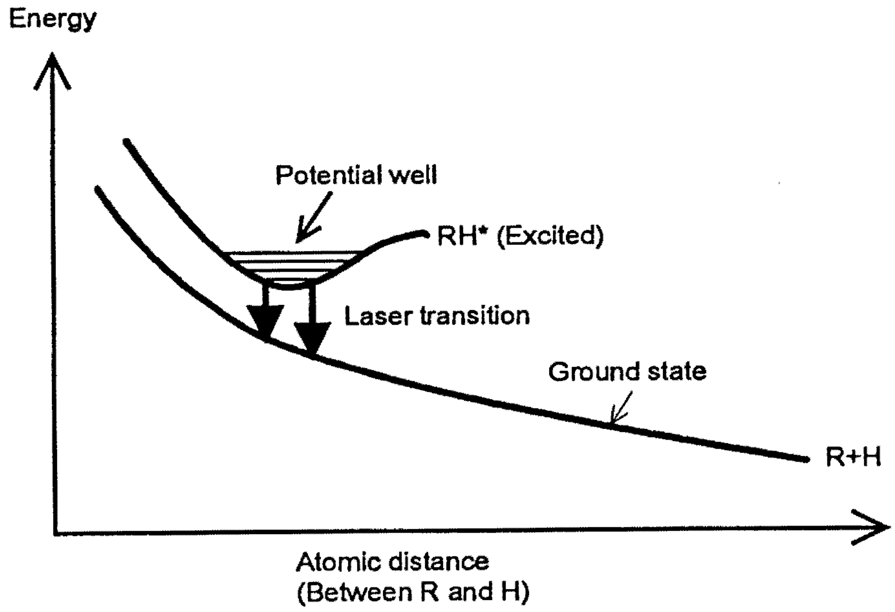

Figure B.1 Internal energy of a rare-gas halide molecule in excited and ground states.

B.3 STRUCTURE OF EXCIMER LASERS

Excimer lasers have such high gain that they almost usually do not need cavity mirrors. In practice, excimer lasers have fully reflective rear mirrors and uncoated output windows that reflect a few percent of the beam back into the cavity and transmit the rest.

As in other high-gain pulsed lasers, the discharge in an excimer laser is perpendicular to the length of the tube. The design is similar to that of a TEA CO_2 laser, except that excimer laser tubes must resist attack by the highly corrosive halogens in the laser gas. Excimer laser tubes are filled with the laser gas mixture, then sealed and operated for a limited number of pulses until the gas needs to be replaced. The tube's total volume is much larger (typically 100 to 1000 times) than the volume where the discharge excites laser action. Often, the gas is passed through a recycling system that helps regenerate the proper gas mixture and extend the life of the gas fill. The laser's pulse energy decreases with time, until the spent gas must be pumped out of the laser and replaced. The number of pulses depends on the gas, and can reach many million for longer-lived gases such as xenon chloride.

APPENDIX C

FLUORESCENCE

C.1 INTRODUCTION

Fluorescence is the process of emission of radiation which accompanies the spontaneous transition of a molecule from an excited state to a lower energy level. This process is best illustrated by the Jablonski diagram shown in Figure C.1 (Lakowicz, 1983).

The ground, first, and second electronic states of the molecule are depicted by S_0, S_1, S_2, respectively. At each of these electronic energy levels the molecule can exist in a number of vibrational energy levels, depicted by 0, 1, 2, etc.

When a molecule (fluorophore) absorbs light radiation, it is usually excited to some higher vibrational level of either S_1 or S_2. Most molecules relax to the lowest vibrational level of S_1 in a process called internal conversion which generally occurs within 10^{-12} s. The molecule can return from the excited state into the ground state by emitting the energy difference as heat or in the form of a photon, or by inducing a chemical reaction. This emission of radiation is called fluorescence.

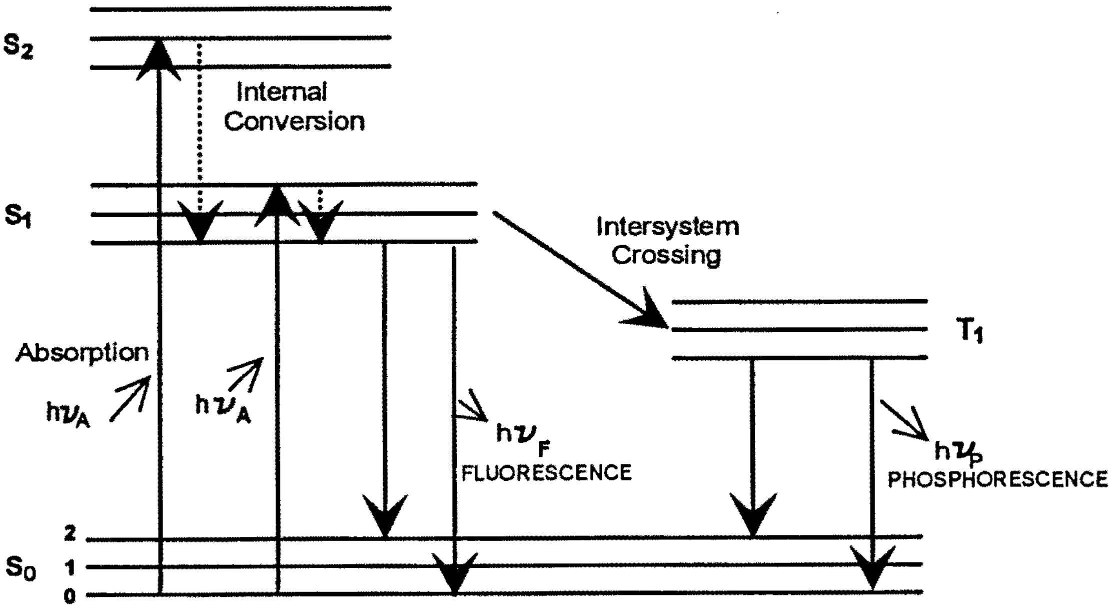

Figure C.1 Jablonski diagram

Since fluorescence lifetimes are typically about 10^{-8} s, internal conversion is generally complete prior to emission. Hence, fluorescence emission generally results from the thermally equilibrated state.

Molecules in the S_1 state can also undergo conversion to the first triplet state T_1. Emission from T_1 is termed phosphorescence, and generally is shifted to longer wavelengths (lower energy) relative to the fluorescence. Conversion of S_1 to T_1 is called intersystem crossing. Transition from T_1 to the ground state is forbidden, and as a result the rate constant for such emission is several orders of magnitude smaller than those of fluorescence. Although not indicated explicitly in Fig C.1, a variety of other processes can influence the fluorescence emission. These factors include solvent effects, solvent relaxation, quenching, and a variety of excited state reactions.

C.2 CHARACTERISTICS OF FLUORESCENCE EMISSION

C.2.1 Stokes shift

Except for atoms in the vapour phase, one invariably observes a shift to lower wavelength (i.e., loss of energy) of the emission relative to the absorption. This phenomenon was first observed by Stokes in 1852.

There are two main causes of Stokes shift. Firstly, there is a rapid decay to excited vibrational levels of S_1. Secondly, fluorophores generally decay to excited vibrational levels of S_0, resulting in further loss of vibrational energy.

C.2.2 Invariance of the emission spectrum with excitation wavelength

The same fluorescence emission spectrum is generally observed irrespective of the excitation wavelength. When a molecule is excited into higher electronic and vibrational levels, the excess energy is quickly dissipated, leaving the fluorophore in its lowest vibrational level of S_1. This relaxation occurs in about 10^{-12} s and is presumably a result of a strong overlap among numerous states of nearly equal energy. Because of this rapid relaxation, emission spectra are usually independent of the excitation energy.

C.2.3 Mirror image rule

Generally, the fluorescence emission spectrum appears to be a mirror image of the absorption spectrum, specifically the absorption representing the S_0 to S_1 transition (Figure C.2).

The generally symmetric nature of these spectra is a result of the same transitions being involved in both absorption and emission, and the similarities among the vibrational energy levels of S_0 and S_1. In many molecules these energy levels are not significantly altered by the different electronic distributions of S_0 and S_1. According to the Franck-Condon principle, all electronic transitions are vertical, that is, they occur without change in the position of the nuclei. As a result, if a particular transition probability (Franck-Condon Factor) between the 0 and 2nd vibrational levels is largest in absorption, the reciprocal transition is also most probable in emission.

Although often true, many exceptions to the mirror image rule occur. Deviations from the mirror image rule usually indicate a different geometric arrangement of nuclei in the excited state as compared to the ground state. Nuclear displacements can occur prior to emission because of the relatively long lifetime of the S_1 state.

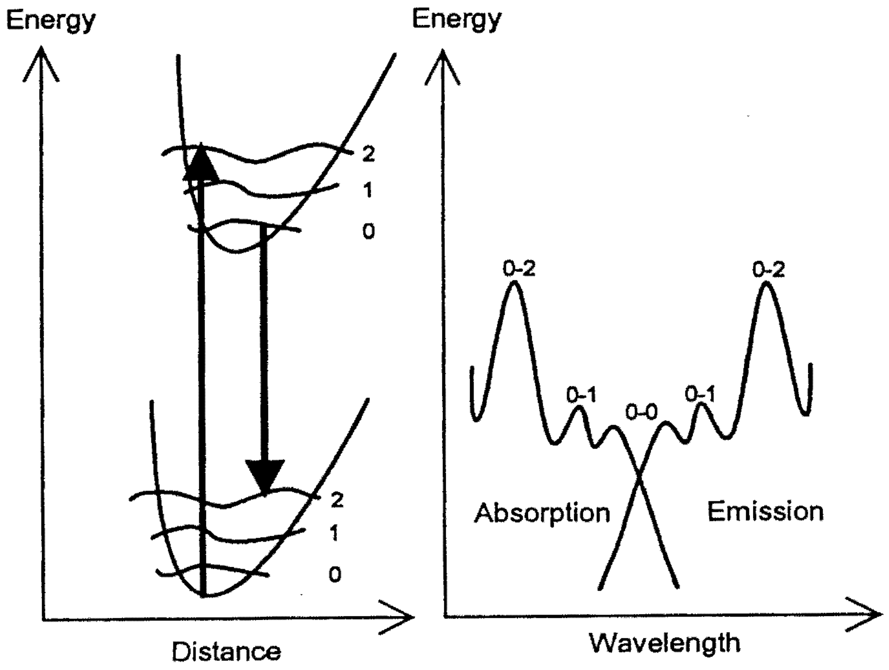

Figure C.2 Mirror image rule and Franck-Condon factors

C.3 FLUORESCENCE LIFETIMES

Upon withdrawal of the exciting source of radiation, the fluorescence intensity of a solution of fluorescent molecules decays with a rate characteristic of a first-order process, like radioactive decay. The relationship between the intensity change in fluorescence with time and the original fluorescence can be expressed by:

$$I = I_0 e^{-t/\tau}$$

where
I : fluorescent intensity at time t
I_0 : maximum fluorescence intensity during excitation
t : time after removing the source of excitation
τ : average lifetime of the excited state

In fluorescence studies, $t = \tau$ is also the time required for the fluorescence intensity to decay to 1/e of its initial value.

C.4 FLUORESCENCE QUANTUM YIELDS

The percentage of the absorbed energy which can be re-emitted as fluorescence is indicated by the term "quantum yield of fluorescence" designated as Φ, where

$$\Phi = \frac{number\ of\ quanta\ emitted}{number\ of\ quanta\ absorbed}$$

In the absence of any perturbations the emitted fluorescence is equal to the absorbed radiation and $\Phi = 1$. The lifetime of the excited state under these ideal conditions is referred to as Φ_0 and can be estimated from absorption data.

APPENDIX D

DEFINITION OF ARTERIAL INTIMA

This review is based on the the article of Stary (1992a)

The intima is defined as the region of the arterial wall from and including the endothelial surface at the lumen to the luminal margin of the media. The internal elastic lamina, generally considered part of the media, denotes the border between intima and media. However, a well-defined internal elastic lamina is absent in some parts of geometric transitions of arteries such as bifurcations, branch vessels, and curvatures. Thus, in these regions, recognition of the demarcation between intima and media may be difficult.

The thickness of arterial intima is not uniform. The criteria for normal thickness should recognise a broad range conveniently expressed quantitatively as the intima:media ratio. The ratio may vary from about 0.1 to 1.0 or more in normal arteries of humans.

Thick segments of intima exist in arteries obtained from healthy human subjects of all ages and from many other species. The thick segments may be focal (eccentric) or they may be more extensive (diffuse). They represent physiological adaptations to changes in flow and wall tension.

At vascular transitions such as bifurcations or trifurcations, normal structural reorganisations of the arterial wall, themselves localised thickenings, may overlap or fuse with intimal thickening caused by physiological adaptation. Structural reorganisations involve thickening of the deep (musculoelastic) intima layer and of the adjacent inner media. In regions of vascular transitions, the internal elastic lamina is partly or completely absent, and the intima and media may appear as a unit, indistinguishable from each other. Although it is sometimes difficult to distinguish how much of a particular thickening is intima or media and how much is of the adaptive or reorganizational type, the structures are composed of "normal" elements, differing clearly from atherosclerotic changes and those of other conditions. The difference between normal and pathological structure is clear when vessels are studied with appropriate methods.

The arterial intima is composed of two layers. The layers may be absent or barely visible by light microscopy in segments of arteries with a very thin intima. In segments with adaptive thickening of the eccentric or diffuse type, the layers are clearly visible. The inner layer, subjacent to the lumen, has been called the proteoglycan layer because it contains an abundance of finely reticulated nonfibrous connective tissue identified as containing proteoglycan ground substances by electron microscopy. Elastic fibres are scarce here. Smooth muscle cells are of both the rough endoplasmic reticulum-rich (synthetic) and myofilament-rich (contractile) phenotypes. They occur as widely spaced single cells rather than in layers. Smooth muscle cells of the rough endoplasmic reticulum-rich type may dominate in the foetal and immediate postnatal period. The part of the proteoglycan layer near the endothelium contains isolated macrophages.

The thicker layer underlying the proteoglycan layer (and adjacent to the media) has been called the musculoelastic layer because of the abundance of smooth muscle cells and elastic fibres. This lower intima layer also contains more collagen than the upper layer. Smooth muscle cells are of the myofilament-rich phenotype and arranged in close layers.

APPENDIX E

SPECTRAL RESPONSE OF PHOTOMULTIPLIER TUBE

The spectral response of the HAMAMATSU R955 photomultiplier tube is shown in Figure E.1.

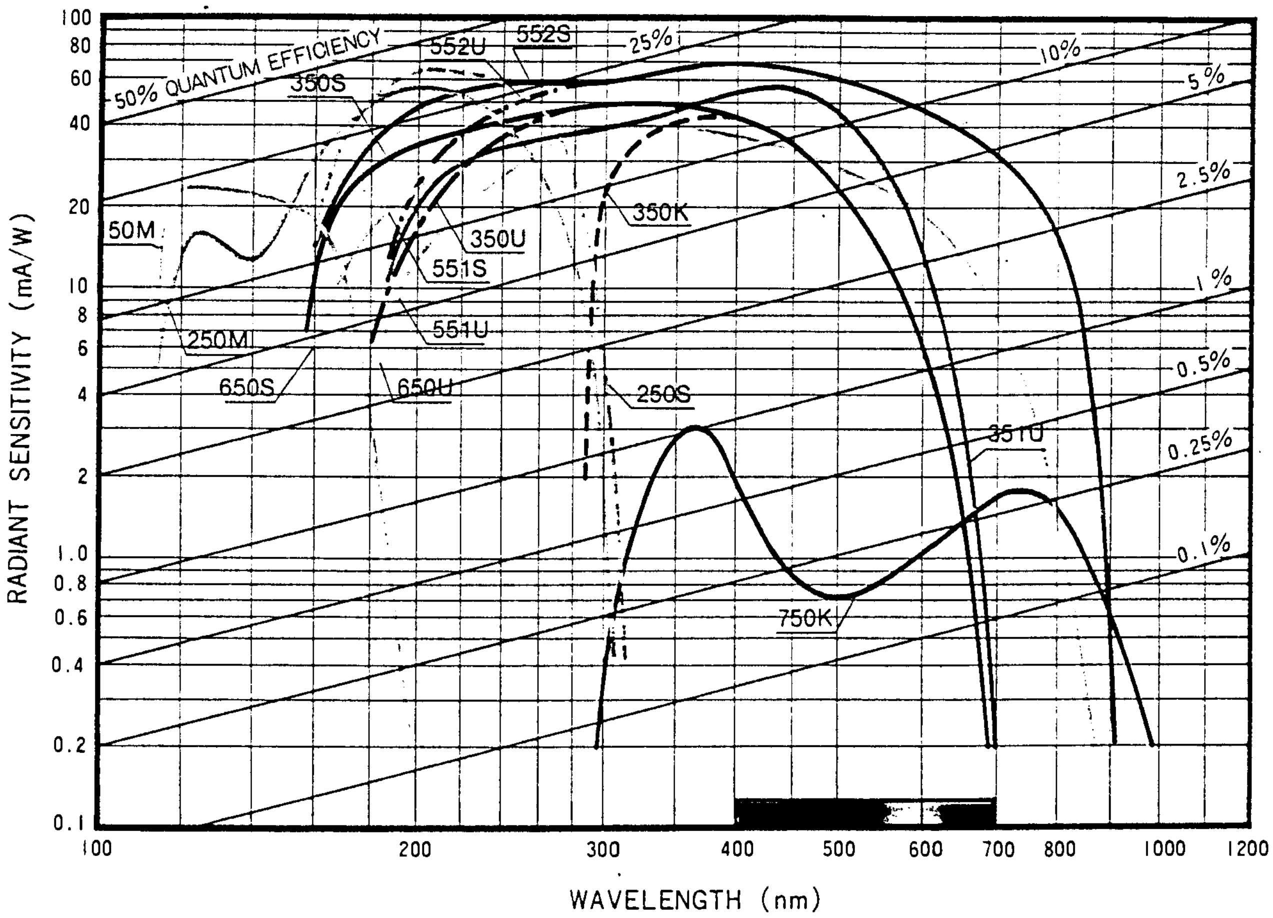

Figure E.1 Spectral response (552S) of HAMAMATSU R955 photomultiplier tube

APPENDIX F

BOXCAR AVERAGERS

Boxcar averagers are instruments which average a repetitive waveform by examining it one piece at a time. One way to look at boxcar averagers is to compare them to a synchronised strobe lamp's flashes, illuminating a rotating object for a split second, making it appear stationary. The boxcar averager operates in an analogous manner. As illustrated in Figure F.1 a repetitive waveform with synchronous triggers is presented to the boxcar. At a precisely selected moment, after receipt of a trigger, an electronic sampling switch closes for a relatively short preset time interval, T_G, known either as the aperture duration, gatewidth, or sample interval. When the switch opens, the balance of the waveform is ignored until the next trigger.

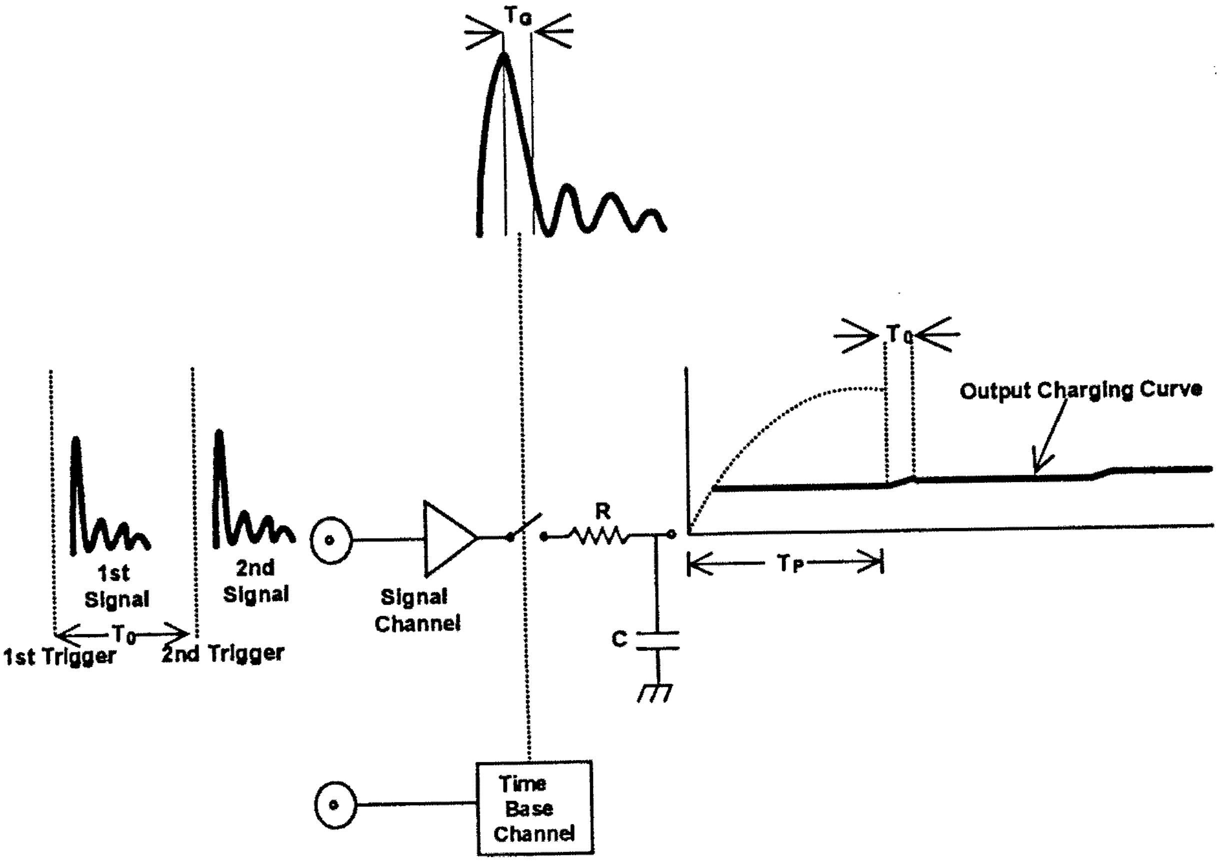

Figure F.1 The principle of a simplified boxcar averager

Because the same waveform segment is sampled repetitively, boxcar output will be a dc voltage asymptotically approaching the average value of that part of the input signal coincident with the sample interval. After an elapsed period of $5(RC)T_P/T_G$ (where T_P is the period between successive triggers), the boxcar output will be within 0.7% of the steady state average. Input noise (any signal asynchronous with the trigger rate) will be similarly processed but its effect at the boxcar output will be greatly reduced, the reduction factor increasing as the effective number of samples taken increases. At any aperture duration setting, the signal to noise improvement ratio (SNIR) increases in proportion to RC/T_G. However, the greater the desired SNIR, the longer the averaging time required.

If more than one point on the waveform is to be examined, or if the entire waveform is to recovered, the boxcar gate can be scanned either manually or automatically across the desired time span.

APPENDIX G

UNCERTAINTIES IN ALGORITHM SCORES

The uncertainty in the determination of the algorithm scores was obtained by examining the fluorescence spectra from 6 tissue samples. For each sample, three fluorescence spectra were recorded successively from the sample. The three fluorescence lineshapes for each sample are shown in Figures G.1a to G.1f.

From the above-mentioned Figures it can be seen that there is a reduction in the fluorescence intensities over the wavelength range 340 nm to 600 nm for each successive fluorescence spectrum recorded from the sample. This reduction in fluorescence intensity is probably due to processes occurring within the tissue as a result of exposure of the tissue sample to the laser radiation.

The sample size was too small for a detailed statistical analysis to be performed to determine the statistical uncertainties in the algorithm scores. Hence, the uncertainties of the algorithm scores were determined as follows. The algorithm score was determined for each set of spectra. The mean of the algorithm scores was then calculated and the variation of the scores from the mean was then determined for each set of spectra. The uncertainty quoted in the algorithm score was the "maximum variation" of the score from the mean for the 6 sets of spectra.

The use of the "maximum variation" as the uncertainty in the algorithm score and, in particular, the decision threshold (DT) is appropriate for this study, in the sense that it is very unlikely that the "true" value of the algorithm score or DT will be outside this interval. The choice of DT, for example, may be biased to the "maximum limit" of DT, i.e., $DT + |\Delta DT|$ (where ΔDT is the uncertainty in DT) to avoid misclassification of normal arteries.

One of the main advantages of the "maximum limit" is: in case of doubt, it can always be enlarged to become "safer" (Müller, 1979). However, (Müller, 1979) and Allisy and Müller (1994) demonstrate that in general, "maximum limits" has drawbacks. For example, they do not lend themselves to the formulation of a suitable propagation law.

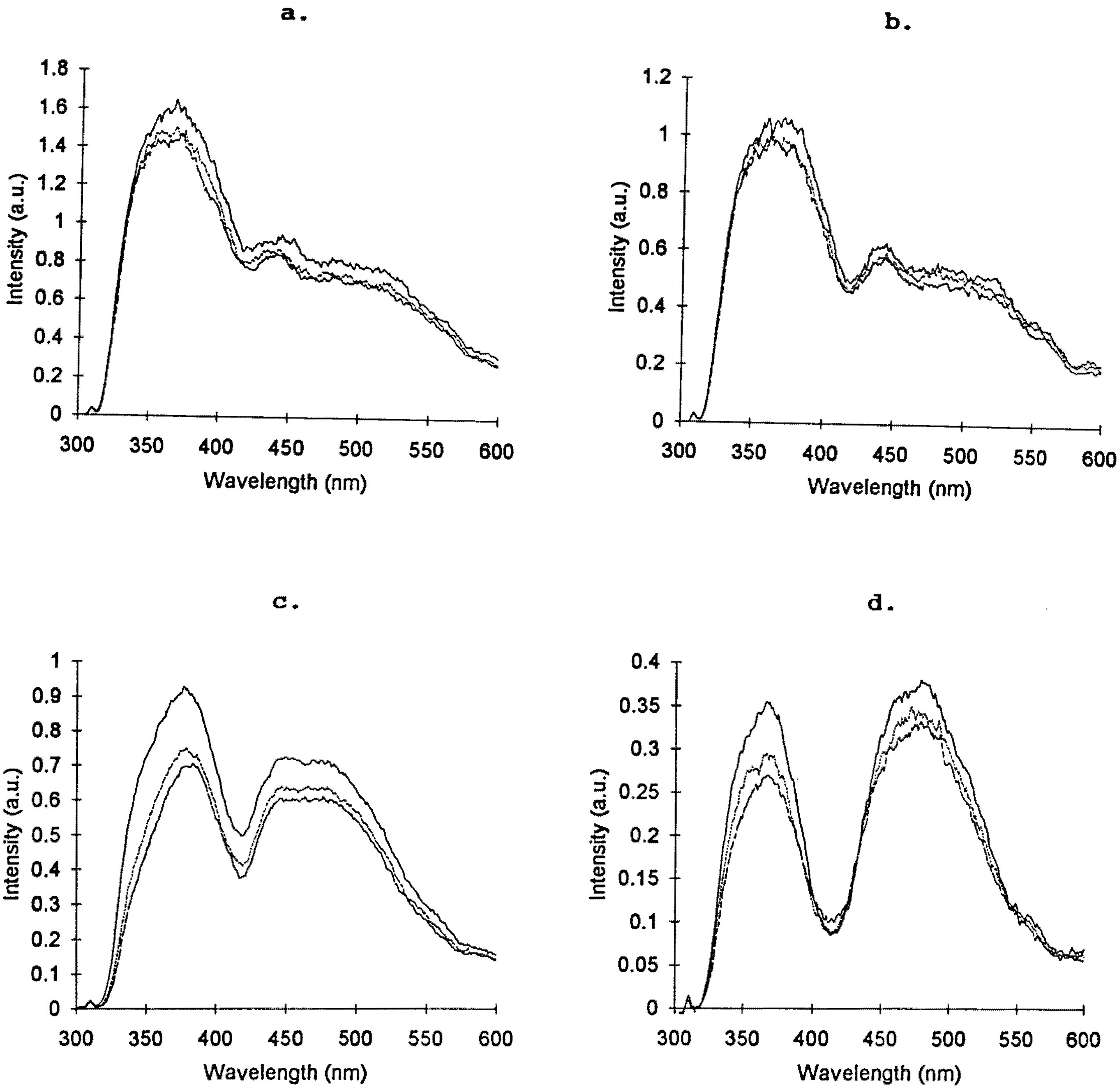

Figure G.1 Fluorescence spectra recorded from six samples (a. to f.) to determine the maximum uncertainties in the algorithm scores. The fluorescence lineshape with the high spectral intensities represent the first scan of the sample and the lineshape with lowest spectral intensities represents the third scan of the sample.

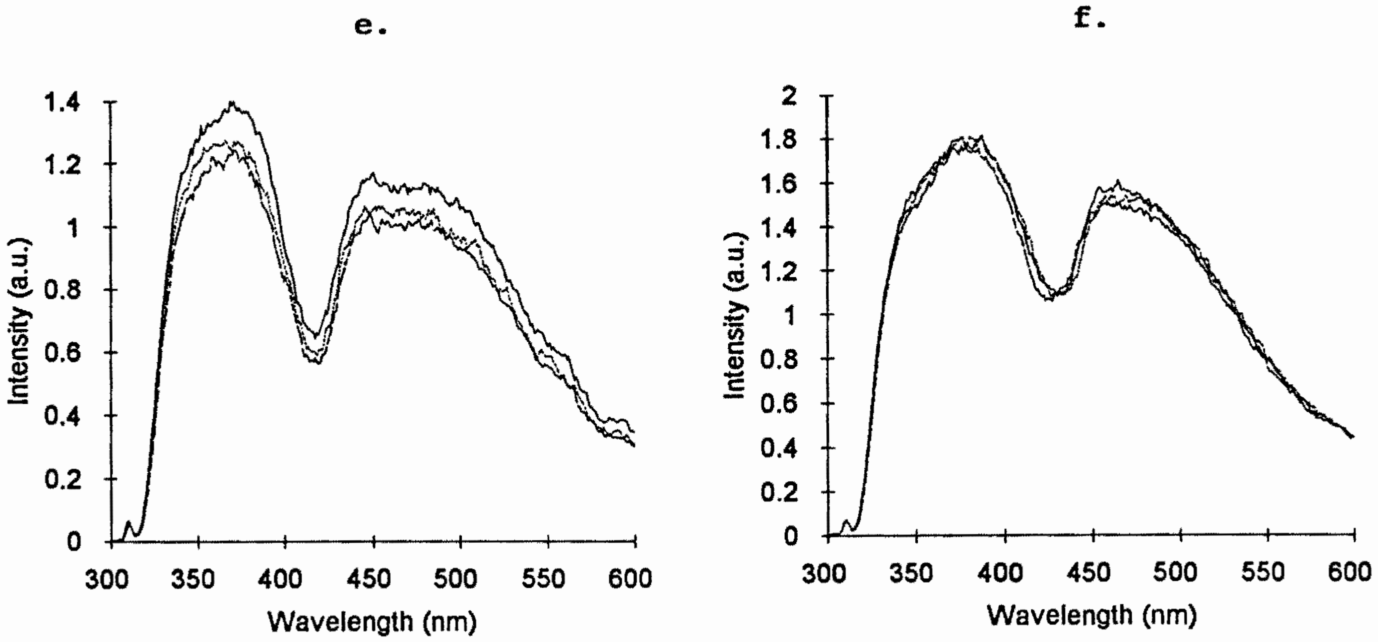

Figure G.1 (continued)

REFERENCES

Allisy A and Müller JW
1994
Assessment of uncertainities in measurements
ICRU News, December 1994: 4-6

Andersson PS, Montán S and Svanberg S
1987
Multispectral system for medical fluorescence imaging
IEEE J Quant Elect QE-23: 1798-1805

Andersson-Engels S, Johansson J, Stenram U, Svanberg K and Svanberg S
1990a
Time-resolved laser-induced fluorescence spectroscopy for enhanced demarcation of human atherosclerotic plaques
J Photochem Photobiol B: Biol 4: 363-369

Andersson-Engels S, Johansson J and Svanberg S
1990b
The use of time-resolved fluorescence for diagnosis of atherosclerotic plaque and malignant tumours
Spectrochimica Acta 46A(8): 1203-1210

Baraga JJ, Rava RP, Taroni P, Kittrell C, Fitzmaurice M and Feld MS
1990
Laser induced fluorescence spectroscopy of normal and atherosclerotic human aorta using 306-310 nm excitation
Lasers Surg Med 10: 245-261

Bergeron A, Douville Y and Duplain G
1988
Complete fluorescence spectrum of a normal and atherosclerotic aorta
Can J Phys 66(12): 1035-1039

Bovet P, Shamlaye C, Kitua, Riesen WF, Paccaud F and Darioli R
1991
High prevalence of cardiovascular risk factors in the Seychelles (Indian Ocean)
Arterioscler Thromb 11: 1730-1736

Breuer H
1990a
Percutaneous transluminal coronary laser angioplasty (PTCLA)
Cardiovasc J of SA V(1): 102-108

Breuer H
1990b
Laser recanalisation of peripheral and coronary vessels
Hospital Supplies: 14-20

Dake MD
1991
Intravascular ultrasound
Curr Opin Radiol 3(2): 181-187

Dardenne MU and Hohla K
1989
UV lasers: Photoablation with the excimer laser - A new surgical tool
Medical Focus 1/89

Dörschel K and Müller G
1991
Photoablation
SPIE Vol 1525 Future Trends in Biomedical Applications of Lasers: 253-279

Fitzmaurice M, Bordagaray JO, Engelmann GL, *et al*
1989
Argon ion induced-excited autofluorescence in normal and atherosclerotic aorta and coronary arteries: Morphologic studies
Am Heart J 118(5): 1028-38

Furzikov NP, Letokhov VS and Oraevsky AA
1988
Fundamentals of laser angioplasty: photoablation and spectral diagnostics
Laser Science and Technology: 243-258
Edited by Chester AN, Letokhov VS and Mertellucci S,
International Science Series, Plenum Press - New York and London

Gmitro AF, Cutruzzola FW, Stetz ML and Deckelbaum LI
1988
Measurement depth of laser-induced tissue fluorescence with application to laser angioplasty
Appl Opt 27(9): 1844-1849

Hecht J
1988
Understanding lasers
Howard W Sams and Company, Division of McMillan Inc., Ft. Worth, Texas, USA

Hoyt CC, Richards-Kortum RR, Costello B, *et al*
1988
Remote biomedical spectroscopic imaging of human artery wall
Lasers Surg Med 8: 1-9

Keil JE, Sutherland SE, Knapp RG, *et al*
1993
Mortality rates and risk factors for coronary disease in black as compared with white men and women
N Engl J Med 329: 73-78

Keijzer M, Richards-Kortum RR, Jacques SL and Feld MS
1989
Fluorescence spectroscopy of turbid media: Autofluorescence of the human aorta
Appl Opt 28(20): 4286-4292

Kiernan JA
1990
Histological and Histochemical Methods: Theory and Practice
Second Edition, Pergamon Press, New York

Kittrell C, Willet RL, De los Santos-Pacheo C, *et al*
1985
Diagnosis of fibrous arterial atherosclerosis using fluorescence
Appl Opt 24(15):2280-2281

Lackowicz JR
1983
Principles of fluorescence spectroscopy
Plenum Press, New York

Laufer G, Wollenek G, Hohla K, *et al*
1988
Excimer laser-induced simultaneous ablation and spectral identification of normal and atherosclerotic arterial tissue layers
Circulation 78(4): 1031-1039

Mollentze WF, Moore AJ, Steyn AF, *et al*
1995
Coronary heart disease risk factors in a rural and urban Orange Free State black population
S Afr Med J 85(2): 90-96

Moretti M
1991
Laser angioplasty attempts comeback
Laser Focus World : 29

Morguet AJ, Körber B, Abel B, Hippler H, Wiegand V and Kreuzer H
1994
Autofluorescence spectroscopy using a XeCl excimer laser system for simultaneous plaque ablation and fluorescence excitation
Lasers Surg Med 14: 238-248

Müller JW
1979
Some second thoughts on error statements
Nucl Instrum Methods 163: 241-251

O'Brien KM, Gmitro AF, Gindi GR, *et al*
1989
Development and evaluation of spectral classification algorithms for fluorescence guided laser angioplasty
IEEE Trans Biomed Eng 36: 424-430

Ogunnowo PO, Odesanmi WO and Andy JJ
1986
Coronary artery pathology of 111 consecutive Nigerians
Trans Roy Soc Trop Med Hyg 80: 923-926

Oraevsky AA, Jacques SL, Pettit GH, Saidi IS, Tittel FK and Henry PD
1992
XeCl laser ablation of atherosclerotic aorta: optical properties and energy pathways
Lasers Surg Med 12: 585-597

Papazoglou TG, Papaioannou T, Arakawa K, Fishbein M, Marmarelis VZ and Grundfest WS
1990
Control of excimer laser aided tissue ablation via laser-induced fluorescence monitoring
Appl Opt 29(33): 4950-4955

Parrish JA
1985
Ultraviolet laser ablation
Arch Dermatol 121: 599-600

Pettit GH, Pini R, Tittel FK, Sauerbrey R, Sartori MP and Henry PD
1990
Excimer laser induced autofluorescence from atherosclerotic human arteries
Lasers Life Sci 3(4): 205-215

Prince MR, LaMuraglia GM, Teng P, Deutsch TF and Anderson RR
1987
Preferential ablation of calcified arterial plaque with laser-induced plasmas
IEEE J Quant Elect QE-23: 1783-1786

Richards-Kortum RR, Mehta A, Kolubayev T, *et al*
1987
Spectroscopic diagnosis for control of laser treatment of atherosclerosis
Laser Spectroscopy #8

Richards-Kortum RR, Mehta A, Kolubayev T, *et al*
1988
Role of collection geometry in spectral diagnosis of atherosclerosis
Proc CLEO '88, Anaheim, CA, USA, April 25-29

Richards-Kortum, Rava RP, Cothren R, *et al*
1989a
A model for extraction of diagnostic information from laser induced fluorescence spectra of human artery wall
Spectrochimica Acta 45A(1): 87-93

Richards-Kortum, Rava RP, Fitzmaurice M, *et al*
1989b
A one-layer model of laser-induced fluorescence for diagnosis of disease in human tissue: applications to atherosclerosis
IEEE Trans Biomed Eng 36(12): 1222-1232

Richards-Kortum R, Rava RP, Petras RE, Fitzmaurice M, Sivak M and Feld MS
1991
Spectroscopic diagnosis of colonic dysplasia
Photochem Photobiol 53(6): 777-786

Ross R
1993
The pathogenesis of atherosclerosis: a perspective for the 1990s
Nature 362: 801-809

Sartori M, Sauerbrey R, Kubodera S, Tittel FK, Roberts R and Henry PD
1987
Autofluorescence maps of atherosclerotic human arteries - a new technique in medical imaging
IEEE J Quant Elect QE-23: 1794-1797

Schaldach M
1990
Cardiovascular laser application
Artif Organs 14(1): 28-40

Schomaker KT, Frisoli JK, Compton CC, *et al*
1992
Ultraviolet laser-induced fluorescence of colonic tissue: Basic biology and diagnostic potential
Lasers Surg Med 12: 63-78

Sechtem U, Arnold G, Keweloh T, Casper C and Curtius JM
In vitro diagnosis of coronary olaque morphology with intravascular ultrasound: comparison with histopathologic findings
Z Kardiol 82(10): 618-627

Singleton DL, Paraskevopoulos G and Higgingson LAJ
1987
Excimer laser angioplasty: Tissue ablation, arterial response, and fibre optic delivery
IEEE J Quant Elect QE-23: 1772-1782

St. Goar FG, Pinto FJ *et al*
1992
Detection of coronary atherosclerosis in young adult hearts using intravascular ultrasound
Circulation 86(3): 756-763

Stary HC, Blankenhorn DH, Chandler AB, *et al*
1992a
A definition of the intima of human arteries and of its atherosclerosis-prone regions
Arterioscler Thromb 12 (1): 120-135

Stary HC
1992b
Composition and classification of human atherosclerotic lesions
Virchows Archiv A Pathol Anat 421: 277-290

Strong JP, Oalmann MC, Newman III WP, *et al*
1984
Coronary heart disease in young black and white males in New Orleans: Community Pathology Study
Am Heart J 108: 747-759

Svanberg S
1989
Medical Applications of Laser Spectroscopy
Physica Scripta T26: 90-98

Taylor RS, Leopold KE, Brimacombe RK and Mihailov S
1988
Dependence of the damage and transmission properties of fused silica fibres on the excimer laser wavelength
Appl Opt 27(15): 3124-3134

Walker ARP, Adam A and Küstner HGV
1993
Changes in total death rate and in ischaemic heart disease death rate in interethnic South African populations, 1978 - 1989
S Afr Med J 83: 602-605

Wu J, Partovi F, Feld MS and Rava RP
1993a
Diffuse reflectance from turbid media: an analytical model of photon migration
Appl Opt 32(7): 1115-1121

Wu J, Feld MS and Rava RP
1993b
Analytical model for extracting intrinsic fluorescence in turbid media
Appl Opt 32(19): 3585-3595

Ye B and Abela GS
1992
Fluorescence behaviour of human arterial tissue
Lasers Med Sci 7: 311-318